INTERFACES AND DEVICE GEOMETRY OF PBS COLLOIDAL QUANTUM DOTS (CQDS) SOLAR CELLS

Qian Dong

A dissertation submitted to the faculty of the University of North Carolina at Chapel Hill in partial fulfillment of the requirements for the degree of Doctor of Philosophy in the Department of Applied Physical Sciences.

Chapel Hill
2019

Approved by:

Rene Lopez

Richard Superfine

Jillian Dempsey

James Cahoon

Scott Warren

ABSTRACT

Qian Dong: Interfaces and Device Geometry of PbS Colloidal Quantum Dots (CQDs) Solar Cells
(Under the direction of Rene Lopez)

The unique properties of lead sulfide (PbS) colloidal quantum dot solar have attracted great interest cells as an emerging photovoltaic technology. In this thesis, a comprehensive study on improving the device performance is carried out through several architectural and materials approaches: 1) introducing a periodic submicron grating pattern, 2) optimizing the film morphology of its electron transport interface, and 3) investigating the physical deposition of the PbS quantum dots. We demonstrated, from both simulation and the experimental results, that by employing a grating pattern, the light absorption-charge carrier compromise could be relaxed since more light absorbing material is packed without upsetting the transport length limit. This results in an increase both in J_{SC} and power conversion efficiency of the device. The same geometry has an added mechanical bonus, allowing a super-flexibility without cracking brittle thin films. A highly flexible and transparent ITO pattern was developed on PET films which survived in our cycling bending test with a minimum diameter of curvature of 3.2 mm and maintained more than 90% of optical transparency over the whole visible wavelength. Subsequently, this patterned ITO/PET substrate demonstrated a promising application for flexible solar cells in our CQDs study. Regarding the electron interface, we explored the effects of various film growth conditions of ZnO between the ITO and the CQDs layer. Our study showed that the device performance could be significantly improved by a ZnO film with optimized morphology realized under specific oxygen pressure during pulsed laser deposition (PLD), in which the carrier transport is facilitated due to limited bimolecular recombination. Finally, by employing PLD, the photo-oxidation rate as function of light intensity, temperature and oxygen pressure of PbS QDs

fabricated by this technique is quantitatively studied. The combined effect of these factors results in a reduced energy barrier that allows the oxidation to proceed at a high rate. These results highlight the importance of photo-excitation on the speed of the oxidation process even at low illumination conditions. Out of this finding a quantitative standard is set up which is useful for characterizing the stability of quantum dots coated with ligands/linkers, and to compare different protection schemes in a fair quantitative way, providing us some guidance on the PbS surface passivation strategy to achieve better PbS CQDs solar cell performance.

ACKNOWLEDGEMENTS

First and foremost, I would like to thank Profs. Rene Lopez and Jillian E. Dempsey for their guidance during my time as a graduate student. They have offered countless suggestions and comments regarding my experiments, and manuscripts since I began research on PbS QDs solar cells in 2015. I also thank Profs. Richard Superfine, James Cahoon, and Scott Warren, for participating in my thesis committee.

Second, I am grateful to have worked alongside Yukihiro Hara, a former postdoc in the Lopez physics group. Most work of this thesis has been published as a joint effort between us. I learned many things from him during our work together and am indebted for the time and effort he spent to conduct our research.

Finally, I would like to thank the many people who offered contributions, help, or suggestions regarding this work. I thank Hanna Starr, Carolyn Hartley, Melody Kessler for helping with the PbS QDs synthesis; Cary Tippet, Taylor Moot, and Tim Garvey for helping me fix all kinds of problem I met in the lab; Huiyan Liu for help with measurement in Shanghai, China, Yulan Fu for helping me with the simulation by Comsol Multiphysics; Carrie Donley, Bob Geil, Jun Yan and Amar Kumbhar for their assistance with and upkeep of CHANL equipment. I also thank people in Eastman Company, Dawn Mason, Mohtashim Saif, Pruthesh Vargantwar and Damon Billodeaux for help with the project and collaboration.

Personally, I am grateful to my family and friends for their unwavering support and encouragement.

TABLE OF CONTENTS

LIST OF FIGURES

LIST OF TABLES

LIST OF ABBREVIATION AND SYMBOLS

α	absorption coefficient
CQDs	colloidal quantum dots
D	diffusivity
DOS	density of trap states
E_g	bandgap
EIS	electrochemical impedance spectroscopy
EQE	external quantum efficiency
FF	fill factor
G	generation rate
h	Planck constant
η	efficiency
ITO	indium tin oxide
J_{SC}	short-circuit current
$\mu_{n,p}$	electron/ hole carrier mobility
L	diffusion wavelength
LIL	laser interference lithography
k_B	Boltzmann constant
τ	carrier lifetime
λ	light wavelength
N_0	photo flux at the surface
PCE	power conversion efficiency
PET	polyethylene terephthalate

PL photoluminescence Spectroscopy

PLD pulsed laser deposition

PVs photovoltaics

q elementary charge

SEM scanning electron microscope

T absolute temperature

TCO transparent conductive oxide

UPS ultraviolet photoelectron spectroscopy

V_{app} applied voltage

V_{OC} open-circuit voltage

XPS X-ray photoelectron spectroscopy

Z complex impedance of the device

Chapter 1 : Introduction

1.1 Meeting the Energy Need of the World

The rising costs of carbon-based fuels and the associated environmental concerns to their extended use have triggered a search for alternative energy sources. In 2001, worldwide primary energy consumption was already 4.25×10^{18}J, which was an average energy consumption rate of 13.5 terawatt (TW). [1,2] 86% percent of this energy was obtained from fossil fuels, with roughly equal parts from oil, coal, and natural gas. Nuclear power accounted for ≈ 0.8 TW of primary (thermal) energy, and the remainder of the energy supply came mostly from unsustainable biomass, with a relatively small contribution from renewable sources. [1,2] The world energy consumption rate is projected to double from the 13.5 TW of 2001 to 27 TW by 2050 and to triple to 43 TW by 2100 [3] due to population and economic growth. Even though many sources indicate there still are ample fossil energy reserves, in one form or another, to supply this energy at some reasonable cost at least for several centuries; the consumption of fossil energy at that rate will produce a potentially significant global climate issue based on CO_2 emission. Therefore, it is imperative to develop and efficiently utilize new, clean methods of energy conversion to meet the growing needs of humanity.

Compared to other renewable energy sources, the solar power is by far the most abundant. More energy from sunlight strikes the earth in1 hour (4.3×10^{20} J) than all the energy currently consumed on the planet in a single year.[4] However, in 2017, after growing at 35% per annum, only 1.7% of the total worldwide electricity was provided by solar power.[5] This large gap between our present use of solar energy and its enormous undeveloped potential has long motivated research for science and technology in a variety of energy renewable technologies. In particular rapid changes have been noted in photovoltaics (PVs), also known as solar cells, that convert sunlight into electrical power. Indeed, since their inception in 1950s, the

power conversion efficiency (PCE) of these devices has steadily improved. Currently, crystalline silicon and gallium arsenide solar cells have proven efficiencies at or above the 25% level.[6] Furthermore, in a multi-junction configuration, where two or more semiconductors are paired to absorb different regions of the solar spectrum, PCE > 45% have been achieved.[7] However, a primary limitation of PVs is their relative cost compared to fossil fuels. This has led to the development of thin film technologies that use less material, such as Cadmium Telluride (CdTe), hydrogenated amorphous silicon (a-Si:H) and Copper Indium Gallium (di)Selenide (CIGS) cells, which have PCE > 21%,11%, and 21%, respectively.[6,8-10] Another avenue to existing thin film PVs was envisioned with the development of an emerging thin-film PVs class in recent decades, which refers to PVs using technologies that have the potential to overcome current efficiency and performance limits or are based on novel, putatively cheap materials. This 3rd generation of PVs mainly includes Dye-sensitized solar cells (DSSC), organic photovoltaic (OPV), perovskite-based PVs, and quantum dot (QD) PVs. This advanced thin film generation approaches to PVs aim to decrease costs to well below the $1/W level of previous thin film PVs to $0.50/W, potentially to $0.20/W or better, by significantly increasing efficiencies but maintaining the economic and environmental cost advantages of thin-film deposition techniques (Fig. 1.1 shows the Efficiency and cost projections of three PV generations).[11,12]

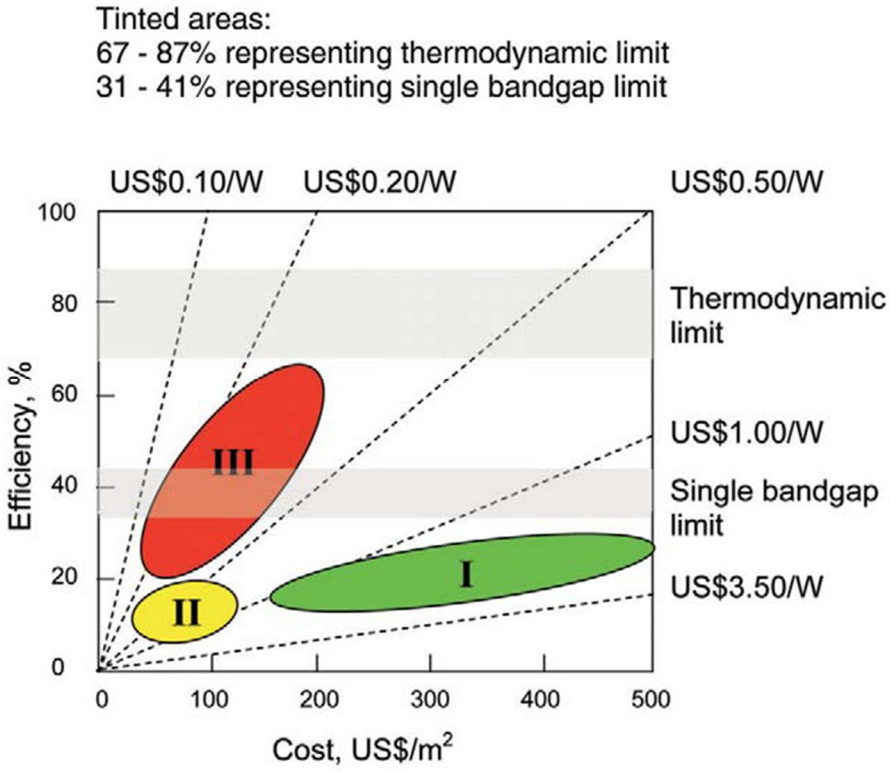

Figure 1.1 Efficiency and cost projections for first- (I), second- (II), and third generation (III) PV technologies (wafer-based, thin films, and advanced thin films, respectively).[11]

One of the important candidates for the new types of solar cells, colloidal quantum dot PVs, take advantage of the fact that semiconductor quantum dots can be synthesized using low-temperature solution processing, with their electronic and optical bandgap tunable by the size and shape of the nanoparticles.[13-15] Despite impressive progress in recent years, the PCE of QDPVs is still below the expected performance for a semiconductor with this bandgap range, resulting in the limitation of its commercial development. Therefore, understanding the device physics and the fundamental mechanisms of charge carrier transport are crucial keys to improve the device performance.

1.2 Colloidal Quantum Dot Solar Cells

1.2.1 Device Configuration and Basic Measurement

The energy band diagrams of typical QDPV device architectures are shown in Figure 1.2a.[16,17] The configuration on the left is a Schottky CQD solar cell, in which the CQD films could act as both absorbers and as the charge transport medium. These cells were based on illumination through a transparent Ohmic contact to a p-type PbS or PbSe CQD film which formed a rectifying junction with a shallow work function metal. However, the device performance has limitations that stems from its architecture: Fermi level pinning at the metal−CQD interface imposes an upper bound on the open-circuit voltage that is well below the voltage predicted from consideration of the CQD band gap alone.[18] Also, it requires illumination at the non-rectifying side of the junction, causing a great loss during carriers' transportation.

Heterojunction CQD solar cell architectures (Figure 1.2a on the right)[16] were developed to overcome the main limitations associated with the Schottky CQD solar cell. The depleted heterojunction architecture[17] uses a highly doped n-type metal oxide (TiO_2 or ZnO) in a p−n heterojunction with a p-type CQD film. The device operation utilizes a charge depletion region formed within the p –type CQD layer to separate photo-generated electron-hole pairs. In this architecture, the device is illuminated through the transparent substrate and the wide-band-gap semiconductor so that the photogeneration occurs close to the junction region, overcoming one of the key limitations of the Schottky architecture. In addition, by employing the heavily doped n-type semiconductor, the depletion region mainly lies in to the CQD film, facilitating the electric charge transport and collection.

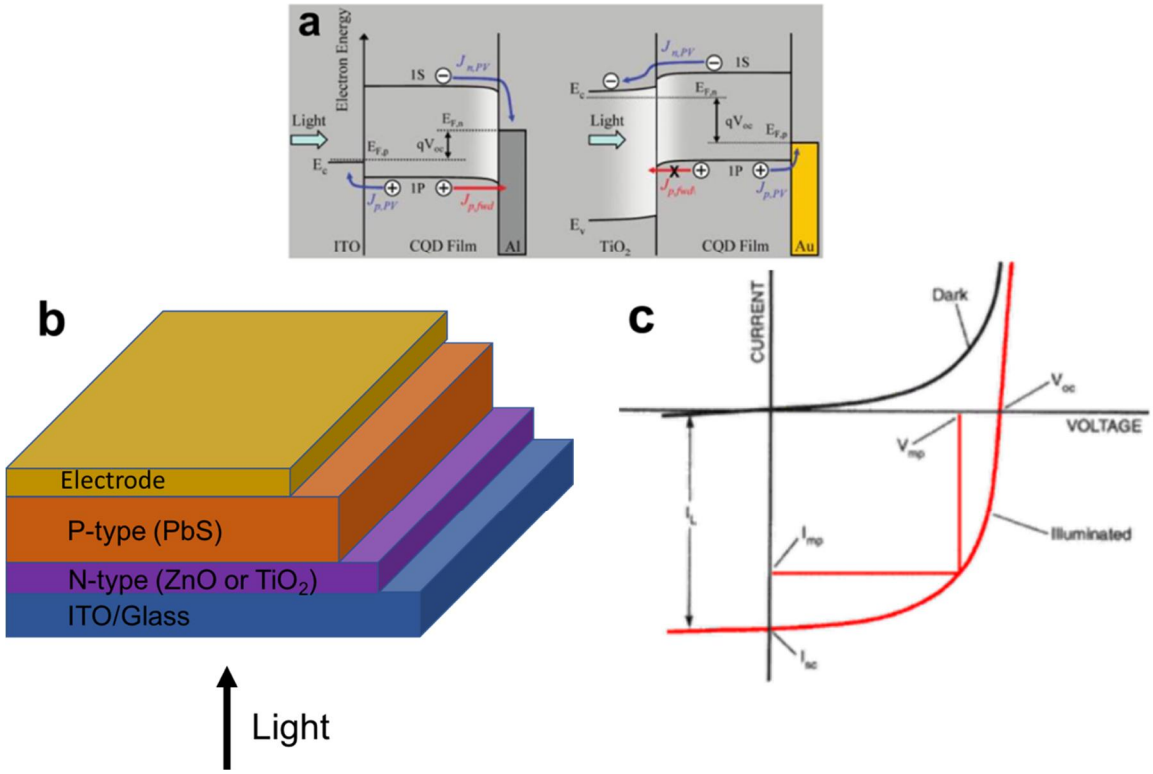

Figure 1.2 (a) Band diagrams of the Schottky junction (left) and the depleted heterojunction (right) CQD photovoltaic architectures under photovoltaic operation close to the maximum V_{OC};[17] (b) Device schematic of layered depleted heterojunction CQD solar cell; (c) Standard current-voltage (J-V) curve under illumination.

The schematic of layered depleted heterojunction CQD solar cell is shown in Fig. 1.2b. When illuminated with light and placed under short-circuit condition (applied voltage Vapp = 0 V), photocurrent is produced in the external circuit. This point is labeled as the short-circuit current (Jsc) on the standard current density vs. voltage (J-V) measurement (Fig. 1.2c). For an ideal solar cell with moderate resistive loss mechanisms, the short-circuit current and the light-generated current are identical. Therefore, the short-circuit current is the largest current which may be drawn from the solar cell. Typically, the current density can be further increased by applying negative bias across the device that raises the internal electric field strength. On the contrary, as the applied voltage (Vapp) is increased to positive bias, the extraction of carriers decreases in part due to a decrease in the internal field, but also due to increased injection of holes from the anode and electrons from the cathode. Under open-circuit conditions, the open-circuit voltage V_{OC} (as shown on the I-V curve) is the maximum voltage available from a solar cell, and this occurs at zero net

current. The open-circuit voltage corresponds to the amount of forward bias on the solar cell due to the bias of the solar cell junction with the light-generated current. The "fill factor", more commonly known by its abbreviation "FF", is an implicit parameter which in conjunction with V_{OC} and Jsc. It is defined as the ratio of the maximum power (P_{MP})from the solar cell to the product of V_{OC} and Jsc:

$$\mathrm{FF} = \frac{P_{MP}}{V_{OC} \times I_{SC}} = \frac{V_{MP} \times I_{MP}}{V_{OC} \times I_{SC}} \tag{1.1}$$

Where V_{MP} and I_{MP} is the voltage and current corresponding to P_{MP}, respectively.

The efficiency is the most commonly used parameter to quantify the performance of one solar cell, which is defined as the ratio of energy output from the solar cell to input energy from the sun. To put it more specifically, the efficiency of a solar cell is determined as the fraction of incident power which is converted to electricity and is defined as:

$$\eta = \frac{V_{OC} I_{SC} FF}{P_{in}} \tag{1.2}$$

Where Voc is the open-circuit voltage, Isc is the short-circuit current, FF is the fill factor and η is the efficiency.

1.2.2 Optoelectronic Properties of Colloidal Quantum Dots

The critical parameters that significantly affect the performance of CQD photovoltaic device are carrier mobility, trap density, carrier lifetime and diffusion length. In this section, the progress of the improvement of these parameters will be discussed.

1.2.2.1 Carrier Mobility

Carrier mobility is one of the most important parameters for semiconductors and plays a crucial role in the performance of CQD solar cells. The carrier mobility of CQD films can be tuned by modifying the QD surface chemistry via ligand exchange and through which, the inter-QD dielectric environment and tunneling distance are changed.[19,20] A wide variety of ligand chemistries have been utilized for CQDs. People found that in the absence of other changes, carrier mobility increases exponentially with decreasing

ligand length (illustrated in Figure 1.3a).[20] Therefore, changing the organic ligand could lead to dramatic variations in the film mobility. Recently, the carrier mobility of CQD films was much improved by developing novel surface ligands. The introduction of halide ligands leads to much higher carrier mobility compared with that of purely organic ligand systems (Figure 1.3b).[16,21] The carrier mobility of bromide ligand films approaches $10^{-1}cm^2/(V \cdot s)$. Solution-phase halide ligand treatment was also used to improve the carrier mobility (Figure 1.3c). [16,22] By using iodide ligand treatment both in solution and in the solid state, the film carrier mobility was increased to over $10^{-1}cm^2/(V \cdot s)$. Recently, based on field effect transistor (FET) measurements, reported majority carrier mobility has reached 10 $cm^2/(V \cdot s)$.[16, 23]

1.2.2.2. Trap Density

Defects in the band gap are demonstrated to be detrimental to QDPV devices. On the one hand, they reduce the photo-carrier population by acting as recombination centers; on the other hand, the quasi-Fermi level splitting range under illumination is reduced, leading to a lower open-circuit voltage. Therefore, it is crucial to reduce the trap density to effectively increase the efficiency of PVs. Literatures already demonstrate that appropriate ligands could passivate electronic trap sites on the QD surface arising from structural aperiodicity and off-stoichiometry of the QD core.[24-26] Among different ligand passivation strategies, making use of hybrid ligands other than pure organic or inorganic ligands is much more effective in reducing the trap density of QDs (Figure 1.4a). [27] Iodide ligand solution-phase processing results in a lower defect concentration compared to untreated quantum dots.[22] Moreover, a strong ligand bonding strength on CQD surfaces is essential for band gap defect prevention. As shown in Figure 1.4b, in comparison to bromide and chloride ligands, iodide ligands give rise to much lower defect concentrations.[28]

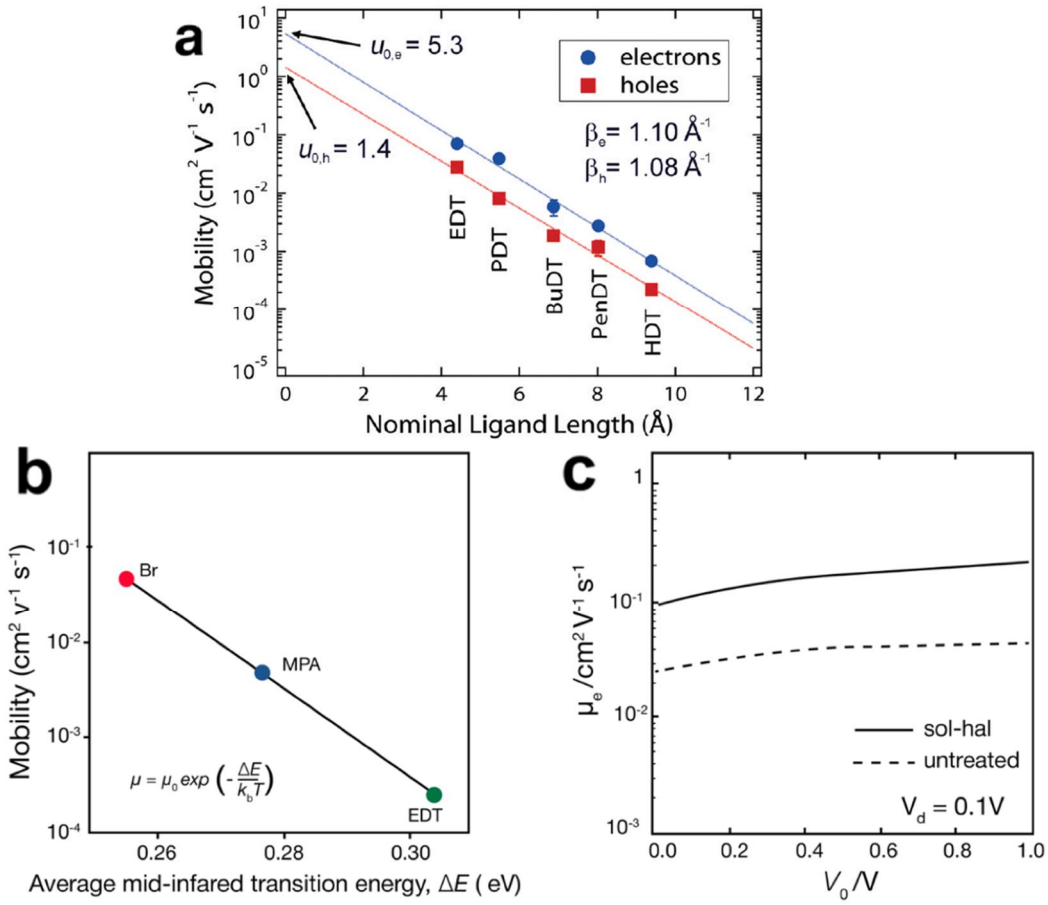

Figure 1.3 (a) Carrier mobility as a function of ligand length in ambipolar PbSe NC field-effect transistors (6.1 nm NCs). [20] (b) Electron mobility comparison for PbS CQD films with bromide, mercaptopropionic acid (MPA), or ethanedithiol (EDT) ligands. [21] (c) Electron mobility for films made from CQDs with or without solution-phase iodide treatment. [22]

1.2.2.3. Carrier Lifetime and Diffusion Length

Considering that the carriers' transport is solely dependent on the diffusion in the diffusion region of actively biased solar cells, the diffusion length is a crucial component to characterize the charge carriers' transport and thus it is of paramount importance to solar cell performance. Given that the diffusion length $L = \sqrt{D\tau}$, where D is the diffusivity and τ is the life time, and $D = \mu \frac{k_B T}{q}$ where μ is the carrier mobility, k_B is the Boltzmann constant, T is the temperature and q is the electron charge, the diffusion length is determined by the carrier lifetime and minority carriers' mobility. Therefore, the lifetime of minority charge carries is also a key factor to determine the device performance. The minority carrier lifetime and the

diffusion length depend strongly on the type and magnitude of recombination processes in the device. Specific correlated to CQD films, theoretical modeling indicates that a higher trap density leads to shorter carrier lifetime. Similarly, the diffusion length of the film increases when the trap density is reduced (as shown in Figure 1.5). [29] Until recently, the highest reported diffusion length for CQD films was about 100nm, approached by employing the hybrid passivation method. [30] A recent study combined partial quantum dot fusing with strong surface passivation to generate a record diffusion length of 230 nm. [31]

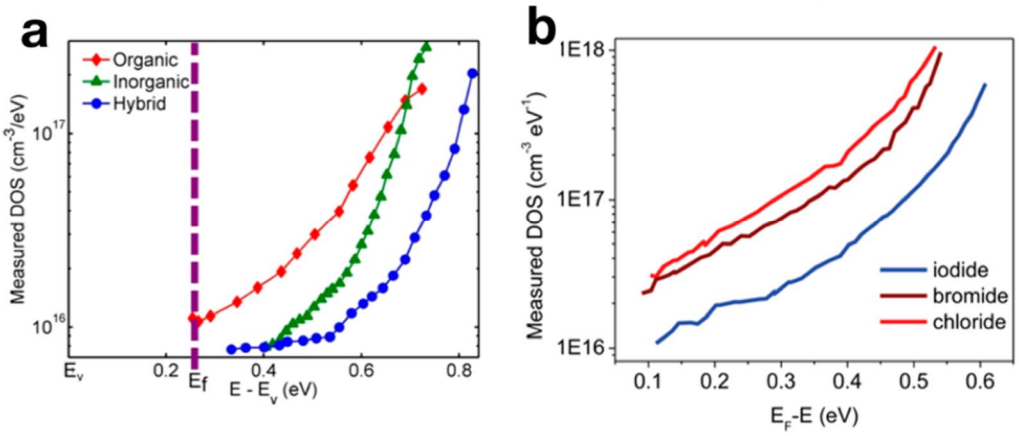

Figure 1.4 (a) Trap density of PbS CQD films with different ligands. [27] The hybrid passivation strategy reduces the trap density compared with both pure organic and pure inorganic ligand passivation. (b) Trap density of films using different halide ligands. [28] Iodide ligands lead to the lowest number of defects.

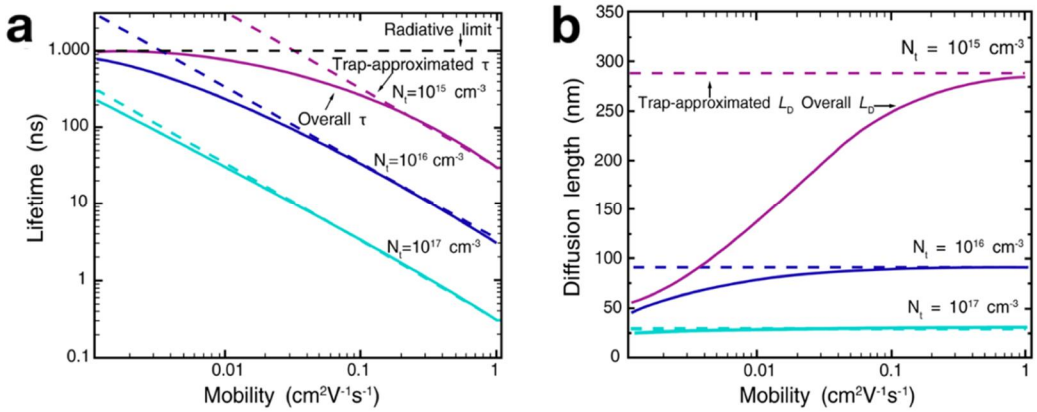

Figure 1.5 Carrier lifetime and diffusion length studies in PbS CQD film by simulation. [29] (a) Theoretical modeling of the relationship between the trap density and carrier lifetime. (b) Theoretical modeling of the relationship between the diffusion length and carrier mobility. As the trap density is reduced, both the carrier lifetime and diffusion length are increased.

1. 3 Light Absorption and Carrier Generation

1.3.1 Characterization

The absorption of light and the generation of electron-hole pairs is fundamental to the operation of a solar cell, whereby the energy of a photons that is equal or larger than the bandgap of the material is absorbed and converted to electrical energy through the creation of electron-hole pairs. To quantitatively describe this process, several critical parameters need to be considered:

1. The absorption coefficient determines how far into a material light of a particular wavelength can penetrate before it is absorbed. The absorption coefficient depends on the material and also on the wavelength of light which is being absorbed.

2. Absorption depth is given by the inverse of the absorption coefficient and describes how deeply light penetrates into a semiconductor before being absorbed. Higher energy light is of a shorter wavelength and has a shorter absorption depth. However, for the light with longer wavelength and lower energy, it is not as readily absorbed and need greater absorption depth for the fully absorption.

3. Generation rate gives the number of electrons generated at each point in the device due to the absorption of photons. Because the light used in PV applications contains many different wavelengths, many different generation rates must be taken into account when designing a solar cell. Neglecting reflection, the amount of light which is absorbed by a material depends on the absorption coefficient (α in cm^{-1}) and the thickness of the absorbing material. The intensity of light at any point in the device can be calculated according to the equation:

$$\mathrm{I} = I_0 e^{-\alpha x} \tag{1.3}$$

where α is the absorption coefficient typically in cm-1; x is the distance into the material at which the light intensity is being calculated; and I_0 is the light intensity at the top surface. Based on this equation, the number of electron-hole pairs being generated in a solar cell can be calculated. Assuming that the loss in light intensity (i.e., the absorption of photons) directly causes the generation of an electron-hole pair, then

the generation G in a thin slice of material is determined by finding the change in light intensity across this slice. Consequently, differentiating the light intensity equation will give the generation at any point in the device:

$$G = \alpha N_0 e^{-\alpha x} \tag{1.4}$$

where N_0 is photon flux at the surface (number of photons/ (per unit area·sec)); α is absorption coefficient; and x is the distance into the material.

1.3.2 Light Absorption and Carrier Generation in CQD Solar Cells

Efficient harvesting of the wide dispersion of photon energies that make up the broad solar spectrum has always been the ultimate goal for low-cost, high-efficiency solar cells (Fig. 1.6a).[32] With size-dependent bandgap ranging from approximately 0.6 to 2.1 eV,[19,33] lead chalcogenide QDs offer an avenue to tandem and multi-junction solar cells that make excellent use of the dispersion of solar fluence as a function of photon energy especially enables infrared photon harvesting which surpasses that of many materials (Fig. 1.6b).[32, 34, 35] In addition, they show promise in multiple exciton generation[36] as well as photon up- and down conversion [37] technologies. All of these favorable properties make the lead chalcogenide QDs especially PbS QDs be a superior candidate for PVs application owing to its potential for solar harvesting.

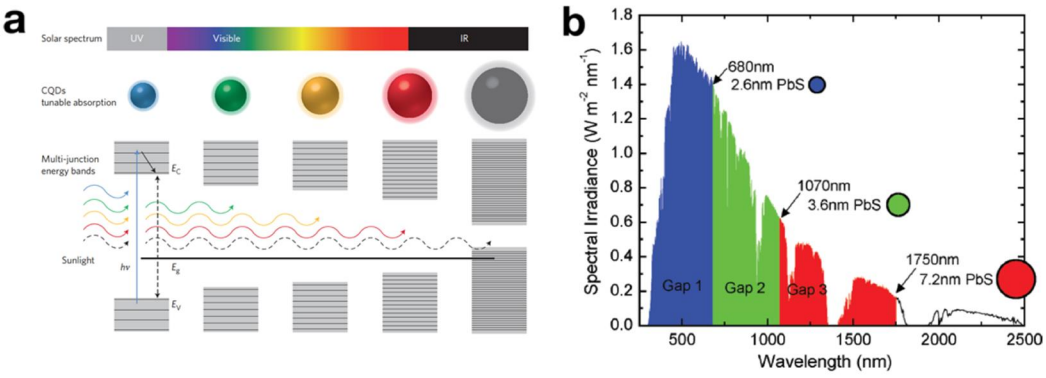

Figure 1.6 (a) The scheme of illustration of the relationship between the CQDs size-dependent absorption and the utilization of the Sun's broad spectrum. [32] (b) Concept of using PbS CQDs with different sizes to build a triple-junction tandem solar cell. [34]

CQDs are strong absorbers, with absorption coefficients for PbS CQDs reaching values of above 10^5 cm^{-1} at blue wavelengths. However, to realize the full light absorption, ideally, the photoactive layer must be thicker than the absorption length of ≈1μm, which assumes two optical passes through the QD film and a typical above-bandgap absorption coefficient of 1×10^4 cm^{-1}.[34] Therefore, at infrared wavelengths near the bandgap energy, CQD solar cells still must contend with the absorption-extraction compromise, whereby absorption lengths exceed charge transport length in CQD film.

Moreover, for CQD solar cells, the local wavelength-dependent carrier generation profile could be obtained from the light absorption distribution utilizing the equation below:

$$g(x, y, \lambda)=-\alpha P(x, y, \lambda)\lambda/hc \quad (1.5)$$

Where P (x, y, λ) is the light intensity within the active layer volume as a function of position (x, y); λ is the wavelength; h is the Planck's constant; C is the speed of light in vacuum; $\alpha=4\pi\kappa/\lambda$ is the imaginary part of the frequency dependent complex refractive index. The total generation rate distribution G (x, y) is the integration of g (x, y, λ) on λ over the spectral band of the absorption.

1.4 Carrier Transport

After generation, the charge carriers need to transport before being collected at the electrodes. To allow efficient charge carrier extraction, a planar PbS QD film must be thinner than the carrier collection length, which corresponds to the sum of the depletion width and the minority electron diffusion length. The depletion width in a semiconductor depends inversely on the square root of the dopant density. Since surface trap states are suspected to act as acceptor-like dopants in PbS QD films, non-stoichiometric surface compositions and incomplete passivation yield a high hole density and therefore a short depletion width. Until recently, the carrier collection length about 300 nm was achieved with less than 100 nm of minority carrier diffusion length and about 200 nm of the depletion width, which was still far below the ≈ 1μm needed for complete light absorption.[30, 34, 38-40] Therefore, effectively increase the light absorption without losing carrier collection is the common goal people are pursuing.

1.5 State of the Art for Quantum Dot Photovoltaics

Since the performance of CQD solar cells is directly affected by the charge carrier generation and collection process, we'll discuss the main improvements for the CQD solar cells from these two aspects.

1.5.1 Enhancement of Light Absorption

Although CQDs are strong absorbers, at infrared wavelength near the band gap energy, CQDs solar cells still need to contend with the compromise of absorption – extraction, whereby the light absorption length exceeds the charge transport length in the CQDs film. Light trapping has been demonstrated as one of the powerful strategy to relax this compromise. In the following section, several different methods of light trapping that have been used to increase the CQDs solar cells performance are discussed.

1.5.1.1. Geometric and Nanophotonic Light Trapping

The idea of making use of different geometric features to increase absorption in CQD solar cells have focused on increasing the number of effective passes that a photon takes through the absorbing material. In a conventional planar cell, the incident light experiences a double-pass path: the light enters the cell, passes through the absorbing material, experiences reflection at the back contact, and passes through the absorbing material once more before leaving the cell. With the introduction of geometric design, a double-pass structure can be converted into a multi-pass structure by the folded light path design such as creating micrometer-scale pyramids in the bottom electrode,[41] or structuring the transparent conductive oxides (TCO) to create diffraction gratings.[42]

Nanophotonic structuring has also been used as a light-trapping method in CQD solar cells. Scalable fabrication methods such as nanoimprint lithography[43] and nanosphere lithography[44] can be applied to structure the bottom electrodes on a sub-micrometer scale. These designs take advantage of light localization and wave-guiding provided by the periodic photonic structures to enhance absorption and consequently the photocurrent in photovoltaic devices.

1.5.1.2. Plasmonic Enhancement

Owing to the unique characteristics of low-temperature solution-processing and size-dependent tunable bandgap that CQDs possess, the CQDs solar cells are particularly suited to benefit from absorption enhancements via plasmonic effects. These nanostructures are extremely sensitive to their local optical environment, offering the possibility to tune or enhance the overall absorption of other materials in their vicinity. Similar as CQDs, their synthesis is solution-based and they are colloidally stable with surfactants. Moreover, the energy of plasmonic nanoparticle resonances is size- and shape- dependent. This effect can be used to target the more weakly absorbing portions of the CQD film spectra and enhance performance in the spectral regions most affected by the absorption−extraction compromise. The noble metals (particularly gold and silver) are popular materials for plasmonic nanostructures used in CQD solar cells. One such device based on plasmonic gold nanoshells embedded in a PbS CQD solar cell is shown in Figure 1.7a. [16, 45] The electric field profile surrounding the gold nanoshell is shown in Figure 1.7b, in which it indicates the expected enhancement at the wavelengths that are minimally absorbed in the CQD film via finite-difference time domain (FDTD)simulations. [16, 45] With introducing the plasmonic nanoshells, a 35% enhancement in photocurrent in the performance-limiting infrared wavelength regime and a resultant 11% improvement of the power conversion efficiency were achieved compared to non-plasmonic control device. Moreover, this enhancement has been demonstrated as well in a device that rapidly transfers hot electrons produced in 5 nm diameter gold particles to PbS CQDs. [16,46] This near-field energy transfer scheme resulted in a 41% increase in the short-circuit current and a 5% increase in the power conversion efficiency compared to those of a non-plasmonic device.

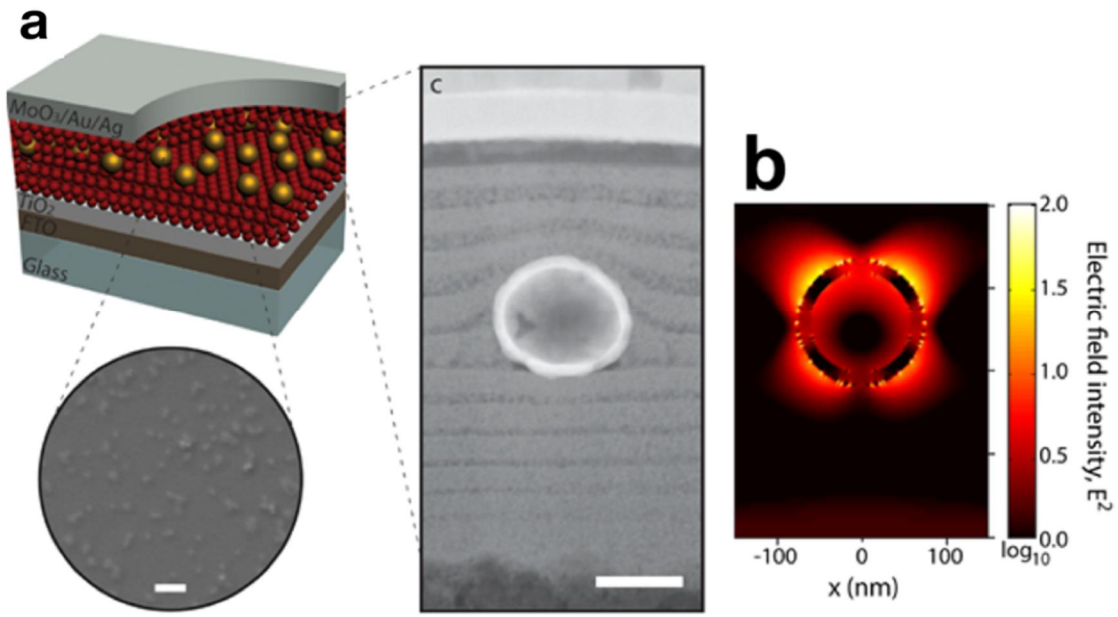

Figure 1.7 (a) (Top left) Schematic of a PbS CQD device with embedded plasmonic gold nanoshells. (Bottom left) Top-view SEM image showing the representative density of nanoshells after CQD deposition. Scale bar 1μm. (Right) Cross-sectional TEM image showing a single gold nanoshellembedded in a PbS CQDfilm. Scale bar 100 nm. [45] (b) FDTD simulation of the electricfield intensity (E^2) profile in the plasmonic film from d on a log scale at the CQD exciton wavelength, λ= 950 nm. [45]

1.5.2 Enhancement of Carrier collection

Due to the unique properties of QDs, a variety of organic, inorganic and hybrid ligand passivation and ligand exchange approaches has been developed to improve the carrier collection by optimizing the QDs in order to impact upon QDs solar cell efficiencies, including extending the recombination time by the passivation of QD surface traps, [47] increasing the carrier mobility by ligand-exchange [48] and engineering the band alignment of QDs to an oxide. [49, 50] In addition to these QDs-based advances, more and more attention has focused on achieving trap-free interfaces and ideal band alignment to seek more performance benefits.

1.5.2.1. Strategies to Improve Hole Collection

Strategies to improve hole collection in CQD solar cells have primarily focused on engineering of the top Ohmic contact to p-type CQD films. Initial studies of heterojunction architectures used gold as the deep

work function top reflective contact.[51] Further studies aimed at reducing the use of this high-cost material found that nickel could act as a suitable replacement if a LiF interlayer was added to prevent reactions and degradation of the metal−semiconductor interface.[52] The introduction of n-type transition-metal oxides MoO_x resulted in significant performance advances. One study found that MoO_x acts as a hole extraction layer by enhancing band-banding at the PbS CQD interface and providing hole transport levels through oxygen vacancies.[53] Another study found that the deep work function MoO_x can remove a reverse-bias Schottky diode otherwise present at the CQD−metal interface by pinning the Fermi level of the top contact. [54] Both studies found that including MoO_x improved the solar cell open-circuit voltage.

1.5.2.2 Strategies to Improve Electron Collection

Since the heterojunction architecture has been successfully fabricated by employing p-type CQD films, a larger number of research has been focused on the electron-collecting layers other than on engineering electrodes in CQD solar cells. Increasing attention has been paid on optimizing the properties of the n-type TiO_2 or ZnO layers for better heterojunction performance. To explore the importance of band offsets between CQD films with different band gaps and the TiO_2 acceptor, a sol−gel-derived TiO_2 precursor was doped with impurities.[55] The optimal band offset resulted in the efficient extraction of carriers even in the absence of a strong electric field. A similar method using magnesium doping was used to tune the ZnO conduction band position and reduce voltage losses associated with the ZnO conduction band tail.[56]

Recombination at the metal oxide-semiconductor interfaces is another area attracting ongoing concern in heterojunction CQD solar cells. Several strategies have been used to improve this performance-limiting process. The introduction of a buffer layer (BL) between the CQD film and TiO_2 or ZnO has been demonstrated a feasible method to significantly reduce the interface recombination and enhance the device performance accordingly. With the aim to reduce this recombination and to enhance charge extraction, several BL materials have been exploited, such as ZnO, [57] fullerenes, [58] molecular monolayers (such as 4-aminobenzoic acid), [59] and polymers, [60] and it was found that the BL under finely control could give the

appropriate energy band alignment for the heterojunction without affecting the depletion region in the CQD solid to ensure that the incoming electrons can be efficiently injected into the electron collecting layer from the CQD films. Thin ZnO buffer layer between the PbS CQD film and TiO_2 was found to result in a nearly 2-fold reduction of the interface recombination rate. [57] The introduction of a self-assembled monolayer as the BL into a depleted heterojunction PbS CQD solar cell resulted in a device PCE of 10.7%, with 11% of PCE increase.[59]

1.6 Our work

Despite the extensive advance in QDs solar cells, the power conversion efficiency of PbS QD solar cell is still far below the expected performance for a semiconductor with this bandgap range, and thus it has a large room for further development. In our work, we proposed two approaches from the device architecture engineering perspective to improve the performance of PbS QDs solar cells: by introducing a periodic submicron grating pattern or optimizing the morphology of ZnO film, the optoelectrical performance of PbS QD solar cells was significantly improved. In chapter 2 and 4, these studies will be fully discussed not also from the device performance but also from the fundamental mechanism underneath. In chapter 3, as inspired from the grating pattern introduced in chapter 2, an extended application was well developed−a creation of highly flexible and transparent conducive Indium Tin Oxide (ITO) film, which opens a door to accessing super-flexible PbS QDs solar cells. Finally, in chapter 5, other than from the engineering point, we enabled a fundamental study on the PbS QD itself, by running calculations, a quantitative way to describe the oxidation rate of PbS QDs as a function of light intensity, temperature and oxygen pressure will be elaborated, which provides us with a reference to further develop the passivation strategy of PbS QDs.

REFERENCES

(1) Energy Information Administration (2005) *Annual Energy Outlook* (US Dept of Energy, Washington, DC).

(2) Lewis, N.S.; Nocera, D. G. Powering the planet: Chemical challenges in solar energy utilization. *Proc Natl Acad Sci USA*. **2006**, *103*(43):15729-35

(3) Hoffert, M. I.; Caldeira, K.; Jain, A. K.; Haites, E. F.; Harvey, L. D. D.; Potter, S. D.; Schlesinger, M. E.; Schneider, S. H.; Watts, R. G.; Wigley, T. M. L.; et al. Energy Implications of Future Stabilization of Atmospheric CO_2 Content. *Nature* **1998**, *395* (6705), 881–884.

(4) United Nations Development Program (2003) *World Energy Assessment Report: Energy and the Challenge of Sustainability* (United Nations, New York).

(5) IEA. *World energy outlook 2012*-executive summary English version. https://www.iea.org/Textbase/npsum/weo2017SUM.pdf.

(6) Polman, A.; Knight, M.; Garnett, E. C.; Ehrler, B.; Sinke, W. C. Photovoltaic Materials: Present Efficiencies and Future Challenges. *Science (80-.).* **2016**, *352* (6283).

(7) Wilson, T.; Thomas, T.; Führer, M.; Ekins-Daukes, N. J.; Roucka, R.; Clark, A.; Johnson, A.; Hoffman, R.; Begarney, D. Single and Multi-Junction Solar Cells Utilizing a 1.0 EV SiGeSn Junction. *AIP Conf. Proc.* **2016**, *1766* (September), 0–6.

(8) Green, M. A.; Emery, K.; Hishikawa, Y.; Warta, W.; Dunlop, E. D. Solar Cell Efficiency Tables (Version 45). *Prog. Photovoltaics,* **2013**, No. *October 2011*, 156–172.

(9) Sai, H.; Matsui, T.; Matsubara, K.; Kondo, M.; Yoshida, I. 11.0% efficient thin-film microcrystalline silicon solar cells with honeycomb textured substrates. *IEEE J. Photovolt*. **2014**, *4*, 1349–1353.

(10) Jackson, P.; Hariskos, D.; Wuerz, R.; Kiowski, O.; Bauer, A.; Friedlmeier, T. M.; Powalla, M. Properties of $Cu(In,Ga)Se_2$ Solar Cells with New Record Efficiencies Up to 21.7%. *Phys. Status Solidi RRL,* **2015**, *9*, 28–31.

(11) Brown, G. F.; Wu, J. Third Generation Photovoltaics. *Laser Photonics Rev.* **2009**, *3* (4), 394–405.

(12) Semonin, O. E.; Luther, J. M.; Beard, M. C. Quantum Dots for Next-Generation Photovoltaics. *Mater. Today* **2012**, *15* (11), 508–515.

(13) Cunningham, P. D.; Boercker, J. E.; Foos, E. E.; Lumb, M. P.; Smith, A. R.; Tischler, J. G.; Melinger, J. S. Enhanced Multiple Exciton Generation in Quasi-One-Dimensional Semiconductors. *Nano Lett.* **2011**, *11*, 3476–3481.

(14) Semonin, O. E.; Luther, J. M.; Choi, S.; Chen, H.; Gao, J.; Nozik, A. J.; Beard, M. C. Peak External Photocurrent Quantum Efficiency Exceeding 100% via MEG In a Quantum Dot Solar Cell. **2011**, *334* , 1530–1534.

(15) Gao, J.; Luther, J. M.; Semonin, O. E.; Ellingson, R. J.; Nozik, A. J.; Beard, M. C. Quantum Dot Size Dependent J - V Characteristics in Heterojunction ZnO/PbS Quantum Dot Solar Cells. *Nano Lett.* **2011**, *11*, 1002–1008.

(16) Taylor, R. A.; Ramasamy, K. Colloidal Quantum Dots Solar Cells. *SPR Nanosci.* **2017**, *4*, 142–

168.

(17) Pattantyus-Abraham, A. G.; Kramer, I. J.; Barkhouse, A. R.; Wang, X.; Konstantatos, G.; Debnath, R.; Levina, L.; Raabe, I.; Nazeeruddin, M. K.; Grätzel, M.; et al. Depleted-Heterojunction Colloidal Quantum Dot Solar Cells. *ACS Nano* **2010**, *4*, 3374−3380.

(18) Henry, C. H. Limiting Efficiencies of Ideal Single and Multiple Energy Gap Terrestrial Solar Cells. *J. Appl. Phys.* **1980**, *51*, 4494.

(19) Brown, P. R.; Kim, D.; Lunt, R. R.; Zhao, N.; Bawendi, M. G.; Grossman, J. C.; Bulović, V. Energy Level Modification in Lead Sulfide Quantum Dot Thin Films through Ligand Exchange. *ACS Nano* **2014**, *8* (6), 5863–5872.

(20) Liu, Y.; Gibbs, M.; Puthussery, J.; Gaik, S.; Ihly, R.; Hillhouse, H. W.; Law, M. Dependence of Carrier Mobility on Nanocrystal Size and Ligand Length in Pbse Nanocrystal Solids. *Nano Lett.* **2010**, *10* (5), 1960–1969.

(21) Tang, J.; Kemp, K. W.; Hoogland, S.; Jeong, K. S.; Liu, H.; Levina, L.; Furukawa, M.; Wang, X.; Debnath, R.; Cha, D.; et al. Colloidal-Quantum-Dot Photovoltaics Using Atomic-Ligand Passivation. *Nat. Mater*. **2011**, *10*, 765−771.

(22) Ning, Z.; Ren, Y.; Hoogland, S.; Voznyy, O.; Levina, L.; Stadler, P.; Lan, X.; Zhitomirsky, D.; Sargent, E. H. All-Inorganic Colloidal Quantum Dot Photovoltaics Employing Solution-Phase Halide Passivation. *Adv. Mater*. **2012**, *24*, 6295−6299.

(23) Oh, S. J.; Berry, N. E.; Choi, J.-H.; Gaulding, E. A.; Paik, T.; Hong, S.-H.; Murray, C. B.; Kagan, C. R. Stoichiometric Control of Lead Chalcogenide Nanocrystal Solids To Enhance Their Electronic and Optoelectronic Device Performance. *ACS Nano*, **2013**, *7*, 2413−2421.

(24) Voznyy, O.; Zhitomirsky, D.; Stadler, P.; Ning, Z.; Hoogland, S.; Sargent, E. H. A Charge-Orbital Balance Picture of Doping in Colloidal Quantum Dot Solids. *ACS Nano*, **2012***, 6*, 8448–8455.

(25) Oh, S. J.; Berry, N. E.; Choi, J.-H.; Gaulding, E. A.; Paik, T.; Hong, S. H.; Murray, C. B.; Kagan, C. R. Stoichiometric Control of Lead Chalcogenide Nanocrystal Solids to Enhance Their Electronic and Optoelectronic Device Performance. *ACS Nano*, **2013**, *7*, 2413–2421.

(26) Kim, D.; Kim, D.-H.; Lee, J.-H.; Grossman, J. C. Impact of Stoichiometry on the Electronic Structure of PbS Quantum Dots. *Phys. Rev. Lett.* **2013**, *110*, 196802.

(27) Ip, A. H.; Thon, S. M.; Hoogland, S.; Voznyy, O.; Zhitomirsky, D.; Debnath, R.; Levina, L.; Rollny, L. R.; Carey, G. H.; Fischer, A.; et al. Hybrid Passivated Colloidal Quantum Dot Solids. *Nat.Nanotechnol*. **2012**, *7*, 577−582.

(28) Ning, Z.; Voznyy, O.; Pan, J.; Hoogland, S.; Adinolfi, V.; Xu, J.; Li, M.; Kirmani, A. R.; Sun, J. P.; Minor, J.; et al. Air-Stable n-Type Colloidal Quantum Dot Solids. *Nat. Mater.* **2014**, *13*, 822−828.

(29) Zhitomirsky, D.; Voznyy, O.; Levina, L.; Hoogland, S.; Kemp, K. W.; Ip, A. H.; Thon, S. M.; Sargent, E. H. Engineering Colloidal Quantum Dot Solids within and beyond the Mobility-Invariant Regime. *Nat. Commun*. *2014*, *5*.

(30) Zhitomirsky, D.; Voznyy, O.; Hoogland, S.; Sargent, E. H. Measuring Charge Carrier Diffusion in Coupled Colloidal Quantum Dot Solids. *ACS Nano* **2013**, *7* (6), 5282–5290.

(31) Carey, G. H.; Levina, L.; Comin, R.; Voznyy, O.; Sargent, E. H. Record Charge Carrier Diffusion Length in Colloidal Quantum Dot Solids via Mutual Dot-to-Dot Surface Passivation. *Adv. Mater.* **2015**, *27*, 3325−3330.

(32) Lan, X.; Masala, S.; Sargent, E. H. Charge-Extraction Strategies for Colloidal Quantum Dot Photovoltaics. *Nat. Mater.* **2014**, *13* (3), 233–240.

(33) Chuang, C. H. M.; Maurano, A.; Brandt, R. E.; Hwang, G. W.; Jean, J.; Buonassisi, T.; Bulović, V.; Bawendi, M. G. Open-Circuit Voltage Deficit, Radiative Sub-Bandgap States, and Prospects in Quantum Dot Solar Cells. Nano Lett. 2015, 15 (5), 3286–3294.

(34) Tang, J.; Sargent, E. H. Infrared colloidal quantum dots for photovoltaics: fundamentals and recent progress. *Adv. Mater.* **23,** 12–29 (2011).

(35) Alivisatos, A. P. Semiconductor Clusters, Nanocrystals, and Quantum Dots. *Science* **271,** 933–937 (1996).

(36) Semonin, O. E.; Luther, J. M.; Choi, S.; Chen, H.; Gao, J.; Nozik, A. J.; Beard, M. C. Peak External Photocurrent Quantum Efficiency Exceeding 100% via MEG in a Quantum Dot Solar Cell. *Science*, **2011,** *334*, 1530–1533.

(37) Huang, X.; Han, S.; Huang, W.; Liu, X. Enhancing Solar Cell Efficiency: The Search for Luminescent Materials as Spectral Converters. *Chem. Soc. Rev.* **2013**, 42, 173–201.

(38) Brown, P. R.; Lunt, R. R.; Zhao, N.; Osedach, T. P.; Wanger, D. D.; Chang, L. Y.; Bawendi, M. G.; Bulović, V. Improved Current Extraction from ZnO/PbS Quantum Dot Heterojunction Photovoltaics Using a MoO_3 Interfacial Layer. *Nano Lett.* **2011**, *11* (7), 2955–2961.

(39) Johnston, K. W.; Pattantyus-Abraham, A. G.; Clifford, J. P.; Myrskog, S. H.; Hoogland, S.; Shukla, H.; Klem, E. J. D.; Levina, L.; Sargent, E. H. Efficient Schottky-Quantum-Dot Photovoltaics: The Roles of Depletion, Drift, and Diffusion. *Appl. Phys. Lett.* **2008**, *92* (12).

(40) Rekemeyer, P. H.; Chang, S.; Chuang, C. H. M.; Hwang, G. W.; Bawendi, M. G.; Gradečak, S. Enhanced Photocurrent in PbS Quantum Dot Photovoltaics via ZnO Nanowires and Band Alignment Engineering. *Adv. Energy Mater.* **2016**.

(41) Labelle, A. J.; Thon, S. M.; Masala, S.; Adachi, M. M.; Dong, H.; Farahani, M.; Ip, A. H.; Fratalocchi, A.; Sargent, E. H. Colloidal Quantum Dot Solar Cells Exploiting Hierarchical Structuring. *Nano Lett*. **2015**, *15*, 1101−1108.

(42) Mahpeykar, S. M.; Xiong, Q.; Wang, X. Resonance-Induced Absorption Enhancement in Colloidal Quantum Dot Solar Cells Using Nanostructured Electrodes. *Opt. Express*, **2014**, *22*, A1576−A1588.

(43) Kim, S.; Kim, J. K.; Gao, J.; Song, J. H.; An, H. J.; You, T. S.;Lee, T. S.; Jeong, J. R.; Lee, E. S.; Jeong, J. H.; et al. Lead Sulfide Nanocrystal Quantum Dot Solar Cells with Trenched ZnO Fabricated via Nanoimprinting. *ACS Appl. Mater. Interfaces*, **2013**, *5*, 3803−3808.

(44) Adachi, M. M.; Labelle, A. J.; Thon, S. M.; Lan, X.; Hoogland, S.; Sargent, E. H. Broadband Solar Absorption Enhancement via Periodic Nanostructuring of Electrodes. *Sci. Rep*. **2013**, *3*, No. 2928.

(45) Paz-Soldan, D.; Lee, A.; Thon, S. M.; Adachi, M. M.; Dong, H.; Maraghechi, P.; Yuan, M.; Labelle, A. J.; Hoogland, S.; Liu, K.; et al. Jointly Tuned Plasmonic−Excitonic Photovoltaics Using Nanoshells. *Nano Lett*. **2013**, *13*, 1502−1508.

(46) Kholmicheva, N.; Moroz, P.; Rijal, U.; Bastola, E.; Uprety, P.; Liyanage, G.; Razgoniaev, A.; Ostrowski, A. D.; Zamkov, M. Plasmonic Nanocrystal Solar Cells Utilizing Strongly Confined Radiation. *ACS Nano*, **2014**, *8*, 12549−12559.

(47) Neo, D. C. J.; Cheng, C.; Stranks, S. D.; Fairclough, S. M.; Kim, J. S.; Kirkland, A. I.; Smith, J. M.; Snaith, H. J.; Assender, H. E.; Watt, A. A. R. Influence of Shell Thickness and Surface Passivation on PbS/CdS Core/Shell Colloidal Quantum Dot Solar Cells. *Chem. Mater.* **2014**, *26* (13), 4004–4013

(48) Tang, J.; Kemp, K. W.; Hoogland, S.; Jeong, K. S.; Liu, H.; Levina, L.; Furukawa, M.; Wang, X.; Debnath, R.; Cha, D.; et al. Colloidal-Quantum-Dot Photovoltaics Using Atomic-Ligand Passivation. *Nat. Mater.* **2011**, *10* (10), 765–771.

(49) Timp, B. A.; Zhu, X. Y. Electronic Energy Alignment at the PbSe Quantum Dots /ZnO($10\bar{1}0$) Interface. *Surf. Sci.* **2010**, *604* (17–18), 1335–1341.

(50) Chuang, C.-H. M.; Brown, P. R.; Bulović, V.; Bawendi, M. G. Improved Performance and Stability in Quantum Dot Solar Cells through Band Alignment Engineering. *Nat. Mater.* **2014**, *13* (8), 796–801.

(51) Pattantyus-Abraham, A. G.; Kramer, I. J.; Barkhouse, A. R.; Wang, X.; Konstantatos, G.; Debnath, R.; Levina, L.; Raabe, I.; Nazeeruddin, M. K.; Grätzel, M.; et al. Depleted-Heterojunction Colloidal Quantum Dot Solar Cells. ACS Nano 2010, 4, 3374−3380

(52) Debnath, R.; Greiner, M. T.; Kramer, I. J.; Fischer, A.; Tang, J.; Barkhouse, D. A. R.; Wang, X.; Levina, L.; Lu, Z.-H.; Sargent, E. H. Depleted-Heterojunction Colloidal Quantum Dot Photovoltaics Employing Low-Cost Electrical Contacts. Appl. Phys. Lett. 2010, 97, 023109.

(53) Gao, J.; Perkins, C. L.; Luther, J. M.; Hanna, M. C.; Chen, H. Y.; Semonin, O. E.; Nozik, A. J.; Ellingson, R. J.; Beard, M. C. n-Type Transition Metal Oxide as a Hole Extraction Layer in PbS Quantum Dot Solar Cells. *Nano Lett*. **2011**, *11*, 3263−3266.

(54) Brown, P. R.; Lunt, R. R.; Zhao, N.; Osedach, T. P.; Wanger, D. D.; Chang, L.Y.; Bawendi, M. G.; Bulović, V. Improved Current Extraction from ZnO/PbS Quantum Dot Heterojunction Photovoltaics Using a MoO_3 Interfacial Layer. *Nano Lett*. **2011**, *11*, 2955−2961.

(55) Liu, H.; Tang, J.; Kramer, I. J.; Debnath, R.; Koleilat, G. I.; Wang, X.; Fisher, A.; Li, R.; Brzozowski, L.; Levina, L.; et al. Electron Acceptor Materials Engineering in Colloidal Quantum Dot Solar Cells. Adv. Mater. 2011, 23, 3832−3837.

(56) Hoye, R. L. Z.; Ehrler, B.; Böhm, M. L.; Muñoz-Rojas, D.; Altamimi, R. M.; Alyamani, A. Y.; Vaynzof, Y.; Sadhanala, A.; Ercolano, G.; Greenham, N. C.; Improved Open-Circuit Voltage in ZnO−PbSe Quantum Dot Solar Cells by Understanding and Reducing Losses Arising from the ZnO Conduction Band Tail. Adv. Energy Mater. 2014,4

(57) Kemp, K. W.; Labelle, A. J.; Thon, S. M.; Ip, A. H.; Kramer, I. J.; Hoogland, S.; Sargent, E. H. Interface Recombination in Depleted Heterojunction Photovoltaics Based on Colloidal Quantum Dots. Adv. Energy Mater. 2013, 3, 917−922.

(58) Yuan, M.; Voznyy, O.; Zhitomirsky, D.; Kanjanaboos, P.; Sargent, E. H. Synergistic Doping of Fullerene Electron Transport Layer and Colloidal Quantum Dot Solids Enhances Solar Cell Performance. *Adv. Mater.* **2015**, *27* (5), 917–921

(59) Kim, G. H.; García De Arquer, F. P.; Yoon, Y. J.; Lan, X.; Liu, M.; Voznyy, O.; Yang, Z.; Fan, F.; Ip, A. H.; Kanjanaboos, P.; et al. High-Efficiency Colloidal Quantum Dot Photovoltaics via Robust Self-Assembled Monolayers. *Nano Lett.* **2015**, *15* (11), 7691–7696.

(60) Azmi, R.; Aqoma, H.; Hadmojo, W. T.; Yun, J. M.; Yoon, S.; Kim, K.; Do, Y. R.; Oh, S. H.; Jang, S. Y. Low-Temperature-Processed 9% Colloidal Quantum Dot Photovoltaic Devices through Interfacial Management of p-n Heterojunction. *Adv. Energy Mater.* **2016**, *6* (8), 1–10.

Chapter 2 : Photovoltaic Performance in PbS Quantum Dot Solar Cells with Submicron Periodic Grating Structure

2.1 Introduction

In the past decade, solution- processed solar cells based on lead chalcogenide (PbX, X= S, Se, Te) colloidal quantum dots (CQDs) have become one emerging photovoltaic (PV) technology[1] that can potentially meet the goal of energy sustainability with lost-cost technologies for efficient solar energy harvesting. Specifically, among different kinds of lead chalcogenide QDs, PbS QDs has received the most attention for solar cell applications. On the one hand, they possess inexpensive and earth- abundant nature,[2] scalable synthesis, good stability,[3] and solution-processability, allowing ease of large-scale and low-cost fabrication; on the other hand, by adding quantum confinement, its bandgap can be tuned to 0.7-2.1 eV,[4] thereby falling in the range that best optimizes electrical conversion of the solar spectrum. Moreover, PbS CQDs allows passivation using a wider variety of ligands.[5,6] All of these properties make PbS QDs a promising candidate superior than other QD materials in lead chalcogenide family. Indeed, the certified QDPV efficiency record has rapidly increased from 3% to >12% within recent 5 years predominantly due to improvements in PbS QDPVs. [1, 7-12]

Despite recent advances, the power conversion efficiency of PbS QDPV is still below expectation for a semiconductor with this bandgap range. Although the diffusion length has been tripled through interface engineering approach,[13] a fully light-absorbing CQD film is still too thick to extract all generated photocarriers with high efficiency, leading to an absorption−extraction compromise.[14, 15] Device architectures have been developed that aim to overcome this compromise, including bulk heterojunctions,[16] depleted bulk hetero-junctions,[17-21] and electrode structuring/geometry-based techniques as we discussed in chapter 1. So far, the attempts of bulk heterojunction though were demonstrated to overcome limited charge transport by reducing the effective electrode-electrode distance, its many-fold increase of the junction has

lessened open-circuit voltage due to heightens the bimolecular recombination at the increased interface area.[22] Therefore, they have not yet led to net power conversion efficiency advances.[23,24] Work on the nanostructures for the enhancement of solar cell performance has been extensively explored, such as nanowires,[20,25] nanopillars,[26] and pyramid arrays.[27, 28] By introducing a pillar structured electrode in PbS QD based solar cells, a 20% improvement in J_{SC} has been demonstrated vs its flat counterpart by Kramer's group, resulting in an efficiency of 5.6%.[26] Labele et al. have reported that by processing a hierarchical structured electrode, a 24% increase in J_{SC} and an overall efficiency of 9.2% was achieved.[27]

In this chapter, firstly, we'll discuss the benefits of introducing a simple grating structure in PbS CQD solar cells by performing full optoelectronic simulations. Secondly, the nanofabrication methods used to realize this nanostructure were discussed. At last, a case study was conducted to experimentally investigate the device performance of PbS CQD solar cells with periodic submicron grating structures compared to that of the planar cells.

2.2 Modeling Photovoltaic Performance in Periodic Patterned PbS CQD Solar Cells

2.2.1 Theoretical Basis

Although various computational methods have been applied to simulate and understand the operational electronic mechanisms in solar cells,[29-32] specific to CQD heterojunction solar cells, the simulations of complete optical generation and transport process that employing optical absorption calculation are rare.[24] In our work, by employing COMSOL Multiphysics-finite element analysis method, we applied both the light absorption distribution and the carrier generation rate into our 2D model and combined the photogeneration with the carrier transport and recombination processes to obtain accurate calculations of both the photonic and electronic characteristics of CQD heterojunction solar cells.[33,34]

The optical field distribution in the solar cells was calculated by applying Maxwell's equations in a unit cell surrounded by Floquet–Bloch boundaries. A normal incident monochromatic plane wave was used as the light illumination, while the input sun energy was swept from 350 to 1160 nm wavelengths with an

input power distribution according to the AM 1.5G solar reference spectrum. Both polarizations of light were considered and averaged for each wavelength. The local wavelength dependent carrier generation profile was obtained from the light absorption distribution utilizing the equation (1.5).

Next, the generation distribution obtained from the optical calculation was transferred to the electronic transport equation system. The electric potential, charge carrier transport, recombination, and collection processes were comprehensively calculated, based on Poisson's equation and the carrier diffusion equations as below:

$$\nabla^2\Phi = \frac{q}{\varepsilon_0\varepsilon_r}(n - p - N) \tag{2.1}$$

where q is the electronic charge; ε_0 is the vacuum permittivity; ε_r is the relative permittivity of the CQD material; n and p are the electron and hole concentrations, respectively; and the impurity concentration, $N \equiv N_d - N_a$, is defined as the sum of the concentrations of ionized donors N_d and the acceptors N_a

$$\nabla\left[-D_n\nabla \mathrm{n} + \mathrm{n}\mu_n\left(\frac{\nabla\chi}{q} + \frac{K_BT}{q}\nabla \ln N_c\right)\right] = \mathrm{G(x,y)} - \mathrm{R} \tag{2.2}$$

$$\nabla\left[-D_p\nabla_p - \mathrm{p}\mu_p\left(\nabla\Phi + \frac{\nabla E_g}{q} + \frac{\nabla\chi}{q} + \frac{K_BT}{q}\nabla \ln N_v\right)\right] = \mathrm{G(x,y)} - \mathrm{R} \tag{2.3}$$

where$D_n = \frac{\mu_n K_B T}{q}$, $D_p = \mu_p K_B T/q$ are the electron and hole diffusion coefficient, respectively; μ_n and μ_p are the electron and hole mobility; χ is the electron affinity; E_g is the semiconductor bandgap; K_B is Boltzmann's constant; T= 300 K is the operating temperature; and R is the carrier recombination rate. $N_c = [m_c K_B T/(2\pi\hbar^2)]^{3/2}$, $N_v = [m_v K_B T/(2\pi\hbar^2)]^{3/2}$ are the effective conduction and valence band density of states, respectively, where m_c and m_{cv} are the conduction and valence band effective mass, and $\hbar$ is the reduced Planck's constant.

In particular, for the recombination term, we employed the classic Shockley–Read–Hall expression which explicitly accounted for a trap density given as

$$R_{srh} = \frac{np - n_i^2}{\tau_n(p + p_t) + \tau_p(n + n_t)} \tag{2.4}$$

where τ_n and τ_p are the electron and hole lifetime; n_t and p_t are the concentration of the trap state of electron and hole, respectively. $n_i = [N_c N_v \exp(-qE_g/K_B T)]^{1/2}$ is the intrinsic carrier concentration. In this model, excess carriers recombine by interacting through those intermediate centers. The electrical contacts that constituted the upper and lower boundary of device were considered as ideal ohmic contacts, which meant that the carrier concentrations were at their thermal equilibrium values at these points.

2.2.2 Results and Discussion

In previous discussion, a compromise existed between the light absorption and charge carrier extraction has already been elaborated in flat QDPV devices. To overcome this limit without expecting the materials improvements, one of the solutions is to go beyond 1D flat device and create a cell structure that can capture more light without upsetting the electronic performance. Here we proposed a simple grating structure that should realize the goal, since in this structure the flat film could be ideally wrapped around in a conformal fashion in which more absorbing materials per unit of effective cross area were packed without upsetting the transport length limit.

To verify this idea, the solar cells were modeled in two different architecture with layers of ITO/TiO_2/PbS/MoO_3/Ag on a glass substrate. One was conventional flat layered structure (Figure 2.1a) and the other was the grating structured solar cell (Figure 2.1b). For the flat "control" devices, the ITO and TiO_2 layers were 90 nm and 10 nm thick respectively, while the thicknesses of the top electrode layers, MoO_3 and Ag, were 10 nm and 60 nm, respectively. For the grating devices, on top of a glass substrate, a first flat ITO layer was layered for bottom contact. The grating was then defined by a transparent periodic optical dielectric covered by a second ITO coating and TiO_2 coating. The total thickness of the two ITO layers was always > 90 nm where they met, which corresponded to the thickness of the ITO of the flat solar cells. The subsequent layers were coated onto the ITO-TiO_2 grating in the same sequence as in the flat one. The first ITO layer, MoO_3, and metal contact thicknesses was set to the same values as used in the flat devices, while allowing for optimization on the PbS thickness, grating height and pitch, as well as the thickness of the

electronically active TiO_2 and second layered ITO. The electronic parameters of PbS and TiO_2 which constitute the p-n junction are listed in Table 2.1 and were obtained from literature sources.[35-38]

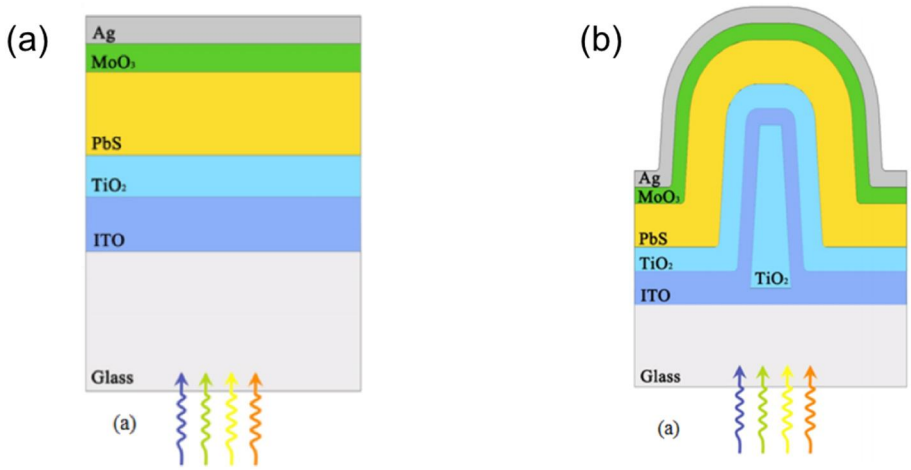

Figure 2.1 The schematic diagram of (a) flat PbS based solar cells, (b) patterned PbS solar cells.

Table 2.1 Parameters employed in simulations of PbS solar cells.

	PbS	TiO_2
Doping ($1/cm^3$)	10^{16} [4]	5×10^{17} [4]
Band-gap (eV)	1.3 [5]	2.4 [5]
Affinity (V)	3.8 [5]	4.1 [5]
Electron Mobility ($cm^2/(Vs)$)	10^{-2} [9]	1 [19]
Hole Mobility ($cm^2/(Vs)$)	10^{-2} [9]	1 [19]
Electron Lifetime (s)	2×10^{-7} [9]	10^{-5} [19]
Hole Lifetime (s)	2×10^{-7} [9]	10^{-5} [19]

The comparison of light absorption and photocarrier generation in patterned and flat PbS QD solar cell are shown in Figs. 2.2. For the light absorption (Figure 2.2a and b), with optimized geometry values (Table 2.2) the PbS layer of grating patterned device can absorb more than 90% of the light in the visible and retain above 80% up to the end of the infrared absorption, which was much higher than that in the flat devices even with thicker PbS films. The carrier generation rates per unit area as a function of the effective PbS thickness in both the flat and patterned PbS solar cells are shown in Fig. 2.2c. It clearly indicates that the patterned device generated more photo-generated carriers than the flat one of the same PbS volume and

which was most likely the result of high localization of the optical field in the grating structure. In Figs. 2.2d and e, this assumption was confirmed, since the absorption in the device with grating structure showed obvious enhancement in the grooves area.

Table 2.2 Optimized Geometry Parameters of Patterned PbS solar cells (nm).

Pitch	960
Flat ITO	80
Patterned ITO	10
TiO_2	10
PbS	230
MoO_3	10
Ag	60
Height	2000

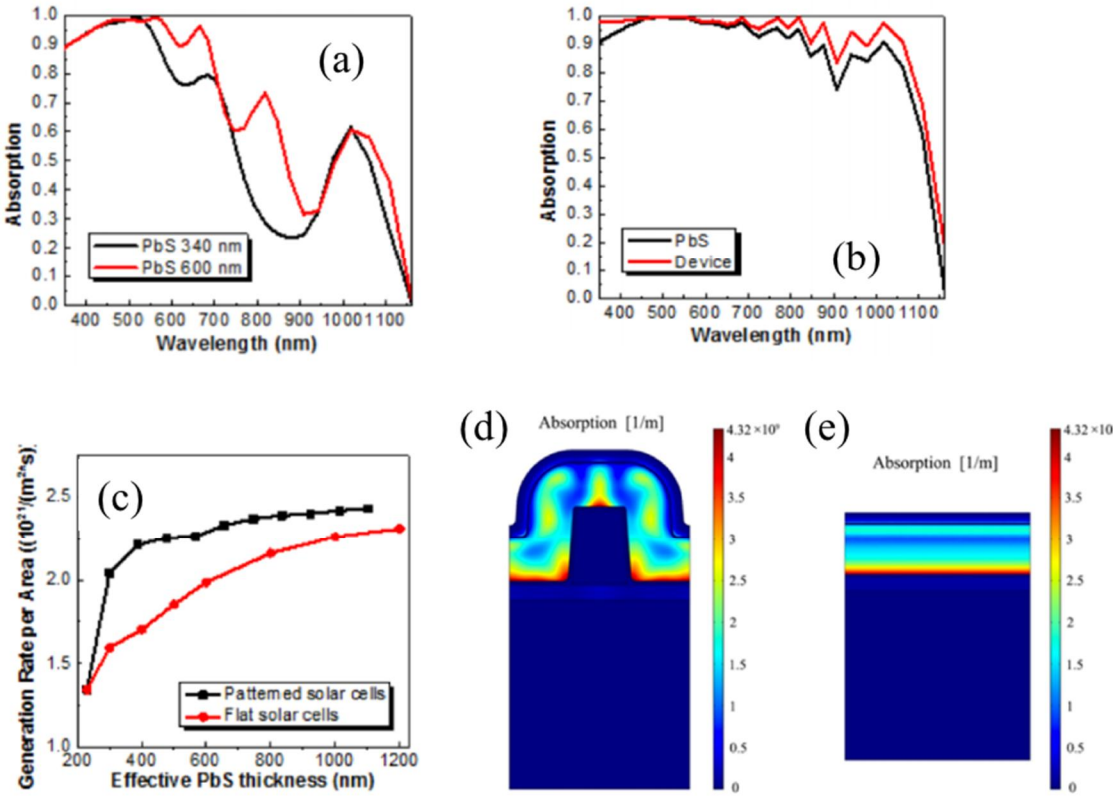

Figure 2.2 The absorption spectrum of (a) flat PbS solar cells, (b) patterned PbS solar cells. (c) Generation rate per unit area as a function of effective PbS thickness in patterned and flat devices. (d) and (e) are Optical absorption in patterned and flat devices with 388 nm effective thickness.

The J_{SC}, PCE, V_{OC} and FF as a function of PbS thickness in both flat and grating patterned devices are shown in Figure 2.3. Comparing to the flat devices, the J_{SC} of patterned device was saturated at about 35.2 mA/cm^2, which was a 71% increase than that of the flat device. Accordingly, the PCE of the grating device showed a maximum value of 11.2%, which was a 50% of increase compared to that in flat device. It's worth noting that the maximum J_{SC} of grating device was achieved with a PbS thickness of 230 nm and which was smaller than the thickness of the optimized flat cell (as shown in Figure 2.3 a and b, the J_{SC}, V_{OC} and PCE all reached the highest values at 340 nm). It implies that the benefits of the patterned structure can only be achieved by keeping the PbS thickness within the transport length.

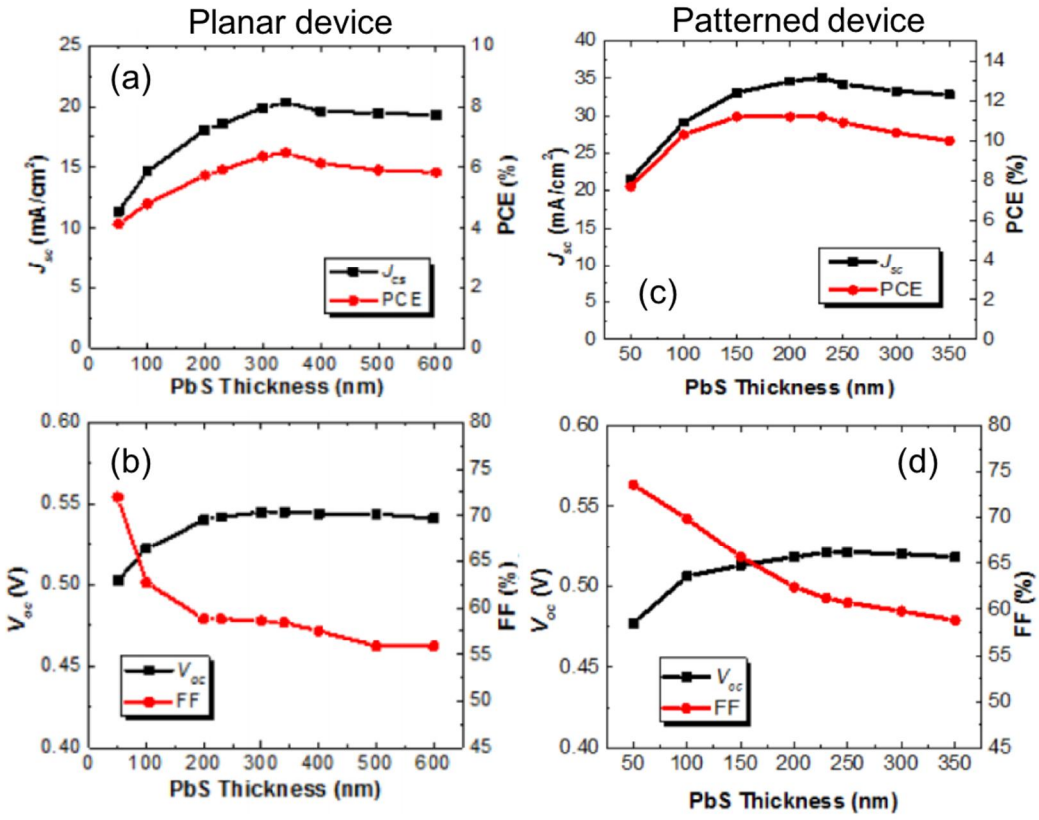

Figure 2.3 Simulation results in flat PbS solar cells: (a) J_{SC} and PCE, (b) V_{OC} and FF as a function of PbS thickness, and in grating PbS solar cells: (c) J_{SC} and PCE, (d) V_{OC} and FF as a function of PbS thickness.

The J_{SC}, PCE, V_{OC} and FF as a function of grating height with all the other parameters set to the optimized values are shown in Figure 2.4a, b. In Figure 2.4a, it shows that the PCE follows the J_{SC} improvements with the increase of grating, reaching a peak value of 11.2% when the grating height is 2 μm. For the FF,

although the simulations result indicates that in the short grating structure, it is lower than that of the flat device, it continues to increase slightly with the grating height increase, as shown in Figure 2.4b. It's convincible that the FF doesn't decrease since the thickness of the PbS layer maintains the same, the electric filed does not decrease when the grating height is increased. However, why does the FF increase? From 2.4 c and d, the reason behand was uncovered, in which the 2D electric field intensity in the grating device with 400 nm and 2000nm height is displayed. As shown from the figure, with larger grating height, the electric field intensity is stronger. In fact, with larger grating height, there is a stronger light absorption localization on the top and bottom of the grating near the heterojunction interface, which heightens the electric field intensity and hence the FF slightly.

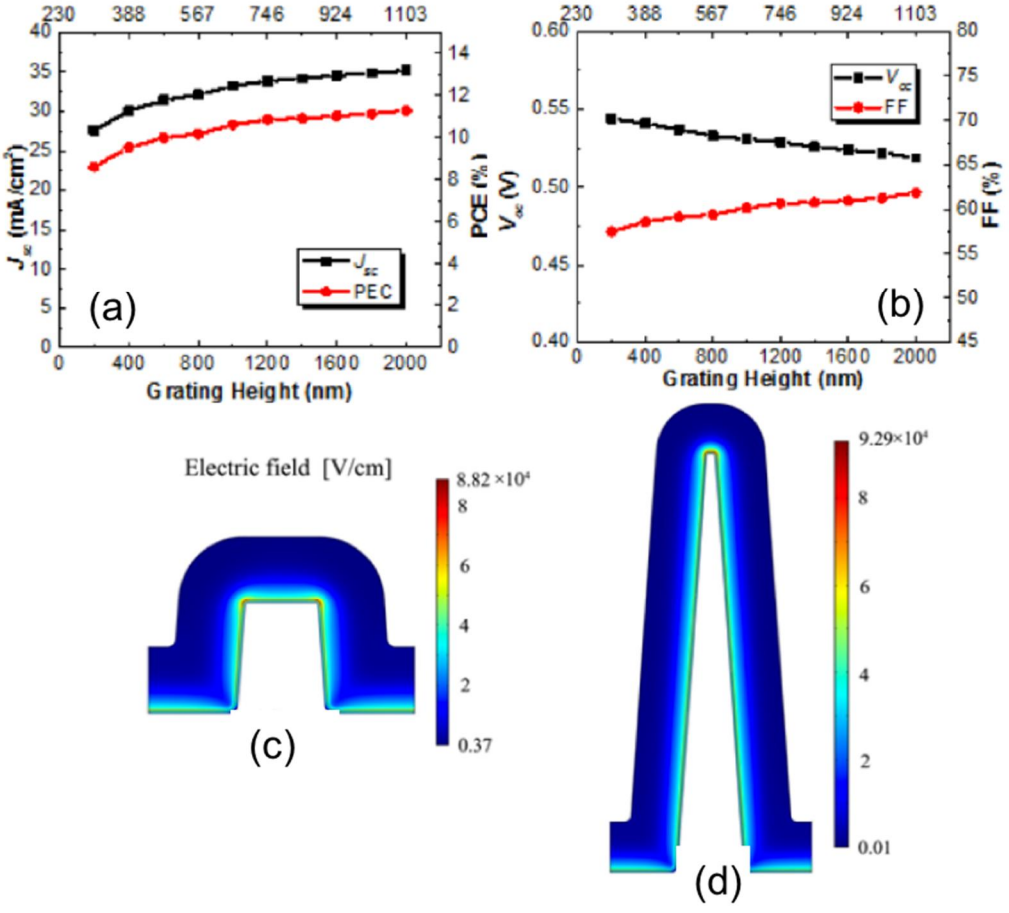

Figure 2.4 Simulation results in grating PbS solar cells: (a) JSC and PCE, (b) VOC and FF as a function of grating height. (c) and (d) electric field at the Mpp condition in grating device with 400 nm and 2000 nm grating height.

2.3 Nanofabrication of Periodic Grating Structures

Since periodic nanostructures are of increasing interest in many fields such as nanotechnology and biotechnology, and are expected to provide new devices, such as antireflective optical elements,[39] photonic crystals,[40] biomaterials[41] and magneto-electronic devices,[42] a number of techniques have been used to fabricate such structures.[41–48] The most common approaches involve using electron-beam or nanoimprint lithography.[45, 47] However, these techniques have limitations in throughput, encountering problems of either small patterning area, low speed, and/or high cost of equipment and moulds.[45] In contrast, maskless laser interference lithography (LIL) allows fast and large area periodical structures to be patterned with simple equipment.[46]

In a two beam LIL method, a periodic grating pattern is formed by intersecting two coherent plane waves which can be recorded on photoresist layer. The period P of the resultant interference pattern depends on the wavelength of the light λ of the laser used, and the angle θ, at which the two beams interfere:

$$\mathrm{P} = \frac{\lambda}{2sin\theta} \tag{2.5}$$

Two experimental arrangements are widely used for two-beam LIL. The first which utilizes a Lloyd's mirror interferometer is shown in Fig. 2.4a.[47] This is a simple corner cube arrangement where the left and right halves of the beam are folded onto each other. The incident angle can be tuned by rotating the Lloyd's mirror. However, there are some limitations arises for this set-up: (1) the incident angle could not be very large or small or the exposure area is quite limited; (2) excimer lasers which have low transverse coherence cannot be used since the two halves of such beams are not mutually coherent and therefore, cannot build up an interference pattern in a resist.

These problems can be minimized in the second arrangement which involves splitting one coherent beam into two portions using a beam splitter and then overlapping the two beams within the resist. (Fig. 2.4b).[47] The longitudinal coherence (narrow spectral width) of the laser source is important because the

distances from the beam splitter to the image plane can vary for the two beams. In the following experiments, a SureLock™ LM Series/ Compact Laser Modules with a single wavelength of 405 nm (with< 0.06nm linewidth) was employed for our LIL set-up.

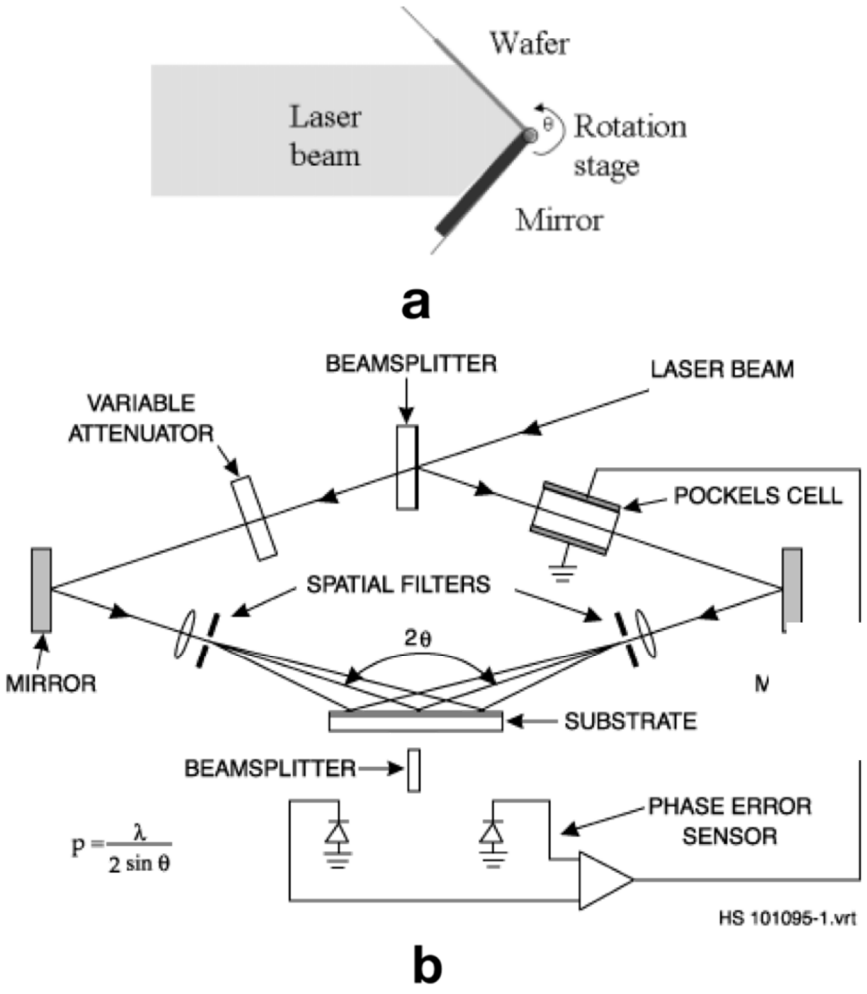

Figure 2.5 Schemes of two commonly used two-beam LIL setups. (a) A Lloyd's mirror configuration. (b) A two-beam configuration created by a beam splitter where one mirror is piezo-electrically controlled for phase stabilization.

Moreover, since the interference grating patterns are formed onto the photoresist layer, to obtained patterns with good quality and desired parameters (such as the pattern pitch and height), some other factors need to be carefully considered and controlled besides the incident angle of the beam during LIL process, including photoresist thickness, laser exposure dose and develop time.

2.4 Case Study： Building Proof-of-concept PbS Quantum Dot Solar Cells with Submicron Periodic Grating Structures

2.4.1 Fabrication of Grating Patterned PbS CQD Solar Cells

2.4.1.1 Synthesis of PbS Colloidal Quantum Dots

PbS quantum dots were synthesized following a modified version of the procedure from Hines et al.[49] Briefly, lead (II) oxide (0.450 g, 2 mmol), oleic acid (1.13 g, 4 mmol), and octadecene (14.0 g) were combined in a 50-mL, three-neck round bottom flask and stirred under vacuum at 100 °C for one hour (flask 1). Simultaneously, hexamethyldisilathiane (TMS) (0.211 mL, 1 mmol) and octadecene (4 g) were combined in a 25 mL, two-neck pear flask and degassed (flask 2). The lead mixture (flask 1) was placed under positive nitrogen flow and heated to 100 °C. The TMS mixture (flask 2) was injected rapidly into the lead mixture (flask 1) and allowed to stir for 1.5 minutes before the QDs were quenched in acetone and left overnight. The QD mixture was dispersed in six 15 mL centrifuge tubes and centrifuged (8500 rpm) using acetone (three times, 10 min, 10 min, 8 min) and methanol (two times, 8 min and 6 min) as the antisolvents. QDs were resuspended in minimal pentane between centrifugation cycles. The yield was 550 mg, and the QDs were stored dry until use. PbS QDs absorbed at 896 nm with a diameter of 2.9 nm as determined by the sizing curve from Moreels, et al. [50,51]

The preparation of metal halide precursors was following the procedure from Ip, et al.[10] For metal halide treatment, 1.0 ml metal halide precursor was introduced into the reaction flask after Sulphur source injection during the slow cooling process. A 6:1 Pb:Cd molar ratio was maintained during the synthesis. When the reaction temperature reached 30–35 °C, the nanocrystals were isolated by the addition of 60 ml of acetone then centrifugation. The nanocrystals were then purified by dispersion in toluene and reprecipitation with acetone/methanol (1:1 volume ratio), then re-dissolved in anhydrous toluene. The solution was washed with acetone two or three more times before final dispersal in octane (50 mg ml^{-1}).

2.4.1.2Nanofabrication of Grating Pattern

Commercial ITO (indium tin oxide) on glass was used as substrate in all the samples. Laser interference photolithography was then employed to create a submicron grating structure with either a pitch of 560 nm or 1 μm composed of a positive photoresist S1811, which was then to become a template for deposition of additional tantalum-doped TiO_2 ($Ta:TiO_2$). To fabricate the grating patterns with different height, the photoresist solution with different ratio of pure photoresist to thinner-P (solvent) was spin-coated with different speeds and time onto the commercial ITO substrates and followed by a prebaking step at 120 °C for 60 s. The photoresist film was then exposed to UV light with 405 nm laser in the interference lithography setup for 2−4 min and developed in MF319 developer for 5-15 s. $Ta:TiO_2$ was then deposited by pulsed laser deposition (PLD) under 10 mTorr of Oxygen for 10000 shots. The substrate was soaked in acetone for 15 min to remove the templated photoresist followed by annealing at 420 °C for 20 minutes to enhance the $Ta:TiO_2$ conductivity.

2.4.1.3 Fabrication of PbS Solar Cells

PbS CQDs were deposited onto both patterned and planar ITO via dip-coating using a layer-by-layer (LBL) deposition technique in the air (all fabrication steps in planar samples were identical to pattern devices, except for the lack of photo- lithography). The LBL technique consisted of the following deposition protocol. Substrates were dipped in four different solutions to deposit one layer of PbS film, namely (1) a ligand solution of 0.2% MPA in methanol as a linker solution, (2) 7.5 mg/mL PbS solution in hexane, (3) a ligand solution of 0.2% MPA in methanol as an exchange solution, and (4) pure methanol as a rinsing solution. For each solution, the substrates were immersed in for 5s, 20s, 15s, 5s and withdrawn at a speed of 1 mm/s, 10 mm/s, 10 mm/s, 10 mm/s followed by a drying time of 60s, 80s, 30s, 60s, respectively. This cycle was repeated 20-30 times to obtain desired thickness of PbS films. The film-coating processes were performed using a fully automated dip-coating machine. To form a photocathode, 25 nm of MoO_3, 50 nm of Au, and then 120 nm of Ag were subsequently deposited in a thermal evaporator at a base pressure of 10−6 mbar. Devices were prepared and tested in a nitrogen-filled glovebox (O2 <0.1 ppm, H2O < 0.1 ppm).

2.4.2 Results and Discussion

The SEM cross-section images of the devices with flat and grating architecture were shown in Figure 2.6. By adjusting the exposure dose and develop time during LIL process, the photoresist template of periodic grating structures with 560 nm pitch and 300 nm height was created. On top of that, the Ta:TiO_2 grating layers with an approximately 110 nm thickness were deposited. The PbS layer thickness was adjusted by the number of dip-coating cycles to be ~200-250 nm thick corresponding to 20 cycles. Then the subsequent layers of top contacts were deposited.

The current density-voltage (J-V) characteristics and EQE spectrum of the flat and grating devices measured under 1 sun illumination are depicted in Figure 2.7a. Their photovoltaic parameters are summarized in Table 2.3. Eight devices of each type were fabricated and tested for the data (Table 2.3). The performance figures were modest relative to champion devices published elsewhere. This was presumably because the charge transport in our QDs was more limited, but nevertheless we noted clearly different metrics for the different device types. Compared with flat PbS QD device, the J_{SC} of grating devices showed significant increase, which was 34% higher than that of the flat device. Given that the grating increased the volume of PbS per projected 2D area without affecting the charge collection dynamics, much of the current enhancement in Jsc should be attributed to the increased carrier generation in the extra volume. This was confirmed and illustrated in the EQE spectrum. (Figure 2.7b) As displayed from the figure, the EQE value of the grating device was obviously higher than that of the flat device within the whole wavelength region of 450−1200 nm. Particularly, this enhancement reached to the maximum with a more than two-fold increase of the EQE value around the PbS CQD's excitonic 900−1100 nm peak range. In addition, with the introduction of grating structure, the V_{OC} of the device increases by 12%. Consistently with the simulation that the FF in the grating device with short grating is lower than that of the flat device, overall the grating device gave an efficiency of 3.76%, which increased 35% compared to that of the flat device.

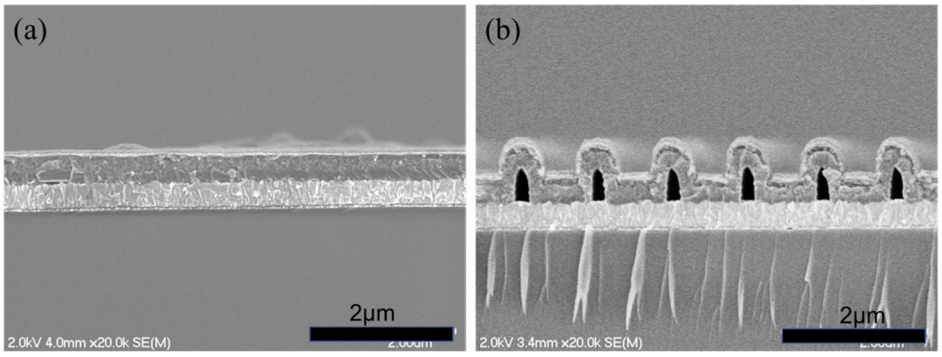

Figure 2.6 SEM cross-section images of (a) flat PbS solar cell, (b) grating patterned PbS solar cell with 560 nm pitch and 300 nm height.

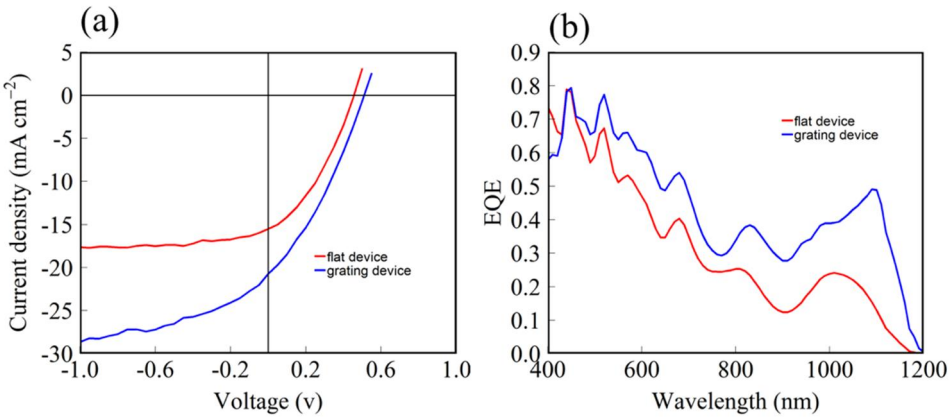

Figure 2.7 (a) J-V characteristics under 1 sun illumination. (b) EQE spectrum of both planar and grating PbS solar cells.

Table 2.3 Device performance parameters of solar cells measurement under AM 1.5 one sun illumination.

Device type	J_{sc} (mA/cm^2)	V_{oc} (V)	*FF* (%)	*Efficiency* (%)
Flat	16.94	0.45	36.03	2.78
Grating	22.62	0.51	32.58	3.76

Based on this, in the new round, a series of grating devices with different heights were development to try to approximately approach the optimal grating configuration that the simulation predicted. Figure 2.8 shows the cross-sectional SEM images of the flat and grating devices with 1 μm pitch and different grating heights. Again, by adjusting the coating thickness of photoresist layer as well as the exposure dose and

develop time during LIL process, the photoresist template of periodic grating structures with a height of 300 nm (small height), 600 nm (middle height) or 1200 nm (tall height) was created, respectively. On top of that, the subsequent layers were deposited with the same sequence and thickness. It's worth noting that these parameters were selected because of the facile fabrication, a step toward a truly optimized structure as modeled which required a larger structure height/pitch ratio to facilitate the optical absorption as well as the electrical performance of the device.

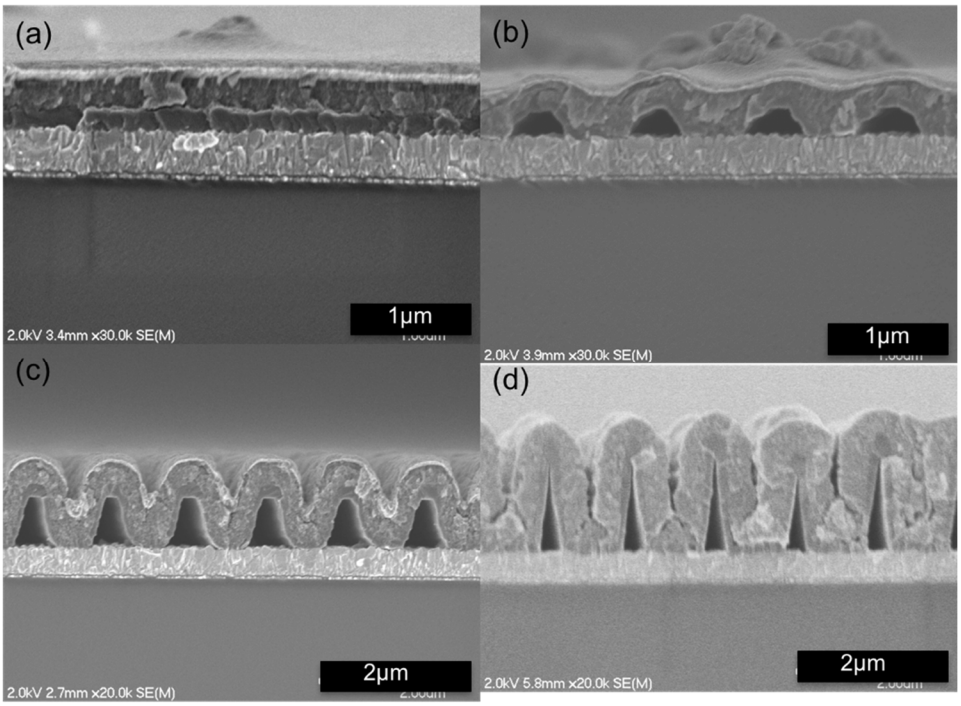

Figure 2.8 SEM cross-section images of (a) flat PbS solar cell, (b) grating patterned PbS solar cell with small height (300 nm), (c) grating patterned PbS solar cell with middle height (600 nm), and (d) grating patterned PbS solar cell with tall height (1200 nm)

The current density−voltage (J−V) characteristics and photovoltaic parameters of the flat and grating devices measured under 1 sun illumination are depicted in Figure 2.9a and Table 2.4, respectively. The detailed measurements presented below were taken for representative performers from the different groups. Compared with flat PbS QD device, the J_{SC} of grating devices showed different degrees of increase. Moreover, this enhancement reached maximum with a 20% increase when the grating height was approximately 600 nm. As predicted by the simulation, the carrier generation rate in the grating device was

enhanced by light-field localization, and which was stronger with larger grating heights. This was consistent with the measured absorption spectra of Figure 2.9b, whereas the absorption that occurred for wavelengths greater than 650 nm, especially near the PbS CQD's excitonic 900−1100 nm peak range, increased with the grating height. This enhanced light absorption over these wavelengths for the grating device is mirrored in the external quantum efficiency (EQE) spectra displayed in Figure 2.9c. Notably, the enhancement in EQE was achieved around the PbS CQD's excitonic peak that was centered at 958 nm, and with the grating height increase, the enhancement increased. This agrees well with the simulation result that the larger grating height resulted in higher J_{SC}. However, when considering the whole wavelength region, the J_{SC} obtained from the integration of EQE somehow didn't follow this trend since the J_{SC} of tall grating device decreased. This is most likely owning to the introduction of more defects and interfaces arises from nanofabrication and dip-coating process for grating device with tall height, resulting in more extrinsic recombination centers. Moreover, this may well explain why the grating devices had lower FF as well as the EQE decrease from 400- 750 nm wavelength compared to the planar devices. Overall, although the performance enhancement of the grating structure did not behave exactly as expected implied by simulation, with proper grating height, the grating structured device improved the power conversion efficiency by 6% over the planar geometry.

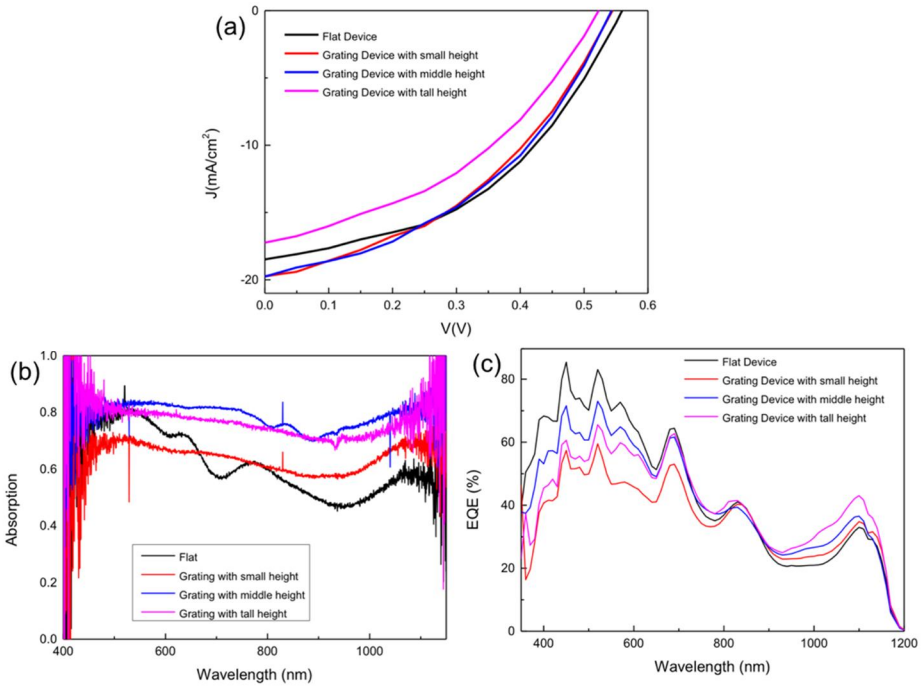

Figure 2.9 (a) J-V characteristics under 1 sun illumination, (b) Absorption spectrum, and (c) EQE spectrum of both planar and grating PbS solar cells with different grating heights.

Table 2.4 Device performance parameters of solar cells measurement under AM 1.5 one sun illumination.

Device type	J_{sc} (mA/cm^2)	V_{oc} (V)	*FF* (%)	*Efficiency* (%)
Flat	17.24	0.56	44.82	4.21
Small height	19.73	0.54	40.99	4.40
Middle height	19.76	0.54	41.62	4.47
Tall height	16.80	0.52	40.27	3.62

2.5 Conclusion

Geometry optimization is one of the important strategies to significantly increase the performance of CQD solar cells. In this chapter, a numerical simulation method that well combines both the photonic and electronic characteristics of CQD heterojunction solar cell is discussed and applied for the analysis of the performance of both 1D planar and 2D grating patterned TiO_2-PbS CQD heterojunction solar cells. The

electrical characteristics of the solar cell was calculated in the patterned PbS solar cells with different geometric parameters. With the optimal parameters for the grating structure, the optimized device showed significantly increase of the PCE, which reached to 11.2% with a J_{SC} of 35.2 mA/cm^2. Finally, as a case study, both planar and periodic grating patterned PbS CQD solar cells was successfully fabricated and tested. It demonstrated that with proper grating structure, the PCE as well as the J_{SC} of the device could be effectively improved, which agrees well with the simulation results. Inspired by the periodic grating pattern developed on the PbS CQD solar cells via laser interference photolithography, an expanding application of making superflexible transparent conductive Indium Tin Oxide (ITO) film and exploring its potential use in flexible optoelectronic will be discussed in the next chapter.

REFERENCES

(1) Research Cell Efficiency Records, National Renewable Energy Laboratory

http://www.nrel.gov/pv/assets/pdfs/best-research-cell-efficiencies-190416.pdf

(2) Wadia, C.; Alivisatos, A. P.; Kammen, D. M. Materials Availability Expands the Opportunity for Large-Scale Photovoltaics Deployment. *Environ. Sci. Technol.* **2009**, *43* (6), 2072–2077.

(3) Tang, J.; Brzozowski, L.; Barkhouse, D. A. R.; Wang, X.; Debnath, R.; Wolowiec, R.; Palmiano, E.; Levina, L.; Pattantyus-Abraham, A. G.; Jamakosmanovic, D.; et al. Quantum Dot Photovoltaics in the Extreme Quantum Confinement Regime: The Surface-Chemical Origins of Exceptional Air- and Light-Stability *ASC Nano* **2010**, *4* (2), 869–878.

(4) Chuang, C. H. M.; Maurano, A.; Brandt, R. E.; Hwang, G. W.; Jean, J.; Buonassisi, T.; Bulović, V.; Bawendi, M. G. Open-Circuit Voltage Deficit, Radiative Sub-Bandgap States, and Prospects in Quantum Dot Solar Cells. *Nano Lett.* **2015**, *15* (5), 3286–3294.

(5) Tang, J.; Wang, X.; Brzozowski, L.; Barkhouse, D. A. R.; Debnath, R.; Levina, L.; Sargent, E. H. Schottky Quantum Dot Solar Cells Stable in Air under Solar Illumination. *Adv. Mater.* **2010**, *22* (12), 1398–1402.

(6) Brown, P. R.; Kim, D.; Lunt, R. R.; Zhao, N.; Bawendi, M. G.; Grossman, J. C.; Bulović, V. Energy Level Modification in Lead Sulfide Quantum Dot Thin Films through Ligand Exchange. *ACS Nano* **2014**, *8* (6), 5863–5872.

(7) Luther, J. M.; Gao, J.; Lloyd, M. T.; Semonin, O. E.; Beard, M. C.; Nozik, A. J. Stability Assessment on a 3% Bilayer PbS/ZnO Quantum Dot Heterojunction Solar Cell. *Adv. Mater.* **2010**, *22* (33), 3704–3707.

(8) Gao, J.; Perkins, C. L.; Luther, J. M.; Hanna, M. C.; Chen, H.-Y.; Semonin, O. E.; Nozik, A. J.; Ellingson, R. J.; Beard, M. C. N-Type Transition Metal Oxide as a Hole Extraction Layer in PbS Quantum Dot Solar Cells. *Nano Lett.* **2011**, *11* (8), 3263–3266.

(9) Tang, J.; Kemp, K. W.; Hoogland, S.; Jeong, K. S.; Liu, H.; Levina, L.; Furukawa, M.; Wang, X.; Debnath, R.; Cha, D.; et al. Colloidal-Quantum-Dot Photovoltaics Using Atomic-Ligand Passivation. *Nat. Mater.* **2011**, *10* (10), 765–771.

(10) Ip, A. H.; Thon, S. M.; Hoogland, S.; Voznyy, O.; Zhitomirsky, D.; Debnath, R.; Levina, L.; Rollny, L. R.; Carey, G. H.; Fischer, A.; et al. Hybrid Passivated Colloidal Quantum Dot Solids. *Nat. Nanotechnol.* **2012**, *7* (9), 577–582.

(11) Chuang, C.-H. M.; Brown, P. R.; Bulović, V.; Bawendi, M. G. Improved Performance and Stability in Quantum Dot Solar Cells through Band Alignment Engineering. *Nat. Mater.* **2014**, *13* (8), 796–801.

(12) Xu, J.; Voznyy, O.; Liu, M.; Kirmani, A. R.; Walters, G.; Munir, R.; Abdelsamie, M.; Proppe, A. H.; Sarkar, A.; García De Arquer, F. P.; et al. 2D Matrix Engineering for Homogeneous Quantum Dot Coupling in Photovoltaic Solids. *Nat. Nanotechnol.* **2018**, *13* (6), 456–462.

(13) Carey, G. H.; Levina, L.; Comin, R.; Voznyy, O.; Sargent, E. H. Record Charge Carrier Diffusion Length in Colloidal Quantum Dot Solids via Mutual Dot-to-Dot Surface Passivation. *Adv. Mater.*

2015, *27* (21), 3325–3330.

(14) Clifford, J. P.; Konstantatos, G.; Johnston, K. W.; Hoogland, S.; Levina, L.; Sargent, E. H. Fast, Sensitive and Spectrally Tuneable Colloidal-Quantum-Dot Photodetectors. *Nat. Nanotechnol.* **2009**, *4* (1), 40–44.

(15) Zhitomirsky, D.; Voznyy, O.; Hoogland, S.; Sargent, E. H. Measuring Charge Carrier Diffusion in Coupled Colloidal Quantum Dot Solids. *ACS Nano* **2013**, *7* (6), 5282–5290.

(16) Rath, A. K.; Bernechea, M.; Martinez, L.; Pelayo Garcia De Arquer, F.; Osmond, J.; Konstantatos, G. Solution-Processed Inorganic Bulk Nano-Heterojunctions and Their Application to Solar Cells. *Nat. Photonics* **2012**, *6* (8), 529–534.

(17) Kramer, I. J.; Zhitomirsky, D.; Bass, J. D.; Rice, P. M.; Topuria, T.; Krupp, L.; Thon, S. M.; Ip, A. H.; Debnath, R.; Kim, H.-C.; et al. Ordered Nanopillar Structured Electrodes for Depleted Bulk Heterojunction Colloidal Quantum Dot Solar Cells. *Adv. Mater.* **2012**, *24*, 2315–2319.

(18) Lan, X.; Bai, J.; Masala, S.; Thon, S. M.; Ren, Y.; Kramer, I. J.; Hoogland, S.; Simchi, A.; Koleilat, G. I.; Paz-Soldan, D.; et al. Self-Assembled, Nanowire Network Electrodes for Depleted Bulk Heterojunction Solar Cells. *Adv. Mater.* **2013**, *25*, 1769–1773.

(19) Barkhouse, D. A. R.; Debnath, R.; Kramer, I. J.; Zhitomirsky, D.; Pattantyus-Abraham, A. G.; Levina, L.; Etgar, L.; Grätzel, M.; Sargent, E. H. Depleted Bulk Heterojunction Colloidal Quantum Dot Photovoltaics. *Adv. Mater.* **2011**, *23*, 3134–3138.

(20) Wang, H.; Kubo, T.; Nakazaki, J.; Kinoshita, T.; Segawa, H. PbS-Quantum-Dot-Based Heterojunction Solar Cells Utilizing ZnO Nanowires for High External QuantumEfficiency in the Near-Infrared Region. *J. Phys. Chem. Lett.* **2013**, *4*, 2455–2460.

(21) Jean, J.; Chang, S.; Brown, P. R.; Cheng, J. J.; Rekemeyer, P. H.; Bawendi, M. G.; Gradeak, S.; Bulović, V. ZnO Nanowire Arrays for Enhanced Photocurrent in PbS Quantum Dot Solar Cells. *Adv. Mater. 2013*, *25*, 2790–2796.

(22) Kemp, K. W.; Labelle, A. J.; Thon, S. M.; Ip, A. H.; Kramer, I. J.; Hoogland, S.; Sargent, E. H. Interface Recombination in Depleted Heterojunction Photovoltaics Based on Colloidal Quantum Dots. *Adv. Energy Mater.* **2013**, *3* (7), 917–922.

(23) Barkhouse, D. A. R.; Debnath, R.; Kramer, I. J.; Zhitomirsky, D.; Pattantyus-Abraham, A. G.; Levina, L.; Etgar, L.; Grätzel, M.; Sargent, E. H. Depleted Bulk Heterojunction Colloidal Quantum Dot Photovoltaics. *Adv. Mater.* **2011**, *23* (28), 3134–3138.

(24) Adachi, M. M.; Labelle, A. J.; Thon, S. M.; Lan, X.; Hoogland, S.; Sargent, E. H. Broadband Solar Absorption Enhancement via Periodic Nanostructuring of Electrodes. *Sci. Rep.* **2013**, *3*, 2928.

(25) Park, H.; Chang, S.; Jean, J.; Cheng, J. J.; Araujo, P. T.; Wang, M.; Bawendi, M. G.; Dresselhaus, M. S.; Bulović, V.; Kong, J.; et al. Graphene Cathode-Based ZnO Nanowire Hybrid Solar Cells. *Nano Lett.* **2013**, *13* (1), 233–239.

(26) Kramer, I. J.; Zhitomirsky, D.; Bass, J. D.; Rice, P. M.; Topuria, T.; Krupp, L.; Thon, S. M.; Ip, A. H.; Debnath, R.; Kim, H. C.; et al. Ordered Nanopillar Structured Electrodes for Depleted Bulk Heterojunction Colloidal Quantum Dot Solar Cells. *Adv. Mater.* **2012**, *24* (17), 2315–2319.

(27) Labelle, A. J.; Thon, S. M.; Masala, S.; Adachi, M. M.; Dong, H.; Farahani, M.; Ip, A. H.; Fratalocchi, A.; Sargent, E. H. Colloidal Quantum Dot Solar Cells Exploiting Hierarchical

Structuring. *Nano Lett.* **2015**, *15* (2), 1101–1108.

(28) Labelle, A. J.; Thon, S. M.; Kim, J. Y.; Lan, X.; Zhitomirsky, D.; Kemp, K. W.; Sargent, E. H. Conformal Fabrication of Colloidal Quantum Dot Solids for Optically Enhanced Photovoltaics. *ACS Nano* **2015**, *9* (5), 5447–5453.

(29) Boardman, A. D.; Swain, S.; Establishment, R. R. Monte Carlo Determination of Electron Transport Properties in Gallium. **1990**, *31*, 1963–1990.

(30) Bandyopadhyay, S.; Klausmeier-Brown, M. E.; Maziar, C. M.; Datta, S.; Lundstrom, M. S. A Rigorous Technique to Couple Monte Carlo and Drift-Diffusion Models for Computationally Efficient Device Simulation. *IEEE Trans. Electron Devices* **1987**, *34* (2), 392–399.

(31) Stewart, R. A.; Ye, L.; Churchill, J. N. Improved Relaxation-Time Formulation of Collision Terms for Two-Band Hydrodynamic Models. *Solid State Electron.* **1989**, *32* (6), 497–502.

(32) Wexler, A.; Shaw, J. Numerical Analysis of Semiconductor Devices. *Adv. Water Resour.* **2003**, *4* (3), 146.

(33) Yang, K.; East, J. R.; Haddad, G. I. Numerical modeling of abrupt heterojunctions using a thermionic-field emission boundary condition. *Solid-State Electron.* **1993**, *36*(3), 321–330

(34) Barkhouse, D. A. R.; Gunawan, O.; Gokmen, T.; Todorov, T. K.; Mitzi, D. B. Device characteristics of a 10.1% hydrazine-processed $Cu_2ZnSn(Se,S)_4$ solar cell, *Prog. Photovolt. Res. Appl.* **2012**, *20*(1), 6–11.

(35) Maraghechi, P.; Labelle, A. J.; Kirmani, A. R.; Lan, X.; Adachi, M. M.; Thon, S. M.; Hoogland, S.; Lee, A.; Ning, Z.; Fischer, A.; et al. The Donor-Supply Electrode Enhances Performance in Colloidal Quantum Dot Solar Cells. *ACS Nano* **2013**, *7* (7), 6111–6116.

(36) Pattantyus-abraham, A. G.; Kramer, Ḱ. I. J.; Barkhouse, Ḱ. A. R.; Wang, X.; Konstantatos, G.; Debnath, R.; Levina, L.; Raabe, I.; Nazeeruddin, M. K.; Sargent, E. H. Depleted-Heterojunction Colloidal. **1800**, *4* (6), 3374–3380.

(37) Zhitomirsky, D.; Voznyy, O.; Levina, L.; Hoogland, S.; Kemp, K. W.; Ip, A. H.; Thon, S. M.; Sargent, E. H. Engineering Colloidal Quantum Dot Solids within and beyond the Mobility-Invariant Regime. *Nat. Commun.* **2014**, *5* (May), 1–7.

(38) Tang, J.; Liu, H.; Zhitomirsky, D.; Hoogland, S.; Wang, X.; Furukawa, M.; Levina, L.; Sargent, E. H. Quantum Junction Solar Cells. *Nano Lett.* **2012**, *12* (9), 4889–4894.

(39) Paivanranta, B.; Baroni, P.; Scharf, T.; Nakagawa, W.; Kuittinen, M.; Herzig, H.P. Antireflective nanostructured microlenses. *Microelectron. Eng.* **2008***, 85*, 1089–1091.

(40) Zhang, X.; Liu, S.; Liu, Y. Fabrication of large-area 3D photonic crystals using a holographic optical element. *Opt. Laser Eng.* **2006**, *44*, 903–911.

(41) Yu, F.; Li, P.; Shen, H.; Mathur, S.; Lehr, C.; Bakowsky, U.; Mücklich, F. Laser interference lithography as a new and efficient technique for micropatterning of biopolymer surface. *Biomaterials*, **2005**, *26*, 2307–2312.

(42) Moralejo, S.; Castaño, F. J.; Redondo, C.; Ji, R.; Nielsch, K.; Ross, C.A.; Castaño, F.; Magn, J. Fabrication and magnetic properties of hexagonal arrays of NiFe elongated nanomagnets. *Magn. Mater.* **2007**, *316*, 44–47.

(43) Beesly, M.J.; Castledine, J. G. The use of photoresist as a holographic recording medium. *Appl. Opt.* **1970**, *9*, 2720–2724.

(44) Zaidi, S.H.; Brueck, S. R. High aspect-ratio holographic photoresist gratings. J. *Appl. Opt.* **1988**, *27*, 2999–3002.

(45) Harriott, L.R. Limits of lithography. *Proc. IEEE*, **2001**, *89* (3), 366–374.

(46) Lasagni, A.; Holzapfel, C.; Weirich, T.; Mucklich, F. Laser interference metallurgy: A new method for periodic surface microstructure design on multilayered metallic thin films. *Appl. Surf. Sci*. **2007**, *253*, 8070–8074.

(47) Divliansky, I.B.; Shishido, A.; Khoo, I.; Mayer, T.S.; Pena, D.; Nishimura, S.; Keating, C. D.; Mallouk, T. E. Fabrication of two-dimensional photonic crystals using interference lithography and electrodeposition of CdSe. *Appl. Phys. Lett*. *2001*, *79* (21), 3392–3394.

(48) Kurihara, K.; Nakano, T.; Ikeya, H.; Ujiie, M.; Tominaga, J. High-speed fabrication of large-area nanostructured optical devices*Microelectron. Eng*.**2008**, *85*, 1197–1201.

(49) Hines, M. A.; Scholes, G. D. Colloidal PbS Nanocrystals with Size-Tunable Near-Infrared Emission: Observation of Post-Synthesis Self-Narrowing of the Particle Size Distribution. *Adv. Mater.* **2003**, *15*, 1844–1849.

(50) Moreels, I.; Lambert, K.; Smeets, D.; Muynck, D. D.; Nollet, T.; Martins, J. C.; Vanhaecke. F; Vantomme, A.; Delerue, C.; Allan, G. ; Hens, Z. Size-Dependent Optical Properties of Colloidal PbS Quantum Dots. *ACS Nano* **2009**, *3*, 3023–3030.

(51) Kessler, M. L.; Starr, H. E.; Knauf, R. R.; Rountree, K. J.; Dempsey, J. L. Exchange equilibria of carboxylate-terminated ligands at PbS nanocrystal surfaces. *Phys. Chem. Chem. Phys.*, **2018**, *20*, 23649-23655.

Chapter 3 : Super-flexibility of ITO Electrodes via Submicron Patterning[1]

3.1 Introduction

Clear substrates coated with Indium tin oxide (ITO) thin films are ubiquitous as transparent conductive electrodes in liquid crystal displays (LCDs),[1,2] organic light-emitting diodes (OLEDs),[3-6] touch screens, thin-film transistors (TFTs),[7,8] solar cells,[9,10] e-paper, and sensors.[11] For several decades ITO and other transparent conductive oxides have fulfilled device performance requirements in terms of transparency and conductivity. Now ITO films face an important challenge: the technological push toward flexible devices require transparent electrodes on highly flexible and heat-sensitive polymer substrates. As with all oxide ceramics, ITO's inherent brittleness is a serious disadvantage for its incorporation in highly flexible electronics, since cracking and/or delamination will adversely impact the performance and lifetime of devices. Moreover, the high refractive index of ITO with its associated optical effects when deposited on polymer substrate cannot be ignored when employed in image display-related devices: In the visible spectrum, the refractive index of ITO is approximately 2.0, which gives rise to a strong reflection and diminished optical transparency for incident light on ITO coated polymer substrates.[12,13]

In order to overcome these challenges, researchers have considered radically different material alternatives for flexible transparent contacts such as single walled carbon nanotubes (CNTs),[14-17] graphene,[18-20] metal nanopatterns[21] or metal nanowires (NW),[12, 22-24] and hybrids of these.[25-27] While these materials have exhibited good durability when they were subjected to external mechanical stresses, there is an unavoidable compromise: the trade-off between high electrical conductivity and optical transparency.

[1]This chapter previously appeared as an article in the Journal of Applied Materials &Interfaces. The original citation is as follows: Dong, Q., Hara, Y., Vrouwenvelder, K. T., Shin, K. T., Compiano, J. A., Saif, M., Lopez, R. *ACS Appl. Mater. Interfaces*, **2018**, *10* (12), 10339–10346

And to improve the resistance of a layer, a thicker film is needed and this, in turn, lowers the transparency.

Therefore, ITO remains the industry's material of choice[12] and investigations on how to improve its mechanical properties has been focused on alternative ITO morphologies. ITO with nanoporous and nanoarray-based structures have attracted attention because of the relative independence of its conductivity and transparency. For ITO porous coatings, the most successful approach derives from depositing nanoparticles from solution to form a porous structure that effectively improves its optical transparency. But this methodology requires relatively high sintering temperatures to build up the interconnections between nanoparticles and achieve competitive levels of electrical conductivity. This high temperature step is an obstacle for heat-sensitive polymer substrates typically utilized in flexible optoelectronic devices. Approaches aimed at lowering the sintering temperature have been advanced in recent years.[28-32] Maksimenko *et al*., for instance, reported the fabrication of porous ITO coatings via a solution-based process with a relatively low sintering temperature of 130 °C.[31,32] A resistivity in the range of 10^{-1} Ω cm (with a sheet resistance of > 400 Ω sq^{-1}) and an optical transparency of 85− 90% were achieved. Yun *et al*. successfully deposited an ITO nanoarray on flexible heat-sensitive polyethylene terephthalate (PET) substrates at room temperature with further improvement in both electrical conductivity and optical transparency (a resistivity of approximately 2.3×10^{-3} Ω cm and a local transmission of about 99% at 550 nm).[33] Although these films demonstrated some improvement in their mechanical flexibility, they all failed catastrophically on reaching a bending curvature < 8 mm diameter. In summary, substantially better ITO mechanical flexibility together with smaller decrements in electrical and optical properties constitutes a technologically important goal to enable the utilization of transparent electrodes on heat-sensitive, soft polymer substrates.

In this chapter, we report on several advancements in developing a flexible transparent ITO conductive electrode on PET based on a spring architecture. Spring-like structures are a well-known mechanical solution for extension and contraction with minimum stress/strain. Thus, it is not surprising that such solution can be considered as a promising architecture for flexible electronic devices. Indeed, this approach

has been proven to add flexibility to important electronic brittle materials such as silicon.[34] Employing laser interference lithography, we initially fabricated a 1-dimensional (1-D) submicron grating structure to serve as the ITO-PET interface. Subsequently, a uniform ITO film was deposited on the nanopatterned structure at room temperature by conventional commercial sputtering deposition. The ITO micro-structured film showed superior flexibility and durability than its non-patterned counterparts, as well as other reported ITO flexibility-improved films. The bending diameter of curvature of the films was successfully tested down to 3.2 mm without cracking (this curvature target was suggested by our commercial ITO producing partners and it is the smallest we could test with our bending apparatus). Multiple samples were fabricated and evaluated with all of them showing, after 50 cycles of bending, relative electrical resistance changes within 20%, and in most cases below 3% (for reference, a standard flat film resistance increases > 100 times with a single bending cycle in this bending curvature). To expand its potential commercial applicability, this enhanced flexibility is also demonstrated in a 2-dimensional (2D) fashion, with resistance changes still below 50% after 50 cycles of bending over 2 perpendicular axes. All samples were subjected to multiple cycles of compression and decompression and maintained commercially required levels of electrical resistance and optical transparency. More importantly, with each bending cycle, the resistance changes got smaller. In the last, flexible and highly transparent conductive ITO film was incorporated into a PbS CQD solar cell and the device performance was characterized.

3.2 Nanofabrication of ITO Submicron Patterning

The substrate patterning and ITO deposition proceeded over two simple, already commercially employed steps as shown in Figure 3.1: (1) fabrication of the submicron structure with a photoresist; and (2) deposition of ITO onto the photoresist structure via sputtering. Since the spring-like structure needs to be transparent in the whole visible range, it must be fabricated with sub-optical wavelength dimensions to avoid angular diffractive effects. As already discussed in chapter 2, mask-less laser interference lithography (LIL) allows a fast and large area of periodical structures to be patterned with simple equipment[35] at great speed (a few seconds to few minutes depending on laser fluence, without the need of precision sample

placement). Adequate periodicity and the height of the spring-like structure was chosen by diffractive optics modeling and fabricated by controlling the exposure dose and angles between the two interference beams.[36]

The LIL process was carried out on positive photoresist S1811. In order to produce the structure with a specific height (180 nm in this study), the dilute photoresist solution was used, in which the ratio of pure photoresist to Thinner-P was 1:1 and 1:2 in volume, respectively. The photoresist solution was spin-coated at 7000 rpm for 40 s onto a PET substrate and followed by prebaking on the hot plate at 120 °C for 60 s. The photoresist coated film was then mounted in the interference lithography set-up and exposed to the UV laser with 405 nm wavelength for 4 min. After exposure, the substrate was dipped into MF 319 developer for 7 s right away, followed by washing step with deionized water, in which the substrate was rinsed for 7 s twice. After that, the substrate was dried with the N_2 flow. ITO was then deposited on the periodic grating pattern template comprising with photoresist on PET by roll-to-roll sputtering deposition at room temperature.

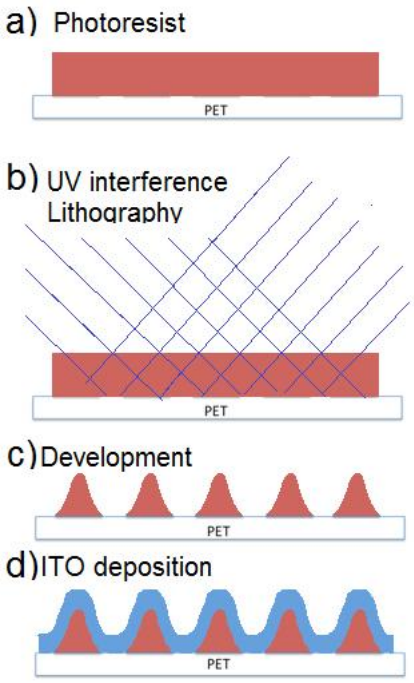

Figure 3.1 (a)-(d) the schematic of fabrication of ITO periodic grating pattern with LIL process.

3.3 Characterization of ITO Submicron Patterning

In our first realization of the structure, the ITO grating had a 285-nm periodicity and a total height of 230 nm (which includes the grating height of photoresist and the thickness of ITO layer). Figure 3.2a and b show the surface and cross-sectional micrographs of the ITO periodic submicron grating structure deposited on the PET substrates. The cross-sectional images of ITO periodic submicron grating structure were obtained using a scanning electron microscopy (SEM, Hitachi S-4700). The specimens were cross-sectioned in liquid nitrogen in order to minimize the tearing damage to the polymer substrate during the cutting process. As can be noted in the micrograph, the deposition of ITO on the grating template is quite uniform. Even though the aspect ratio (height /pitch) of the structure was ~ 0.9, the peaks and valleys of the grating were coated only slightly thinner than the control flat ITO layer.

The initial sheet resistance of ITO periodic submicron grating structure was determined by the mean value of at least three different measurements with the same condition by using a four-point probe system (Signatone1160 series probe station). The measured sheet resistance of all the ITO films on patterned PET substrates fabricated via the same conditions were approximately the same, with a deviation of 5%. The lowest sheet resistance observed was 209 Ωsq^{-1}, which corresponded to a resistivity of 1.4×10^{-3} Ω cm (this was calculated from the sheet resistance using the thickness of the ITO layer ~ 67 nm). Compared to the resistivity values previously reported for porous ITO films via solution-based process[31,32] and ITO nanoarray via sputtering-based process,[33] the sheet resistance of the ITO nanopatterned films analyzed in this study was at least 20% better. Relative to the control flat samples though, the electrical sheet resistance of the patterned specimens was approximately 10% higher. Taking the grating aspect ratio into account, this difference is understandable since the conductive path of ITO patterned structure was longer and its thickness was slightly thinner at the pattern walls than that of the flat sample, the introduced geometrical change must indeed induce a slightly higher sheet resistance.

3.4 Mechanical Flexibility of ITO Submicron Patterning

To test the mechanical flexibility and durability of the ITO periodic submicron grating structures, a high tensile or compressive stress to the ITO nanopattern via bending need to be applied. In our study, this process was realized via a lab-made bending station that comprised of two parallel plates with a programmable separation distance as illustrated in Figure 3.2c and d. During the forward and backward bending process, the electrical sheet resistance of the specimen was measured by four-point measurement via NI-4065 multimeter as a function of bending diameter of curvature, which was the distance between the two plates of the bending system. During the bending test, the sample was bent into given diameters of curvature in discrete small steps. At each diameter of curvature, the movement was paused to measure via 4-point probe the sheet resistance. The probes were spring set on the 4 corners of the square-shaped samples, relatively far from the strained region. Each bending cycle included compressing and decompressing steps. The test specimens were subjected to 50 bending cycles with the minimum bending diameter of curvature being 3.2 mm, that as mentioned earlier was limited by the apparatus range.

Figure 3.3a and b show the sheet resistance and the resistance change upon bending the first cycle for the flat control and the patterned 285-nm pitch ITO samples, respectively. The contrast can hardly be more dramatic, when the curvature diameter has decreased to barely 23.5 mm, the sheet resistance of flat ITO film has already undergone a very large 100-fold resistance increase. The post-test examination of this conventional ITO film under electron microscope showed that large cracks and some delamination (as shown in Figure 3.4) were responsible for the deteriorated resistance, leading to an irreversible catastrophic failure. In contrast, the ITO patterned sample stayed approximately the same all the way to the smallest possible bending in the instrument without any obvious structural change. The relative resistance change for the patterned ITO film was less than 1.6% after the first bending cycle.

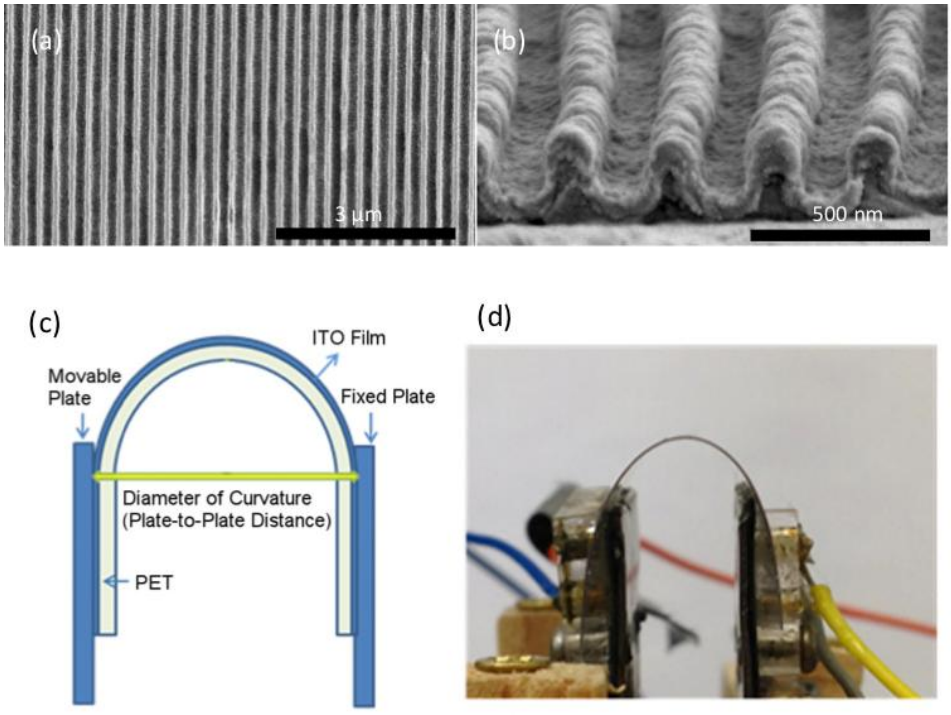

Figure 3.2 SEM surface image (a) and cross-section image (b) of the morphology of the ITO periodic grating patterns on the surfaces of the polymer substrates. (c) and (d) illustrated the schematic diagram and corresponding photograph of the bending system, respectively. Notice the film convex location relative to the substrate upon bending.

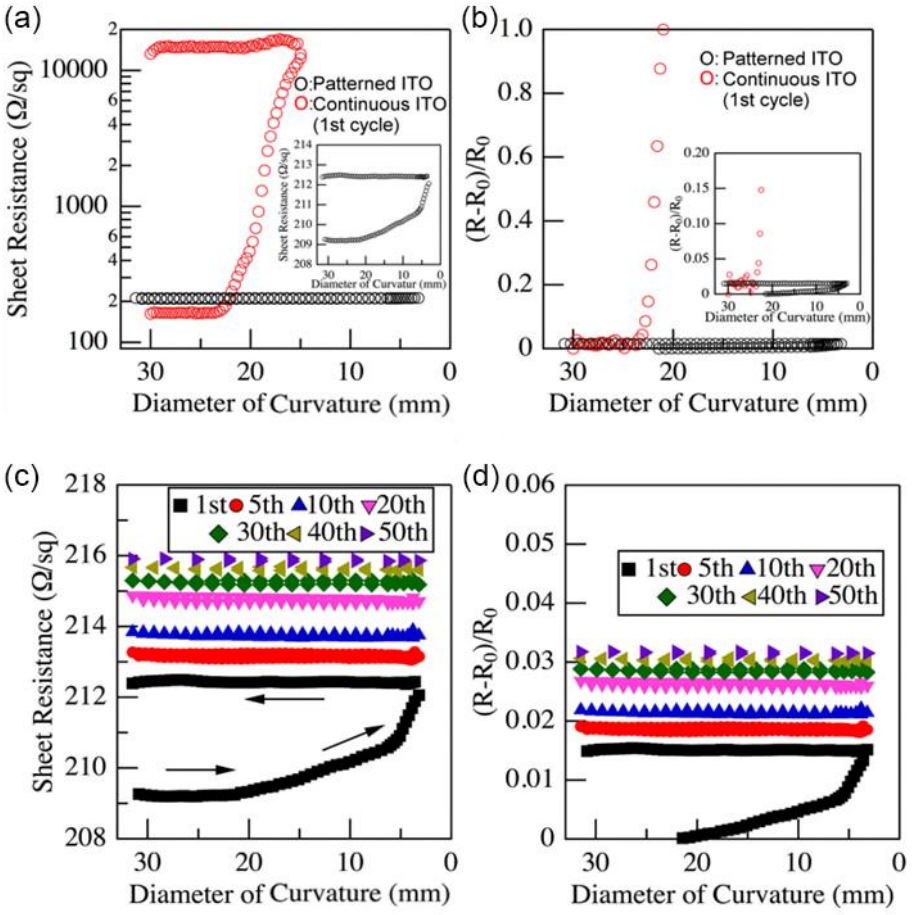

Figure 3.3 The comparison of the sheet resistance (a) and relative resistance increase (b) between ITO periodic grating patterns and continuous films on the surfaces of the polymer substrates as a function of diameter of curvature during the bending test. Insets show the magnified scale. Notice the film convex location relative to the substrate upon bending. The (c) sheet resistance and (d) relative resistance increase of the ITO periodic grating patterns on the surfaces of the polymer substrates during the cycling bending test. During each cycle, the minimum bending diameter of curvature was kept at 3.2 mm. And the specimen experienced 50 cycles of the reversible bending test.

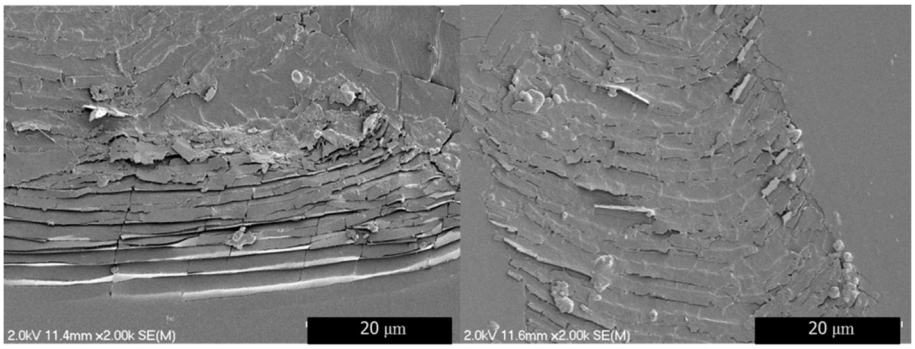

Figure 3.4 SEM images of the continuous ITO film after reversible bending test.

Remarkably, with < 2% resistance deterioration, this first bending cycle is the biggest single damaging event the films patterned with this nanostructure will suffer if continue evaluating over multiple consecutive bending tests. Figure 3.3c and d show the sheet resistance and relative resistance increase of this ITO film with the periodic submicron patterning over multiple bending cycles. The super flexibility and durability of this ITO patterned PET substrate are evident by reaching 3.2 mm diameter of curvature and surviving after cycling for more than 50 times with a negligible resistance change. The total accumulated damage (resistance change/initial resistance) is only 3.2%. We found out the resistance change per cycle is a decaying as a function of the number of cycles, thus in a conservative estimate utilizing the last resistance change measured between 40th-50th cycles, we can offer an upper ceiling to the sheet resistance change for further cycles to be $0.025\Omega sq^{-1}$/cycle. Given the small magnitude of this degradation rate, we can reasonably expect the film could keep performing over several hundreds to thousands of bending cycles without significant deterioration. The exact total of cycles it can live would naturally depend on the acceptable degradation of the particular application is being employed for.

How can such a simple structure make such a significant difference? The reasons why the structure is successful in extending the bending capability of ITO can be appreciated by looking at finite element analysis of the stress in the film upon stretching. Figure 3.5 presents the von Mises stress map for both ITO pattern and flat film undergoing the strain imposed by bending to the 3.2 mm diameter of curvature. For reference, the critical stress and stress for cracking ITO are $\sigma_c = 5.8\times10^5$ Pa and strain $\varepsilon_c = 0.005$

(experimentally determined by standard tensile tests in conventional films). The local von Mises stress in the ITO pattern has a spatial distribution that clearly depends on the geometrical details of the structure, but it is lower than the critical stress of ITO at all points. In contrast, the stress in the flat film is quite uniform but surpassing σ_c. This indeed indicates that during the bending process, the ITO pattern should survive at such small bending curvatures while the flat counterpart would never get there. In fact, the same simulation with strains produced under a 21-mm diameter curvature (the point that the continuous ITO film started to crack) on both of the continuous ITO film and ITO grating nanopattern (as illustrated in Figure 3.6) shows that indeed the flat sample should start to break around that strain level while the patterned ITO layer is far from it. All points of the generated stress map of the ITO patterned structure were much lower than σ_c in full agreement with the experimental observations presented above. Focusing again on the patterned sample stress map when bent to 3.2 mm diameter of curvature, one can also note that the stress distribution presents some "hot-spots" at the bending "knees" of the pattern. The reason for those is that in the tensile mode the stretching is carried out by flexing those "knees" of the spring with a combination of local tensile and compressive stresses. The presence of compressive stress even when stretching the structure is fully benign, as the material does not strain beyond its capability, but hinges around those points, presumably limiting the opening of cracks. Simulations confirm that the larger the aspect ratio of the spring structure, the smaller the flexing needed to accommodate the substrate strain. Therefore, the potential for cracking is inverse to the structure aspect ratio.

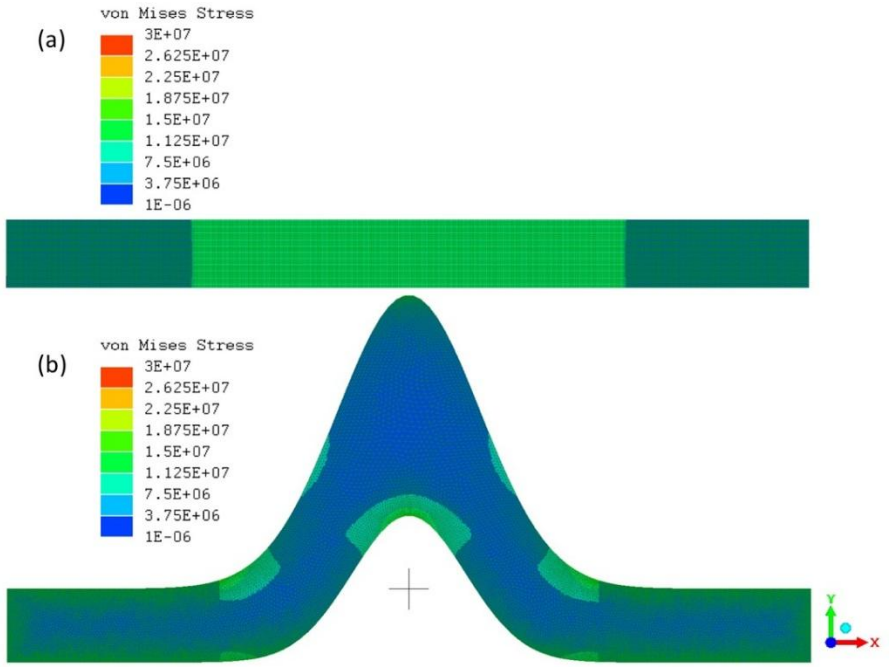

Figure 3.5 Tensile stress simulation of (a) continuous and (b) patterned ITO films with critical strain at 3.2 mm diameter of curvature. Stress in Pa units.

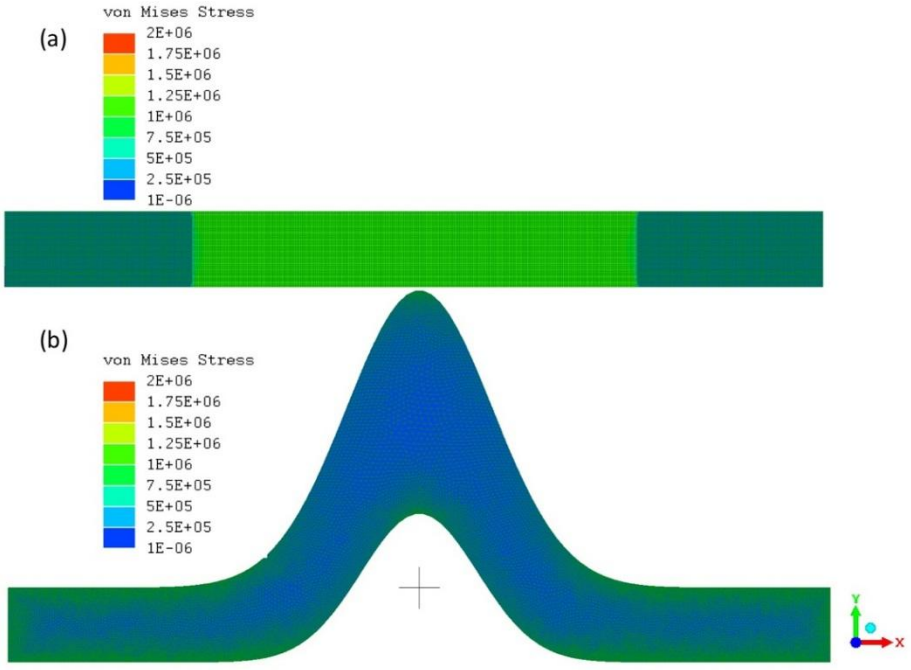

Figure 3.6 Tensile stress simulation of continuous and patterned ITO films with critical strain at 21 mm diameter of curvature. Stress in Pa units.

3.5 Optical Property of ITO Submicron Patterning

In addition to the electrical conductivity and mechanical flexibility, high transparency is another important property that should be preserved and/or enhanced in the transparent conductive oxide films. To achieve better antireflective (AR) characteristics in the application of optoelectronic devices, a possible solution inspired from nature is the moth-eye antireflective scheme.[37-39] Eyes and wings of certain species of moth are covered in arrays of tapered pillars with a nano-scale period and height. Since the array features are on a length scale smaller than the wavelength of the incident light, the tapering of the pillars causes the incident photons to experience a gradual change in refractive index from that of the incident medium to that of the substrate. This is a well-known effect that has been employed earlier by others focused on improving ITO optical properties. Specific to our study, the fabrication of the ITO grating pattern at the right length scale and with a suitable periodicity for the optical matching creates a bonus-added moth-eye anti-reflector. Compared to the conventional flat commercial ITO film, the ITO grating patterned films exhibited a higher transmittance in most the visible and near-infrared spectrum range (500~900 nm) as shown in Figure 3.7a.

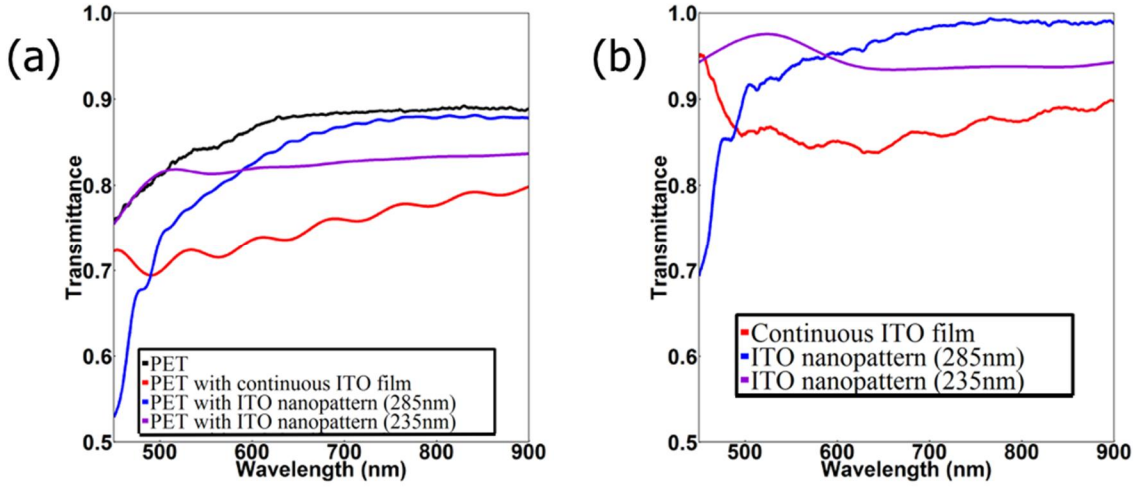

Figure 3.7 Comparison of (a) Specular transmittance of ITO with PET substrate and (b) local transmittance of ITO only in the form of ITO continuous film and different ITO nanopattern.

The 125 μm thick PET substrates used in this study present on their own a ~ 80 - 90% transmittance in the visible and near-IR range. When normalized at this PET transmittance (Figure 3.7b), the transmittance

of ITO nanopattern alone is above 90% in the visible range and reaches 98% at red region wavelengths. In contrast, the normalized transmittance for flat commercial quality ITO film is around 85% in the whole visible range. The only disadvantage presented by the 285-nm period patterned samples is a pronounced transmittance decrease in the blue region (450~500 nm). The type of photoresist present in the structure contributes to some spurious blue light absorption, but this blue deficiency is primarily caused because the moth-eye effect does not reach those very short wavelengths. In fact, the dip in blue light transmission is associated with a large reflection enhancement, indicating constructive interference in the reflection optical channel. It is indeed worth noting that the AR characteristics are very sensitive to the periodicity of the pattern when its geometrical features are not significantly smaller than the wavelength of light. As the blue-light drop could be very detrimental in some applications, correction to this issue could be obtained by decreasing the grating period. This was confirmed by optical simulations as shown in Figure 3.8, which predicts that when the periodicity of grating structure decreases to 235 nm the short wavelength optical impedance mismatch would shift to the UV region, disappearing accordingly of the visible range. Based on the simulation, an ITO periodic submicron grating structure with a periodicity of 235 nm was deposited on the PET substrates via the same methods mentioned before. This 2nd set of gratings have a total height of 90 nm (which includes the grating height of photoresist and the thickness of ITO layer). As shown in Figure 3.7a, the optical transmittance of the ITO grating pattern with 235 nm pitch showed a great improvement in the blue wavelength region. The optical transmittance is > 94% in the whole visible wavelength region (Figure 3.7b). It should be observed that compared to 285 nm-pitch ITO nanopattern, the transmittance of 235 nm-pitch ITO nanopattern ranging from 600 nm to 900 nm is ~5% lower. This near-IR drop is also predicted by the simulation shown in Figure 3.8. The analysis indicates that the transmission loss mainly arises from the reflection increase (no enhanced absorption), and both of them are connected with the sharpness of the high frequencies transmission dip.[40] During design simulations we noted this effect and in an ideal case, the transmission loss in blue wavelength region could be corrected without affecting the IR by decreasing only the pitch down to 190 nm without changing the pattern height. However, considering the required nanofabrication steps, such pitch and high aspect ratio were outside the dimensions we can

reliably fabricate. Therefore, a trade-off between the decrease of the pitch and height was made to realize optimal transparency in the visible range scarifying a small amount of near IR transmission.

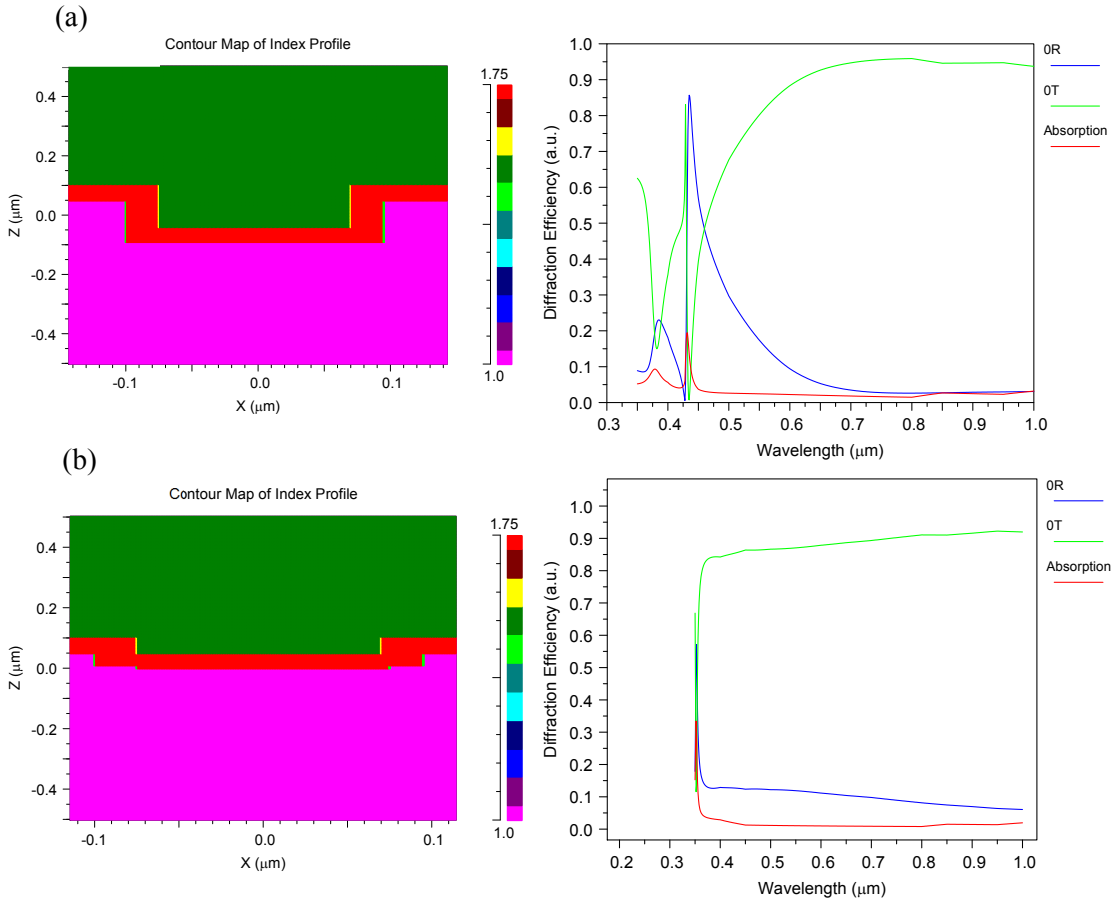

Figure 3.8 Simulated transmittance spectrum in (a) ITO grating pattern with 285 nm of periodicity and 180 nm of grating height; (b) ITO grating pattern with 235 nm of periodicity and 100 nm of grating height.

We can expect that the lower aspect ratio of the 235 nm pitch samples was also going to affect their bending performance. Upon testing for 50 bending cycles, the total accumulated resistance change went up to 35% relative to the initial value, which is still outstanding relative to the flat control samples, but relatively poor when compared to the 285 nm pitch ones. This lower aspect ratio (0.65) originated from limitations from the LIL step to create tall gratings with small pitch but also because the ITO film deposited was somewhat thicker (~ 90 nm as shown in Figure S6 in Supporting Information) than ideally designed (60 nm) for these particular set of substrates. It is easy to understand why these fabrication shortcomings

were deleterious: the 235 nm samples turned out to be simply "flatter", and as the simulation work showed, the mechanical properties are truly continuous between the flat and grating structures, favoring better strain handling with larger grating aspect ratios. Nevertheless, the sheet resistance increased slowly after each tensile cycle, with the first cycle being the biggest single damaging event the film suffered. As the cycles accumulated, the resistance change per cycle became smaller, resulting from the 40th to 50th cycle in a $0.1\Omega sq^{-1}$ sheet resistance increase per cycle. Importantly, although flatter, the smaller pitch samples showed no hint of the catastrophic failure typical of the flat control samples.

3.6 2D ITO Submicron Patterning

All those 1D patterned ITO films discussed in previous sections can only be bended safely perpendicular to the grating lines. When bended along the grating lines direction, naturally the film behaves identical as a flat conventional film, cracking catastrophically at relatively large bending curvatures. For most commercial applications, multi-axis bending is certainly more broadly desired if not essential. Clearly what is required is a generalization of the 1D grating into a 2D pattern. A simple 2D square array is not satisfactory as in between the rows of hills and valleys, there is expected to find un-interrupted orthogonal domains of regular flat regions connected from end to end in the sample. We tested examples of such naive design and their performance (not shown) was not superior to a regular flat film, suffering orders of magnitude resistance deterioration upon undergoing just one cycle in the bending test. A better approximation to the correct design is a 2D hexagonal nanopattern which does not present orthogonal flat domains. To realize it experimentally, the hexagonal array was fabricated by employing the LIL with a double exposure with the sample rotated 60° on its plane between exposures. Figure 3.9a shows the surface micrograph of the 2D hexagonal ITO periodic submicron grating structure deposited on the PET substrates. Figure 3.9b shows the relative resistance increase upon bending 25 cycles in two perpendicular directions successively (the 26th cycle labeled in Figure 5b represent the first cycle for the second direction). The accumulated relative resistance increase after 50 cycles was 48.4%. The higher relative resistance increase of this 2D ITO pattern was likely caused again by a somewhat lower aspect ratio mentioned above and also

by the contribution of continuous flat regions between the pattern hills. However, the diminishing relative resistance change with the increase of the number of bending cycles was observed once again, with a rate of deterioration ~ 0.2Ωsq^{-1}/cycle at the 50th bending test. By testing multiple samples, we randomized the alignment of the pattern relative to the axis of the bending instrument. The results showed small variations, but overall the flexibility and durability were independent to the bending directions in 2D. In other words, these mechanical properties were maintained no matter of the direction of the bending. In addition, given the small 235 nm pitch employed in the fabrication of this 2D sample, it also exhibited outstanding optical performance. The moth-eye effect described above effectively improved its transparency in the whole visible wavelength and made it comparable to that of the 1D grating patterned ITO structure fabricated with the same characteristic length as shown in Figure 3.10 a and b.

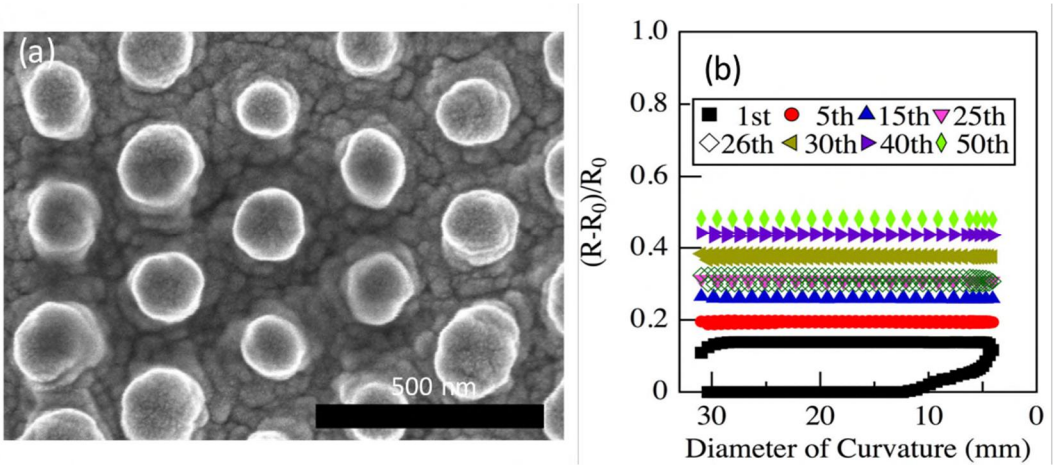

Figure 3.9 (a) SEM surface image of the morphology of the 2D ITO hexagonal nanopatterns on the surfaces of the polymer substrates. (b) The relative resistance increase of the 2D ITO hexagonal nanopatterns on the surfaces of the polymer substrates during the cycling bending test in two perpendicular directions. During each cycle, the minimum bending diameter of curvature was kept at 3.2 mm. And the specimen experienced 25 cycles of the reversible bending test for each direction.

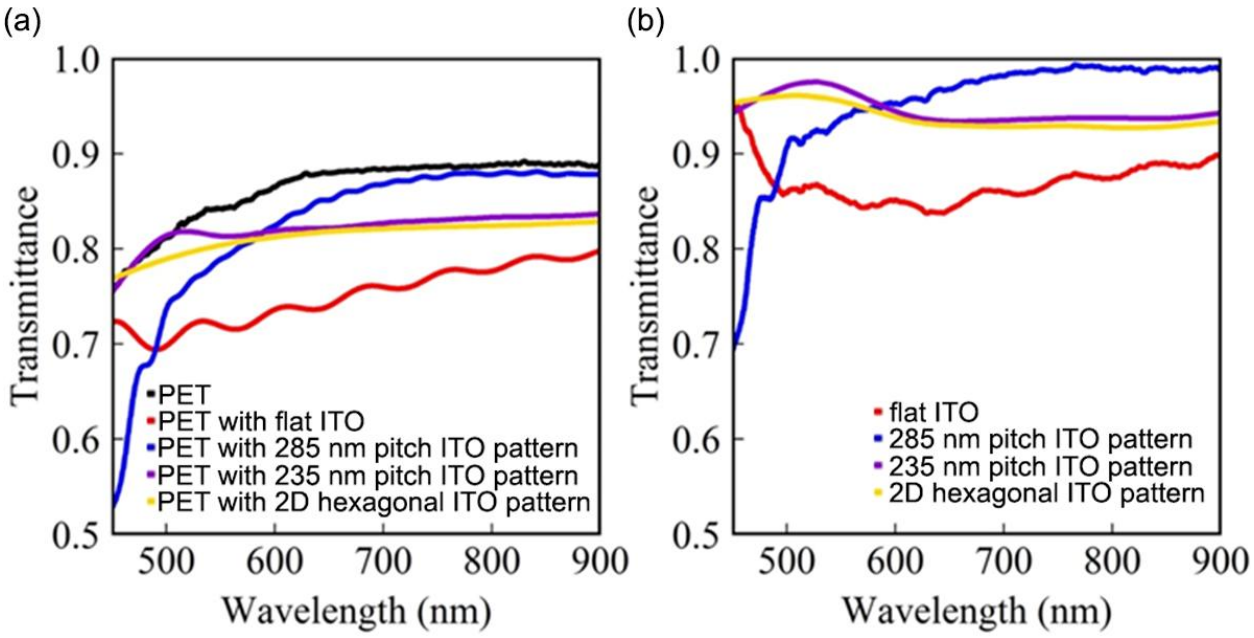

Figure 3.10 Comparison of (a) Specular transmittance of ITO with PET substrate and (b) local transmittance of ITO only in the form of ITO continuous film and different ITO nanopattern.

3.7 Case Study: Proof-of -concept Flexible PbS CQD Solar Cell

Glass substrates coated with Indium tin oxide (ITO) thin films have been ubiquitous exploited as transparent conductive electrodes in many optoelectronic applications. In previous sections, we have demonstrated that with optimized grating pitch and height, the patterned ITO-PET film exhibited superior flexibility and durability. The next question is, could it be incorporated into a real optoelectronic device and make it work? To answer this question, a patterned ITO-PET film was employed as the electrode to prepare the grating patterned PbS CQD solar cells. The optoelectronic performance as well as the flexibility of the device was tested afterwards.

It's worth noting that the "best" grating ITO pattern demonstrated in previous discussion was no longer optimal in particular for the solar cell application. As implied from the simulation results that discussed in chapter 2, a larger pitch is more favorable for the light absorption and thus result in a better performance in J_{SC} as well as the efficiency. Taking this into account, the new ITO grating pattern with a larger pitch of 560 nm and optimized height was fabrication to use in solar cells.

Before incorporating it into the device fabrication, a cycling bending test was conducted on the patterned ITO- PET film to verify its flexibility and durability. The structure of the pattern was illustrated in Figure 3.11a, which showed outstanding flexibility and stability. As shown in Figure 3.11 b, after 50 cycles of bending test with a 3.2 nm of minimum bending diameter of curvature, the relative resistive increase was within 10%, which was comparable with the other structure configuration we discussed before. With this patterned ITO-PET substrate, PbS QD solar cells with flat layered architecture was prepared. The architecture configuration and fabrication process for other layers were the same as we did before (which discussed in chapter 2)

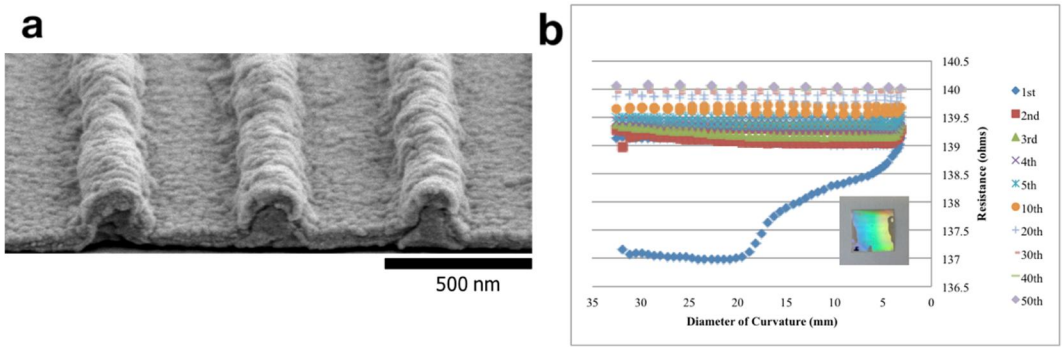

Figure 3.11 (a) SEM cross-section image of the optimized ITO pattern (with 560 nm pitch and 230 nm height) (b) Cycling bending test result for the ITO pattern. (the inset is the picture of the patterned ITO-PET film)

The J-V characteristics of the device and the photovoltaic parameters before and after bending with 5 mm of minimum bending diameter of curvature was depicted in Figure 3.12a and Table 3.1, respectively. Although the overall performance of the device was not very promising, compared the parameters before and after bending, only the JSC decreased a bit (which was confirmed by the EQE spectrum in Figure 3.12b), accounting for the efficiency loss. Moreover, after 20 cycles of bending test, the efficiency of the device only showed 5% loss. Both of these indicates that the PbS QDs solar cell based on patterned ITO-PET substrate worked while retained a large degree of flexibility and stability. Also, it's worth mentioning that compared with the "control device" that fabricated on ITO-glass substrate, the performance of the device made on flexible patterned ITO-PET substrate was not scarified.

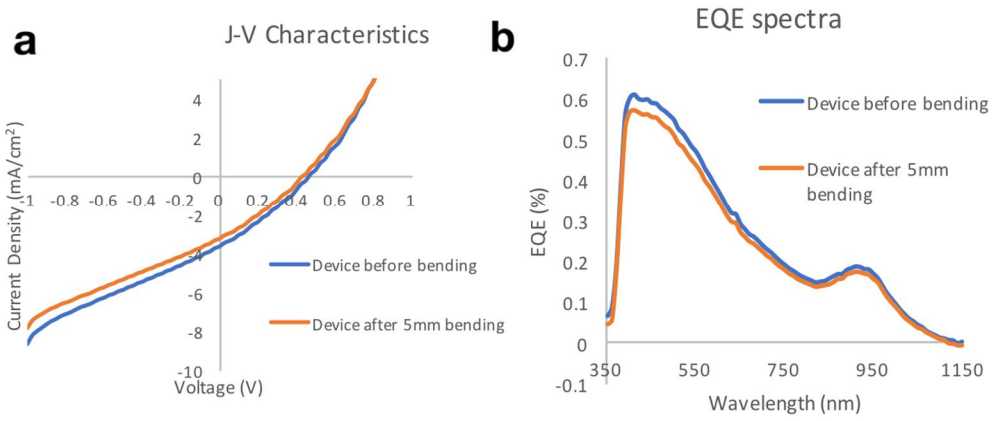

Figure 3.12 (a) J-V characteristics and (b) EQE spectrum of the PbS QD solar cell on patterned ITO-PET substrate.

Table 3.1 1Photovoltaic Parameters of the PbS QD Solar Cells Measured under A.M. 1.5 One sun Illumination.

Devices	V_{OC} (V)	J_{SC} (mA/cm²)	FF (%)	PCE (%)
PbS ITO/glass device (Control)	0.3875	5.566	27.43	0.592
PbS-patterned ITO/PET device	0.4625	5.320	27.87	0.686
PbS-patterned ITO/PET device (after bending)	0.4375	4.083	28.72	0.513

3.8. Conclusion

In this chapter, we fabricated submicron 1D and 2D periodic grating patterns in ITO via a well-controlled laser interference lithography and sputtering deposition at room temperature. The optically transparent films retained requisite commercial level resistivity and sheet resistances in samples subjected to tight curvature bending down to 3.2 mm. Our observed properties surpass all the electrical resistance and resistivities previously reported for ITO formulations created to reach a high flexibility goal. Moreover, by controlling the periodicity of the ITO grating patterns, super-flexible ITO film also exhibited significant light transmittance improvements. The success of a 2D hexagonal ITO nanopattern enabled multiaxial bending while maintained low resistance and high optical transparency. By employing both mechanical and optical simulations, the origin of the enhanced flexibility and transparency was revealed suggesting a route to the ultimate 2D pattern with perfect performance in all the metrics of interests when subjected to multiaxial

bending. These results clearly demonstrate a promising future for ITO in super-flexible devices. The near perfect results of the 1D 285 nm grating pitch shows that improvements in 2D pattern requires a true generalization of the 1D effect. Admittedly, such perfection might come at a cost of complicating the nanopattern and nanofabrication. As the performance is simply geometry dependent, the graduation of the structural dimensions could tailor the optical and electrical performance depending on the application. For example, although not our initial intent, a controlled and known rate of resistance increase on bending cycle, could give rise to other applications such as a bending counter to evaluate fatigue in a connected structural element, e.g., in aircraft structures. Uses of the patterned contacts could also bring additional design advantages for light extraction in light emitting diodes or light trapping in solar cells. [41] Given the techniques employed here are all available for large areas and relatively high-speed manufacturing, the potential for incorporating simple nanostructures in ITO and other transparent conductive oxides seems to be without inherent physical limitations. Notwithstanding these physical facts, the cost and viability at a commercial scale will depend on the cost of nanopatterning. In this work, we employed LIL, but newer approaches[42] such as nanoimprint or self-assembly might have a cost advantages in nanofabrication in a roll-to-roll production.

REFERENCES

(1) Betz, U.; Kharrazi Olsson, M.; Marthy,J.; Escolá, M. F.; Atamny, F. Thin Films Engineering of Indium Tin Oxide: Large Area Flat Panel Displays Application. *Surf. Coatings Technol.* **2006**, 200, 5751-5759.

(2) Park, S. K.; Han, J. I.; Kim, W. K.; Kwak, M. G. Deposition of Indium–tin-oxide Films on Polymer Substrates for Application in Plastic-based Flat Panel Displays. *Thin Solid Films* **2001**, 397, 49-55.

(3) Kim, H.; Gilmore, H.; Piqué, A.; Horwitz, J. S.; Mattoussi, J. S.; Murata, H.; Kafafi, Z. H.;Chrisey, D. B. Electrical, Optical, and Structural Properties of Indium–tin–oxide Thin Films for Organic Light-emitting Devices. *J. Appl. Phys.* **1999**, 86, 6451-6461.

(4) Kim, H.; Horwitz, J. S.; Kushto, G. P.; Kafafi, Z. H.; Chrisey, D. B. Indium Tin Oxide Thin Films Grown on Flexible Plastic Substrates by Pulsed-laser Deposition for Organic Light-emitting Diodes. *Appl. Phys. Lett.* **2001**, 79, 284-286.

(5) Schmidt, H.; Flügge, H.; Winkler, T.; Bülow, T.; Riedl, T.; Kowalsky, W. Efficient Semitransparent Inverted Organic Solar Cells with Indium Tin Oxide Top Electrode. *Appl. Phys. Lett.* **2009**, *94*, 52-54.

(6) Wang, Y.; Deng, J.; Di, J. J.; Tu, Y. Electrodeposition of Large Size Gold Nanoparticles on Indium Tin Oxide Glass and Application as Refractive Index Sensor. *Electrochem. commun.* **2009**, 11, 1034-1037.

(7) Wei, T. C.; Wan, C. C.; Wang, Y.Y.; Chen, C. M.; Shiu, H. S. Immobilization of Poly(N-vinyl-2-pyrrolidone)-Capped Platinum Nanoclusters on Indium−Tin Oxide Glass and Its Application in Dye-Sensitized Solar Cells. *J. Phys. Chem. C*. **2007**, 111, 4847-4853.

(8) Wu, H.; Hu, L.; Carney, T.; Ruan, Z.; Kong, D.; Yu, Z.; Yao, Y.; Cha, J. J.; Zhu, J.; Fan, S. Cui, Y. Low Reflectivity and High Flexibility of Tin-Doped Indium Oxide Nanofiber Transparent Electrodes. *J. Am. Chem. Soc.* **2011**, 133, 27-29.

(9) Yin, L. T.; Chou, J. C.; Chung, W. Y.; Sun, T. P.; Hsiung, S. K. Separate Structure Extended Gate H^+-ion Sensitive Field Effect Transistor on a Glass Substrate. *Sensors Actuators, B Chem.* **2000**, 71, 106-111.

(10) So, S.; Choi, W.; Cheng, C.; Leung, L.M.; Kwong, C. F. F. Surface Preparation and Characterization of Indium Tin Oxide Substrates for Organic Electroluminescent Devices. *Appl. Phys. A Mater. Sci. Process.* **1999**, 68, 447-450.

(11) Nomura, K.; Ohta, H.; Ueda, K.; Kamiya, T.; Hirano, M.; Hosono, H. Thin-Film Transistor Fabricated in Single-Crystalline Transparent Oxide Semiconductor. *Science.* **2003**, 300, 1269-1272.

(12) Hecht, D. S.; Hu, L.; Irvin, G. Emerging Transparent Electrodes Based on Thin Films of Carbon Nanotubes, Graphene, and Metallic Nanostructures. *Adv. Mater.* **2011**, 23, 1482-1513.

(13) Lu, H. T.; Yokoyama, M. Plasma Preparation on Indium-tin-oxide Anode Surface for Organic Light Emitting Diodes. *J. Cryst. Growth.* **2004**, 260, 186-190.

(14) Hu, L.; Hecht, D. S.; Grüner, G. *Chem.* Carbon Nanotube Thin Films: Fabrication, Properties, and Applications. *Rev.* **2010**, 110, 5790-5844.

(15) Dan, B.; Irvin, G. C.; Pasquali, M. Continuous and Scalable Fabrication of Transparent Conducting Carbon Nanotube Films. *ACS Nano.* **2009**, 3, 835-843.

(16) Qing, C.; Zhu, Z. T.; Lemaitre, M. G.; Xia, M. G.; Shim, M.; Rogers, J. A. Transparent Flexible Organic Thin-film Transistors That Use Printed Single-walled Carbon Nanotube Electrodes. *Appl. Phys. Lett.* **2006**, 88, 113511.

(17) Wu, Z.; Chen, Z.; Du, X.; Logan, J. M.; Sippel, J.; Nikolou, M.; Kamaras, K.; Reynolds, J. R.; Tanner, D. B.; Hebard, A. F.; Rinzler, A. G. Transparent, Conductive Carbon Nanotube Films. *science*, **2004**, 305, 1273-1276.

(18) Hu, L.; Hecht, D. S.; Grüner, G. Percolation in Transparent and Conducting Carbon Nanotube Networks. *Nano Lett.* **2004**, 4, 2513-2517.

(19) Becerril, H. A.; Mao, J.; Liu, Z.; Stoltenberg, R. M.; Bao, Z.; Chen, Y. Evaluation of Solution-Processed Reduced Graphene Oxide Films as Transparent Conductors. *ACS Nano* **2008**, 2, 463-470.

(20) Eda, G.; Lin, Y. Y.; Miller, S.; Chen, C. W.; Su, W. F.; Chhowalla, M. Organic Solar Cells with Solution-Processed Graphene Transparent Electrodes. *Appl. Phys. Lett.* **2008**, 92, 263302.

(21) Wang, X.; Zhi, L.; Müllen, K. Transparent, Conductive Graphene Electrodes for Dye-Sensitized Solar Cells. *Nano Lett.* **2008**, 8, 323-327.

(22) Kuang, P.; Park, J. M.; Leung, W.; Mahadevapuram, R. C.; Nalwa, K. S.; Kim, T. G.; Chaudhary, S.; Ho, K. M.; Constant, K. A New Architecture for Transparent Electrodes: Relieving the Trade-Off Between Electrical Conductivity and Optical Transmittance. *Adv. Mater.* **2011**, 23, 2469-2473.

(23) De, S.; Higgins, T. M.; Lyons, P. E.; Doherty, E. M.; Nirmalraj, P. N.; Blau, W. J.; Boland, J. J.; Coleman, J. N. Silver Nanowire Networks as Flexible, Transparent, Conducting Films: Extremely High DC to Optical Conductivity Ratios. *ACS nano*. **2009**, 3, 1767-1774.

(24) Lee, J. Y.; Connor, S. T.; Cui, Y.; Peumans, P. Solution-Processed Metal Nanowire Mesh Transparent Electrodes. *Nano Lett.* **2008**, 8, 689-692.

(25) Hu, L.; Kim, H. S.; Lee, J.; Peumans, P.; Cui, Y. Scalable Coating and Properties of Transparent, Flexible, Silver Nanowire Electrodes. *ACS Nano* **2010**, 4, 2955-2963.

(26) Hong, W.; Xu, Y.; Lu, G.; Li, C.; Shi, G. Transparent Graphene/PEDOT–PSS Composite Films as Counter Electrodes of Dye-Sensitized Solar Cells. *Electrochem. commun.* **2008**, 10, 1555-1558.

(27) Tung, V. C.; Allen, M. J.; Yang, Y.; Kaner, R. B. High-throughput solution processing of large-scale graphene. *Nat. Nanotechnol.* **2009**, 4, 25-29.

(28) Tung, V. C.; Chen, L. M.; Allen, M. J.; Wassei, J. K.; Nelson, K.; Kaner, R. B.; Yang, Y. Low-

Temperature Solution Processing of Graphene−Carbon Nanotube Hybrid Materials for High-Performance Transparent Conductors. *Nano Lett.* **2009**, 9, 1949-1955.

(29) Puetz, J.; Al-Dahoudi, N.; Aegerter, M. A. Processing of Transparent Conducting Coatings Made With Redispersible Crystalline Nanoparticles. *Adv. Eng. Mater.* **2004**, 6, 733-737.

(30) Puetz, J.; Aegerter, M. A. Direct Gravure Printing of Indium Tin Oxide Nanoparticle Patterns on Polymer Foils. *Thin Solid Films* **2008**, 516, 4495-4501.

(31) Heusing, S.; de Oliveira, P. W.; Kraker, E.; Haase, A.; Palfinger, C.; Veith, M. Wet Chemical Deposited ITO Coatings on Flexible Substrates for Organic Photodiodes. *Thin Solid Films* **2009**, 518, 1164-1169.

(32) Maksimenko, I.; Wellmann, P. Low Temperature Processing of Hybrid Nanoparticulate Indium Tin Oxide (ITO) Polymer Layers and Application in Large Scale Lighting Devices. *Thin Solid Films* **2011**, 519, 5744-5747.

(33) Yun, J.; Park, Y. H.; Bae, T. S.; Lee, S.; Lee, G. H. Fabrication of a Completely Transparent and Highly Flexible ITO Nanoparticle Electrode at Room Temperature. *ACS Appl. Mater. Interfaces.* **2013**, 5, 164-172.

(34) Alford, T. L.; Feldman, L. C.; Mayer, J. W. *Fundamentals of Nanoscale Film Analysis*. Springer, **2007**, 336.

(35) Xie, Q.; Hong, M. H.; Tan, H. L.; Chen, G. X.; Shi, L. P.; Chong, T. C. Fabrication of Nanostructures with Laser Interference Lithography. *J. Alloys Compd.* **2008**, 449, 261-264.

(36) Hinsberg, W.; Houle, F.A.; Hoffnagle, J.; Sanchez, M.; Wallraff, G.; Morri-son, M. Deep-Ultraviolet Interferometric Lithography as a Tool for Assessment of Chemically Amplified Photoresist Performance. *J. Vac. Sci. Technol. B.* **1998**, 16, 3689-3694.

(37) Wilson, S. J.; Hutley, M. C. The Optical Properties of 'Moth Eye' Antireflection Surfaces. *Journal of Modern Optics*. **1982**, 29, 993-1009.

(38) Sun, C. H.; Jiang, P.; Jiang, B. Broadband Moth-Eye Antireflection Coatings on Silicon. *Appl. Phys. Lett.* **2008**, 92, 061112.

(39) Boden, S. A.; Bagnall, D. M. Optimization of Moth-Eye Antireflection Schemes for Silicon Solar Cells. *Prog. Photovoltaics*. **2010**, 18, 195-203.

(40) Tikhodeev, S.G.; Yablonskii, A. L.; Muljarov, E. A.; Gippius, N. A.; Ishihara, T. Quasiguided Modes and Optical Properties of Photonic Crystal Slabs. *Phys. Rev. B*, **2002**, 66, 1-17.

(41) Fu, Y.; Dinku, A.G.; Hara, Y.; Miller, C.W.; Vrouwenvelder, K. T.; Lopez, R. Modeling Photovoltaic Performance in Periodic Patterned Colloidal Quantum Dot Solar Cells. *Opt. Express*, **2015**, 23, 779-790.

(42) del Campo, A; Arzt, E. *Generating Micro- and Nanopatterns on Polymeric Materials* Wiley-VCH Verlag GmbH & Co., **2011**, 369.

Chapter 4 : The Impact of Background Oxygen Pressure on the Pulsed Laser Deposition of ZnO Nanolayers and on Their Corresponding Performance as Electron Acceptors in PbS Quantum Dot Solar Cells[1]

4.1 Introduction

As previous discussed in Chapter 1 and 2, the extensive attention of PbS CQDs by researchers originates not only from their unique properties such as tunable bandgap via particle size modification [1-3] and convenient energy level adjustment via molecular linkers,[4, 5] but also from their practical device fabrication advantages, such as the ease of operation of solution-based processing at low temperature and low cost. Specific to its application for solar cell, the significant developments in PbS CQD solar cells are main realized through two routes: surface passivation and device architecture engineering. Additionally, the PbS CQDs solar cells with different architectures have been reported with outstanding air stability.[6, 7-9]

Considering the methods of device architecture engineering, besides introducing new geometric features to the conventional planar structure as we discussed in chapter 2, alternatively, we could adjust the film morphology in order to optimize the interface condition between layers to improve the device performance. Among the numerous studies of the depleted-heterojunction CQDs solar cell performance improvements, the majority of researchers have devoted their attention to the optimization of the absorbing layer. The exploration of window layer materials is rather limited even though they play a crucial role in the extraction and transportation of the charge carriers. People already demonstrate that ZnO is an excellent candidate as electron transport layer since it possesses relatively high mobility, high optical transparency (wide bandgap), abundance, and ease of fabrication and processing.[10, 11] The excellent photosensitive response of ZnO to ultraviolet radiation is also well known and adds to its utility in solar cells.[12] Several

[1]This chapter previously appeared as an article in the Journal of ACS Applied Nanomaterials. The original citation is as follows: Dong, Q., Liu, H., Hara, Y., Star, H.E., Dempsey, J.E., Lopez, R. *ACS Appl. Nano Mater*. **2019**, *2* (2), 767–777

groups have explored various modifications to ZnO films and monitored the effect of these modifications in solar cells to achieve > 8% of PCE.[6, 8, 13, 14] Song and Cheng's group for instance studied the impact of different ZnO thicknesses on the optimization for CQDs solar cell performance.[15] Until a few years ago, nanowires of ZnO, which deviated from common flat architectures, were considered an enabler architecture that eased the transport of electrons out of the CQD layer. For example, Bawendi and Gradečak et al.[16, 17] fabricated ZnO nanowire arrays to improve the solar cell device performance with large photocurrents. Nevertheless, the most efficient ZnO CQDs solar cells reported have employed flat films, but the impact of the ZnO film microstructure on the optimization for CQDs solar cell performance still requires further investigation because some morphological variations, optimized by just final device performance, are not particularly well understood.

To investigate the effect of different ZnO film morphologies, covering not just microstructure but composition and defects, a suitable fabrication method must be considered. Due to its simplicity and large area applicability, sol-gel is more common to deposit ZnO to study the CQDs photovoltaic devices.[18-20] However, sol-gel approaches typically only allow easy adjustments of the film thickness, making addition film morphology control a challenge. Therefore, it is imperative to find an alternative way to make this morphology control be practicable. PLD is a method for ZnO film fabrication by which researchers have reported, one can tailor subtle changes in the film surface morphology and properties via its deposition background gas pressure. [21, 22] Inspired by this, in this chapter we employ PLD with various oxygen gas pressures to obtain ZnO films with different microstructures and examine the performances of the corresponding ZnO-PbS-CQDs photovoltaic devices. Although oxygen pressure increases during PLD fabrication produced monotonic trends in grain size, crystallinity, and electron mobility, once these ZnO layers were incorporated in PbS CQD solar cells, the photovoltaics showed a peak in performance at the mid-pressure fabrication setting. Investigation of the underlying physical mechanism showed that such mid-pressure enhancement arises from a reduction in bi-molecular recombination, which we trace to an enhancement in carrier lifetime and minimum in ZnO oxygen defect densities. Our experimental data

demonstrates detailed information on how to obtain an optimal morphology for the ZnO film to improve the device performance and reveals simple crystallinity or grain enhancement is insufficient. Moreover, our work provides clear guidance on the minimal quality and morphology the electron transport layer must possess for the successful fabrication of heterojunction oxide-PbS CQD-based solar cells.

4.2 Experiments

4.2.1 Synthesis of PbS QDs

PbS quantum dots were synthesized following the method discussed in chapter 2 exactly.

4.2.2 Synthesis of ZnO Film

The ZnO film was prepared by PLD. ITO coated glass was ultrasonically washed successively in a detergent, DI water, acetone, and isopropanol and then dried under air. ZnO films were then deposited on clean ITO glass by PLD (PVD Products Nano-PLD-1000 Pulsed Laser Deposition System, configured with a 248-nm KrF excimer laser) at room temperature from a ZnO target (Kurt J. Lesker 99.9% purity). The Oxygen gas pressure was set to be 80, 100, or 150 mTorr and the flow rate was set to be 5 sccm. The chamber was pumped down to 10^{-6} Torr before flowing the oxygen and starting the ZnO deposition. For the ZnO films deposition, a pulse energy of 200 mJ and a repetition rate of 40 Hz was used. All ZnO films were then annealed in the air for 30 minutes at 350 °C.

4.2.3 Fabrication of PbS CQD Solar Cells

PbS CQDs films were fabricated on top of the ZnO films with different morphology through solid-state ligand exchange via layer-by-layer (LBL) dip-coating technique, and the whole process was conducted in the air. Each cell is composed of 35 layers of TBAI-coated PbS CQDs and 5 layers of EDT-coated PbS CQDs. For the preparation of one layer of TBAI -coated PbS, substrates were dipped in four different solutions successively: (1) TBAI (10 mg/mL in methanol) solution is used as a linker solution, (2) 7.5 mg/mL PbS CQDs solution in hexane, (3) TBAI (10 mg/mL in methanol) solution is used as an exchange

solution, and (4) methanol is used as a rinsing solution. For each solution, the substrates were immersed in for 5s, 20s, 15s, 5s and withdrawn at a speed of 1 mm/s, 10 mm/s, 10 mm/s, 10 mm/s followed by a drying time of 60s, 80s, 30s, 60s, respectively. The same dip-coating process parameters and sequences were applied for the subsequent preparation of layers of EDT-coated PbS films with EDT solution (0.02% vol in acetonitrile). 100 nm of Au was used as photo-cathode and it was deposited in a thermal evaporator under 10^{-6} mbar.

4.3 Characterization of ZnO film with Different Morphology

Considering the architecture of the solar cells, the most obvious role the ZnO-based entry window should play is to provide an n-type electrical layer with minimal impedance for the light transmittance into the absorbing layer. The UV-Vis spectra of three types of ZnO films which were deposited under different oxygen gas pressures are shown in Figure 4.1. To make it simple, before further discussion, we designate the ZnO film deposited under 80 mTorr oxygen as type I-ZnO, deposited under 100 mTorr oxygen as type II-ZnO and deposited under 150 mTorr oxygen as type III-ZnO. Notably, all the curves present a clear UV absorption edge around 375 nm wavelength, and a large transmission (80%-90%) from the blue to near IR wavelength region. However, the curves are not identical, and we can see that the high transmission region presents a modulation typical of interference effects across the oxide layer. Ellipsometry measurements show that the ZnO index of refraction decreases slightly under increased oxygen pressure. The refractive indices for the 80, 100 and 150 mTorr films are 1.89, 1.82, and 1.78, respectively (taking the 500-nm wavelength value as representative of the visible range). This optical change (compared with bulk ZnO index at 500 nm wavelength which is 1.98) may arise from the structural changes in the film. This is confirmed by inspection of scanning electron micrographs (SEM) of the ZnO films prepared at the various oxygen pressures. As indicated in Figure 4.2, an inverse relationship between the oxygen pressure and the grain size of the ZnO film is an obvious effect. Less obvious, but in association with the index of refraction drop, the grains are not only smaller, but also less densely packed. This effect from the PLD deposition has been shown in other instances.[23] The results from atomic force microscopy (AFM) analysis (Figure 4.3)

agree well with the SEM results. They reveal that the RMS roughness in the films increases along with the increase of background gas pressure, forming a progressively less compact microstructure composed of smaller nanocrystallites.

This microstructural change is coupled with structural quality changes on the atomic scale. To explore this connection, we perform the XRD to analyze the crystal structures of the deposited ZnO films, which is shown in Figure 4.4. The XRD patterns of the three types of ZnO films indicate they present the expected wurtzite structure, but as it can be noted the C-axis oriented (002) peak intensity decreased significantly following the oxygen pressure increase, with a concomitant increase of the full width at half maximum (FWHM). Scherrer's [24] relationship between x-ray line sharpness and size of the nanocrystallites confirms the microstructural changes we already noted from the SEM micrographs. The XRD data has a more important implication, specifically that the smaller crystallites are also increasingly incoherently connected (breaking crystal translation symmetry) among each other. Thus, although the film morphologies and their optical properties are quite similar, we could expect the microstructure qualities will have a marked influence in the electron transport properties, namely the carrier transport mobility.

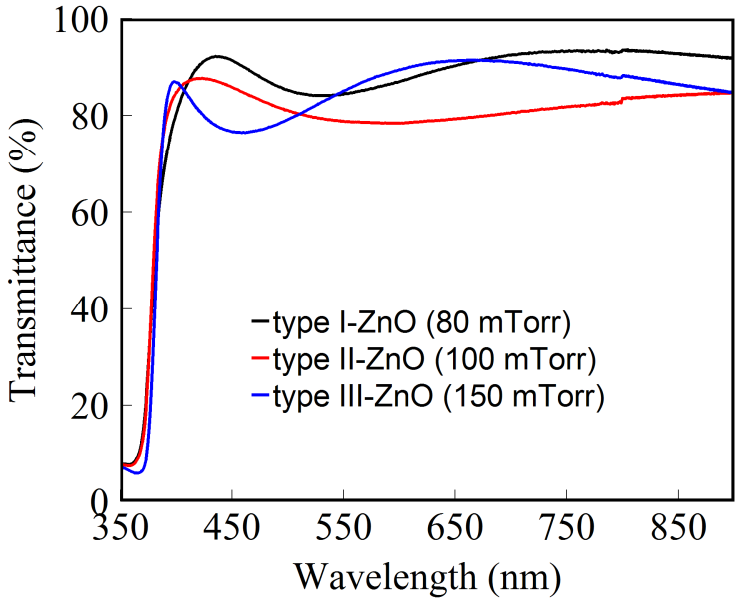

Figure 4.1 Optical transmission spectrum of three different types of ZnO films.

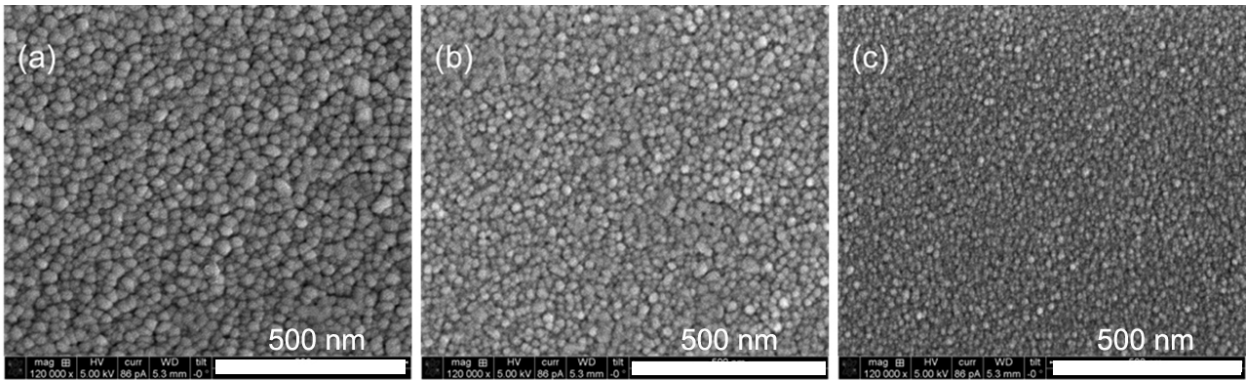

Figure 4.2 SEM images of the deposited ZnO films under different oxygen pressures: (a) 80 mTorr; (b) 100 mTorr; (c) 150 mTorr.

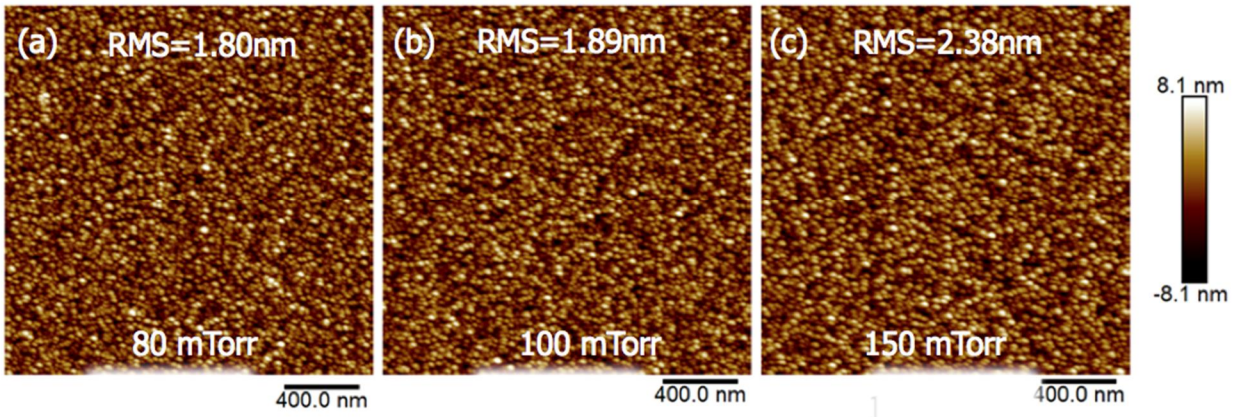

Figure 4.3 AFM images of films surface (scan size 2 μm × 2μm) for various deposited oxygen gas pressures, (a) 80 mTorr, (b) 100 mTorr, (c) 150 mTorr.

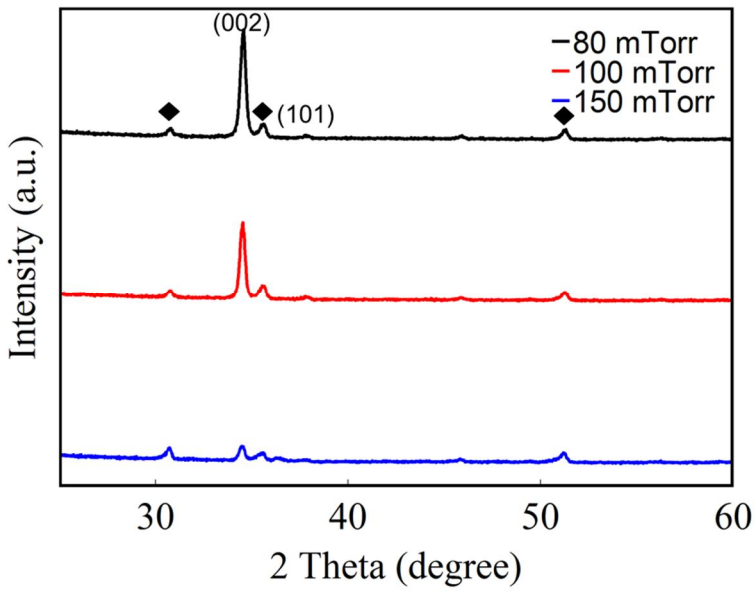

Figure 4.4 XRD patterns of ZnO films on ITO/glass substrate. ITO peaks are marked by black diamonds and ZnO peaks are identified by their Miller indices.

The field-effect transistors (FET) with the ZnO film in the channel are fabricated to study the electrical transport properties of the ZnO films prepared at different pressures.[25] The channel width and length are set to be 0.15 mm and 1.5 mm, respectively. The channel is built on a SiO_2 p-type wafer, with 285 nm oxide, 100 nm aluminum contacts. The detailed electrical parameters obtained from FET measurements are summarized in Table 4.1. We observe that the carrier mobility of the ZnO films decrease while increasing the oxygen gas pressure during deposition. Simultaneously, the correlated carrier concentrations increase. The ZnO film deposited under lower oxygen gas pressure gives a larger carrier mobility owing to the smaller number of grain boundaries in such film,[22] as observed in the SEM images (Figure 4.2). Overall, the trends in the optical transmission, SEM, AFM, XRD and mobility data indicate that the ZnO fabricated with the lowest oxygen pressure has the best morphology and electronic properties. However, as shown below subsequent studies of solar cells fabricated with these films revealed that these trends do not correlate with solar cell performance.

Table 4.1 Deposition oxygen pressure-dependent electrical properties for different ZnO films

Deposition O_2 pressure (mTorr)	Carrier concentration (cm^{-3})	Mobility ($cm^2 v^{-1} s^{-1}$)	Conductivity ($S\ cm^{-1}$)
80	2.9×10^{14}	5.1	1.6×10^{-4}
100	6.5×10^{14}	3.4	5.3×10^{-4}
150	1.5×10^{16}	2.4	5.6×10^{-3}

4.4 Role of Morphology of ZnO film on Photovoltaic Properties

Solar cell devices were fabricated in a layered structure with ZnO/PbS-TBAI/PbS-EDT/ Au on an ITO/glass substrate (schematic in Figure 4.5a). Each particular layer was created as described in detail in the methods section and with thicknesses within 5 % of the ones shown in the representative example in Figure 4.5b. It's worth pointing out that for the three types of ZnO films, the film thickness is 108±1nm, 110±1nm and 113±1nm, respectively. Since the thickness difference is still within 5%, its influence on the devices performance could be ignored and we approximately take the film thickness for all types as the same. The J–V characteristics and EQE spectra of the three types of ZnO–PbS CQDs solar cells are displayed in Figure 4.6a. The typical devices with type I-ZnO exhibited a J_{SC} of 17.3 mA cm^{-2}, a V_{OC} of 0.64 V, and a fill factor (FF) of 48.2%, resulting in a PCE of 5.3%. Fabricated at 100 mTorr of oxygen, the Type II-ZnO devices surprisingly presented a significant PCE enhancement, delivering a local champion device (type II-ZnO) with a PCE of 7.4% and a J_{SC} of 21.1 mA cm^{-2}. However, further increasing the oxygen pressure to 150 mTorr (Type III- ZnO), the PCE of the devices suffers a substantial deterioration. The description of ZnO films and the corresponding devices performance parameters are listed in Table 4.2 in details. Comparing among the different devices, we can see that both the J_{SC} and FF of type II-ZnO are simultaneously improved with very minimal changes in the V_{OC}. This is confirmed by the ultraviolet photoelectron spectroscopy (UPS) measurements on ZnO films

deposited under different oxygen pressures as illustrated in Figure 4.7. Ultraviolet photoelectron spectroscopy measurements were conducted in an ultrahigh vacuum chamber (10-10 mbar) with a He (I) (21.2 eV) discharge lamp. During the measurement, copper tape was used to make electrical contact and a 10.0V bias was used to determine the low-kinetic-energy photoelectron cut-off. With the increase of the oxygen gas pressure, the Fermi level regarding to vacuum did not show an obvious change, indicating a similar V_{OC} can be expected for the devices with different types of ZnO films. In order to guarantee this was not an anecdotical event in the device performance, twenty devices of each type were tested. The statistical deviations from the median values are relatively small (under 7% variation) for all devices, supporting the conclusion that ZnO morphological changes induced by the PLD oxygen pressure are indeed behind this substantial solar cell performance effect. Still though, as highlighted above this solar performance trend does not simply follow the SEM/AFM/XRD structural tendencies nor the electrical parameters derived from the ZnO FETs characterization.

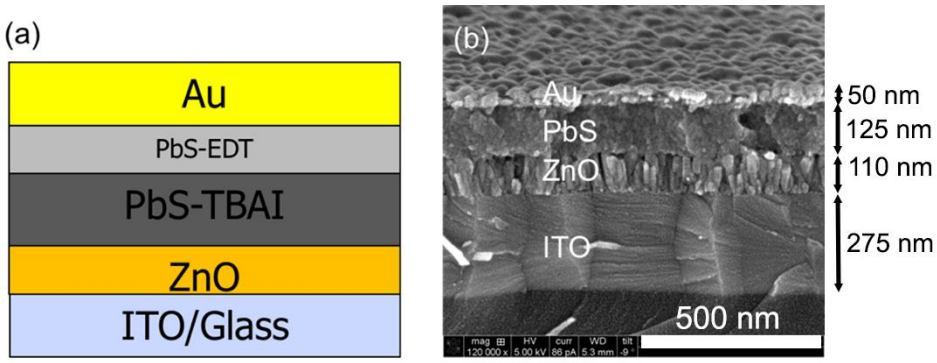

Figure 4.5 (a) Schematic device structure showing the heterojunction between n-type ZnO and p-type PbS CQDs. (b) SEM cross-section image of type-II ZnO-PbS CQDs device indicating layer thicknesses.

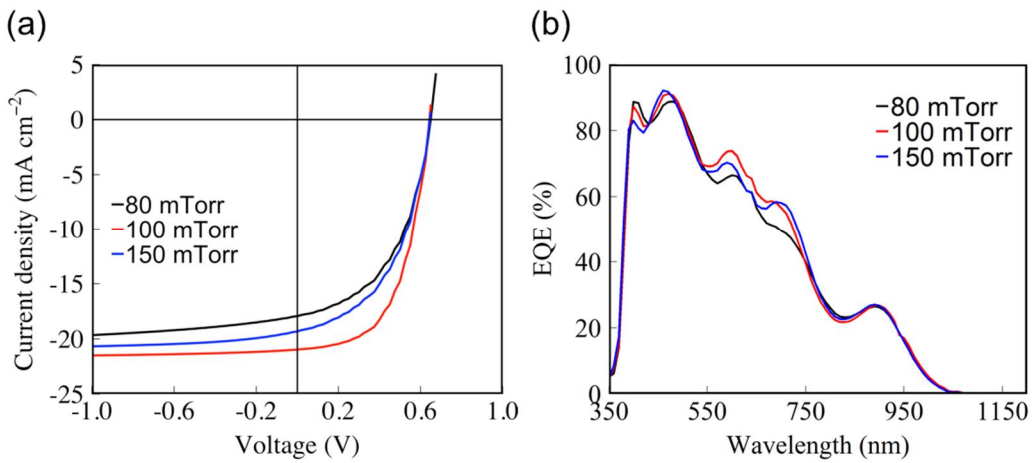

Figure 4.6 (a) Representative J-V characteristics. (b) EQE curve of devices with ZnO films under different deposition oxygen pressure.

Table 4.2 Performance parameters of three types of the devices summarized from Figure 4.6.

Devices	V_{OC} (V)	J_{SC} (mA/cm^2)	FF (%)	PCE (%)
Type-I ZnO-PbS device (80mTorr)	0.64±0.01	17.2±0.7	48.2±0.5	5.3±0.2
Type-II ZnO-PbS device (100mTorr)	0.64±0.01	21.1±0.1	55.6±0.1	7.4±0.3
Type-III ZnO-PbS device (150mTorr)	0.64±0.01	19.3±0.2	48.7±0.1	6.0±0.2

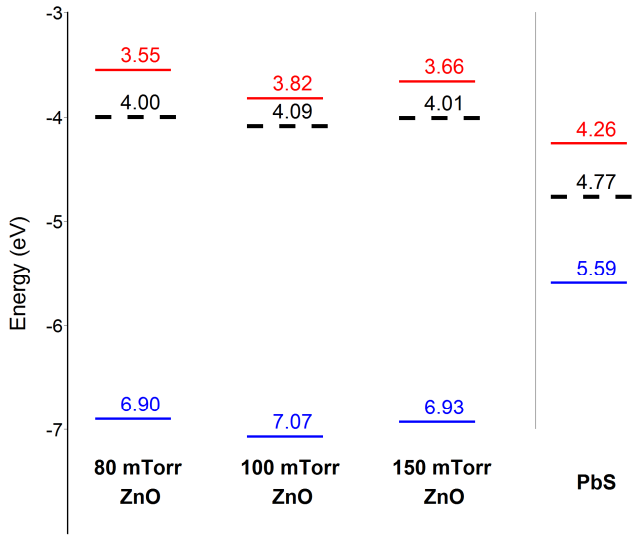

Figure 4.7 Energy levels with respect to vacuum for ZnO film deposited under different oxygen pressures, and PbS-TBAI film. The Fermi levels (E_F, dashed line) and valence band edges (E_V, blue lines) were determined by UPS. The conduction band edges (E_C, red lines) were calculated by adding the optical bandgap energy of 3.25 eV, 3.25 eV and 3.27 eV, respectively as determined from the first exciton absorption peak in the ZnO absorption spectrum to E_V.

To identify the origin of the J_{SC} improvement, we perform the EQE spectra for different types of ZnO film-based PbS CQDs solar cells as shown in Fig. 4.6b. Considering making comprehensive comparisons, the EQE spectra are divided into three distinctive regions. In the ultra-violet region (400–450 nm), the higher EQE value in type I-ZnO devices is consistent with the outcome of transmission spectrum discussed above. This optical difference is not large, but it might explain the slight relative decrease for both type II-ZnO and type III-ZnO based devices. In the visible region (450–700 nm), the EQE of type II-ZnO devices demonstrates higher, broader and more feature rich response, which states that type II-ZnO devices couple to visible wavelengths more effectively and/or could be more efficiently extracting the charge carriers. In the infrared region, the EQE spectra overlap quite well for all three types of devices and it confirms as others have demonstrated the positive role of PbS-TBAI/PbS-EDT back structure to secure the IR-originated carriers' extraction.[6] Based on these observations, it is clear that the higher J_{SC} of Type II-ZnO devices is attributed to the improvement of the external quantum efficiency in the visible region. However, the significant change in the FF indicates this is not a pure optical enhancement arising from a constructive light-interference event originating of the film thickness and index of refraction combination of the whole stack. Indeed, the J-V curve shows that at high reverse bias (−1 V) all the current densities closely converge ~ 20 - 21.5 mA cm^{-2} indicating that the optical differences are not substantial enough to explain the behavior from the short circuit to the forward bias regions.

4.5 Losses Analysis Based on White Light Intensity –dependent Measurement

To identify the fundamental reasons behind the performance differences between different types of devices, the J-V characteristics and EQE spectra under various illumination conditions were performed to explore the charge carriers' recombination process. The charge collection probabilities of the devices under various light intensities are obtained by manipulating the J-V characteristics and from which the predominant recombination mechanism (bi-molecular/mono-molecular recombination) is recognized. As discussed in other literature reports, [26-28] the photocurrent of PbS CQDs-based solar cell with a thickness z of the PbS film could be derived from a simplified model of charge generation/collection:

$$J_{ph}=e\int G(LI)\, P_c\,(LI, V)\, dz \tag{4.1}$$

where G(LI) is the absorbed photon flux per unit volume and P_c (LI, V) is the probability of charge collection (G is a function of the light intensity (LI) and P_c is left to possibly be). [26-29] Alternatively, under a more common situation in which we don't consider the effect of the device geometry, this probability can be presented as:

$$P_c\,(LI, V) = |J_{ph}\,(LI, V)/\,(J_{ph} \text{ at saturation})\,| \tag{4.2}$$

Given the saturated current is set to be at −1 V for all three kinds of devices, we could expand the collection probability as follows:

$$P_c\,(LI, V) = |J_{ph}\,(LI, V)/J_{ph}\,(LI, -1V)\,| \tag{4.3}$$

As shown in Figure 4.8, under different light intensities, the charge collection probabilities derived from the equations discussed above don't overlap exactly at all applied voltage biases for all the three types of devices. This is a qualitative indication of the existence of bi-molecular recombination [26-29] for all three device types, but the curves also indicate its prominence in each device type is significantly distinct. In the type II device, the normalized curves overlap quite well in the reverse bias region and their degrees of dispersion over the positive voltage range are relative smaller. In sharp contrast, for both the type I and type III devices, all the curves start to disperse immediately from the reverse bias region. The curves dispersion for the type I device is the widest, even more than that for the type III device especially in the reverse bias region. Therefore, it demonstrates that bi-molecular recombination appears significantly greater in both the types I and III devices. This is the most likely physical reason accounting for the reduction in FF compared to the type II device.

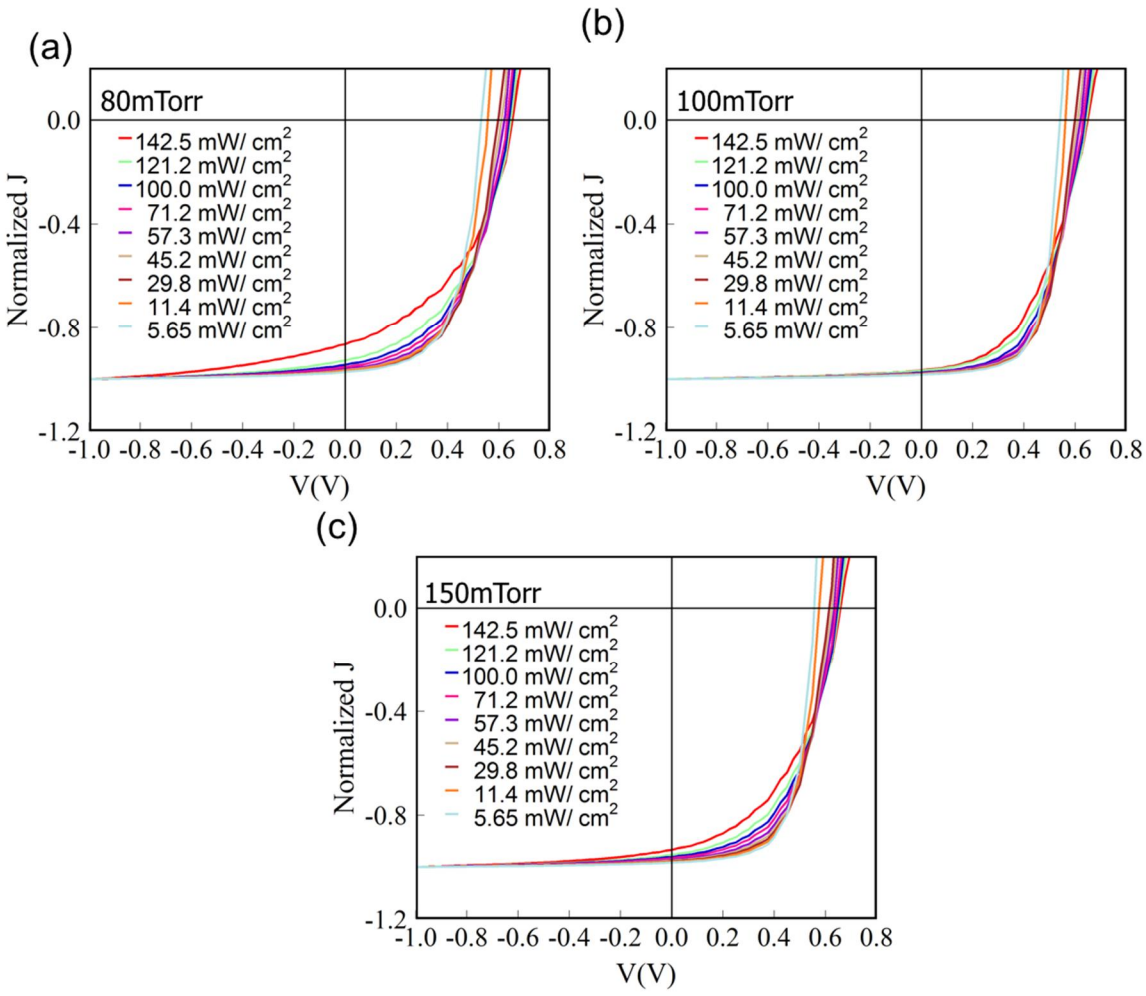

Figure 4.8 Charge collection probabilities of the devices with ZnO films under different deposition oxygen pressures, (a) 80 mTorr; (b) 100 mTorr; (c) 150 mTorr. The charge collection probabilities of all are derived from the normalization of their J-V Characteristics under different light intensities, respectively.

Figure. 4.9 shows the EQE spectra measured while the devices were exposed to different white light intensities (all taken in short circuit conditions). In an ideal case, the EQE dark curve should overlap well with the one under extra white light exposure. In other words, as before, the more acute EQE curve dispersion indicates that more recombination is occurring under illumination. Comparing the three types of devices, the EQE curves of the type II device shows the least dispersity vs. the dark curve through the whole wavelength region.

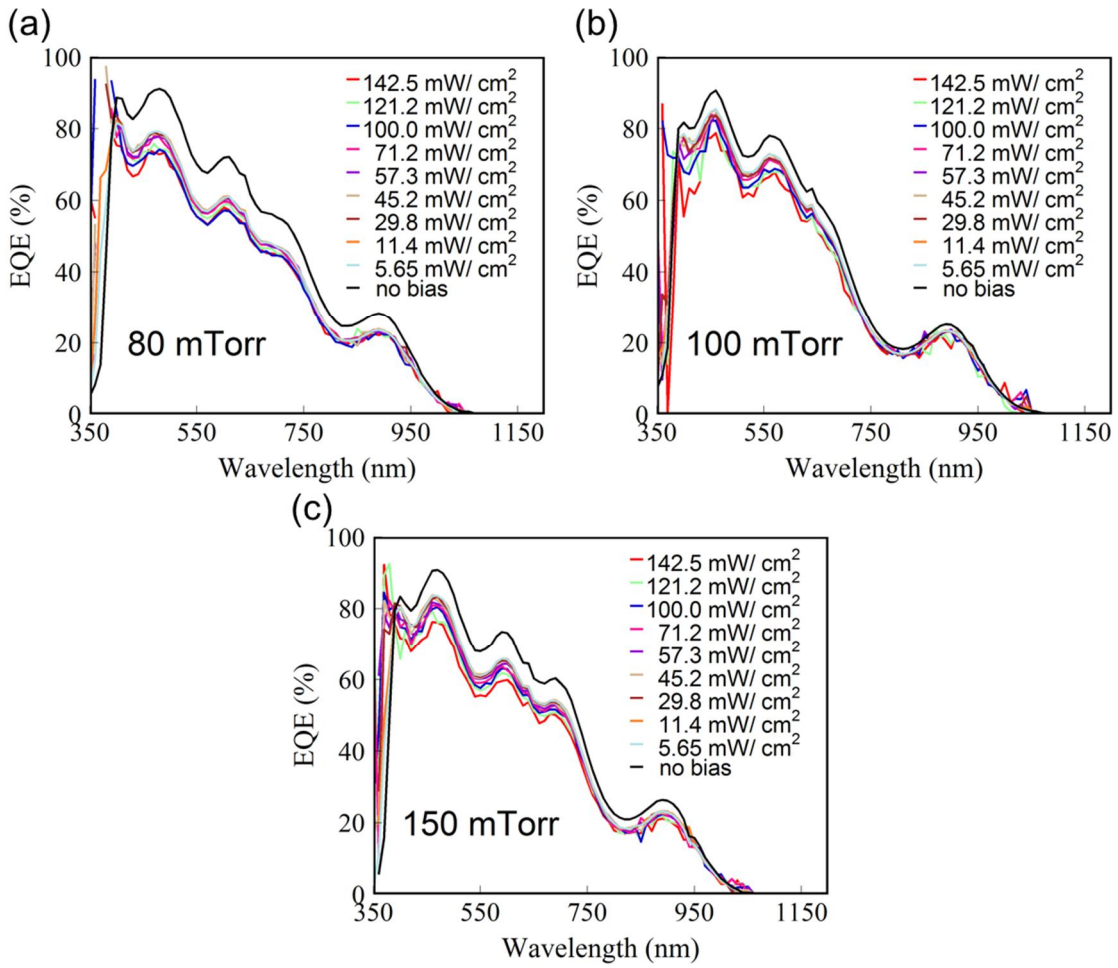

Figure 4.9 White-light bias EQE spectra of the devices with ZnO films under different deposition oxygen pressures, (a) 80 mTorr; (b) 100 mTorr; (c) 150 mTorr.

The above light intensity experiments all confirm that the differences in bi-molecular recombination are the key factor separating the performance between devices. However, how is this type of recombination linked to the ZnO fabrication differences? In order to make headway in this key question, we have directed out attention to quantitatively studying the charge carrier accumulation and transport in the PbS CQDs-based solar cells in the following section.

4.6 Charge Carrier Conduction and Transport Mechanism

Electrochemical Impedance Spectroscopy (EIS) is a very powerful tool for the investigation of the impedance spectra of these devices under different V_{OC} conditions that were extracted from the J-V characteristics induced under different light intensities (Figure 4.10). In these curves, Z, the complex impedance of the device is expressed by the two parts, the real part Z' and the imaginary part Z''. The relationship among those three are shown as follows (eq. 4.4):

$$Z(\omega) = Z' + i Z'' \quad (4.4)$$

The frequency is an indirect parameter in Figure 4.10, and it decrease along the semi arc from left to right under different light intensities.[29, 30] Although the semi arcs look quite similar, quantitatively there are important differences. In the low-frequency region, the recombination resistance is quantified by the value derived from the cross point of the EIS curve and the Z'-axis. [30, 31] In Figure 4.11a we show these recombination resistances vs. the V_{OC} obtained under different light bias conditions. A large recombination resistance (R_{rec}) is a necessary element for a high-performance PbS CQDs-based solar cells since the accumulated charge carriers are allowed to flow through the external circuit under this circumstance .[30, 32] EIS also allowed us to characterize the carrier lifetime of these CQD based solar cells. This is a crucial parameter to describe the charge dynamics of the solar cells. Generally, the primary relaxation process could be expressed by the following equation:[30, 33]

$$I(t) = Ae^{\frac{-t}{\tau_1}} \quad (4.5)$$

where A is a constant, τ_1 is the carriers' lifetime, and *t* is the time. The relaxation process listed above can be associated with a characteristic frequency,[30, 34] which is simple given in the following equation,

$$\omega_1 = 1/\tau_1 \quad (4.6)$$

where the value of the frequency ω_1 can be directly derived from the plot of imaginary part of the impedance Z''as a function of frequency. ω_1 is the frequency that corresponds to the peak value of Z''. In Figure 4.11b,

it is clear that the lifetime of the carriers in type II device is the longest among three types of devices, followed by type III and type I under illumination.

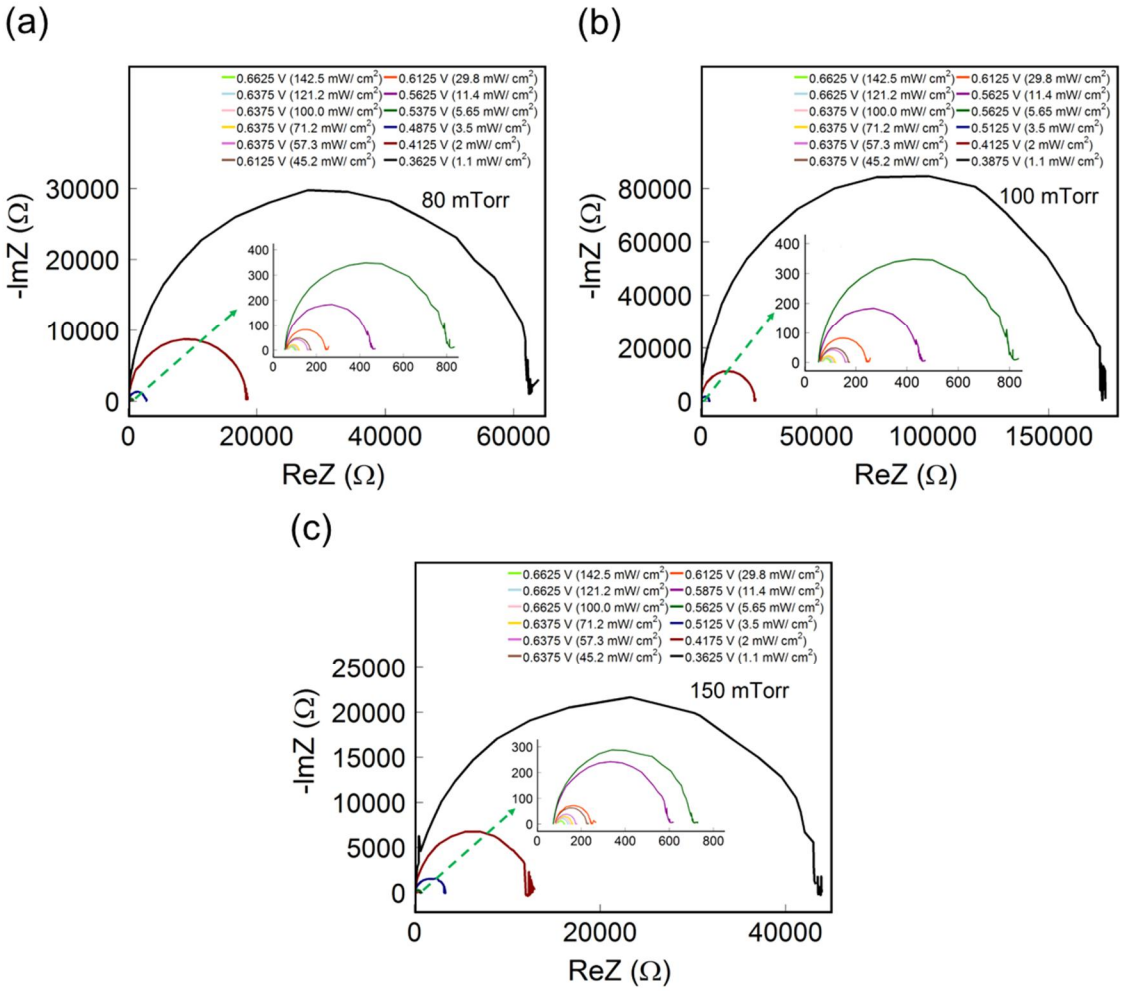

Figure 4.10 Impedance spectra for the devices with ZnO films under different deposition oxygen pressures, (a) 80 mTorr; (b) 100 mTorr; (c) 150 mTorr.

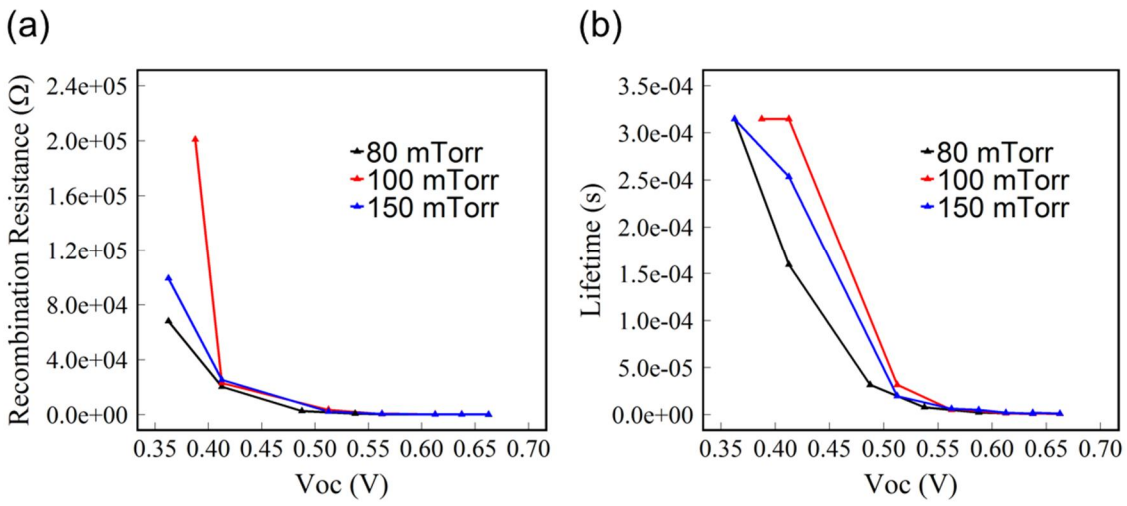

Figure 4.11 (a) Recombination resistance and (b) carrier lifetimes for the devices with ZnO films deposited under different oxygen pressures.

Up to this point, we can partially summarize the findings by stating the differences in solar cell performance are due to different rates of bi-molecular recombination, and this deleterious effect is minimal in type II-ZnO-containing solar cells because its recombination lifetime and resistance are the largest. Since the only difference in these devices is in the ZnO morphology, we should be able to connect the improved device metrics to the ZnO-type II structural/compositional morphological characteristics.

However, given that mobility and the charge lifetime should be positively correlated, why does the FET mobility characterization not anticipate the EIS observations? We believe the most important reason behind this apparent discrepancy is that the FET measures transport qualities in-plane along the film surface, but not across the film-thickness dimension, the way charges move in solar cell operation and are actually probed by EIS. As shown in the SEM micrographs the structure of the films is granular but it is also somewhat columnar (Figure 4.2), thus defects in-plane across those columns are likely to affect the FET measured mobilities, but the defects along the film thickness likely play a larger role in solar cell operation.

To probe on the existence and density of defects in the ZnO layers, we have employed several approaches, the first of which is transient photovoltage spectroscopy.[35, 36] Using this technique, the trap

state densities of the three types of devices have been explored. For an ideal trap-free semiconductor, the photogenerated electrons under illumination experience a very fast relaxation process to the conduction band-edges and still sustain dynamic thermal equilibrium. This situation is applicable for the holes in the valence band. The two quasi-Fermi levels they establish are directly corresponding to the V_{OC} itself. For a semiconductor with traps, upon illumination some of the photogenerated carriers are used to fill the traps and therefore generate a smaller V_{OC}. This process could be revealed with the transient photovoltage spectroscopy. In the photovoltage transient measurement, the modulation of the V_{OC} was realized by a 532-nm high energy nanosecond laser on top of constant light bias with 5 ns of the pulse duration and 15 Hz of the repetition rate. The modulated V_{OC} was well controlled by tuning the intensity of nanosecond laser to make sure that it was less than 10% of V_{OC}. The open circuit voltage transient was recorded with a digital oscilloscope at an input impedance of 1MΩ, while the short circuit transient was measured at an impedance of 50 Ω. Figure 4.12a-c shows the capacitance, carrier concentration (*n),* and density of trap states (DOS) at a series of V_{OC} values. Given the assumption that the exciton generation and applied bias are non-correlated and a small recombination occurs under short circuit conditions, since capacitance corresponds to the stored charge in the bulk of the film, larger capacitance implies more trap states in the film. Here *n* can also be seen as the number of extra carriers used for the separation of the quasi-Fermi levels and the V_{OC} accordingly, (more details on this method can be found in ref 40).[37] As shown in Figure 4.12 in all parameters *n*, capacitance per unit area, and particularly for the DOS, the lowest values are all associated with the type II device, followed by the type III device and the highest in type I. This is consistent with the photovoltaic performance shown earlier. We note that this technique cannot distinguish where the defects are located. As ZnO is the electron acceptor, we presume some defects are at energy states below the conduction band in the ZnO, but some may also exist within the PbS layer. However, as noted earlier, extreme care was taken to ensure uniformity in the PbS layer across samples so that most differences can be attributed to the ZnO itself.

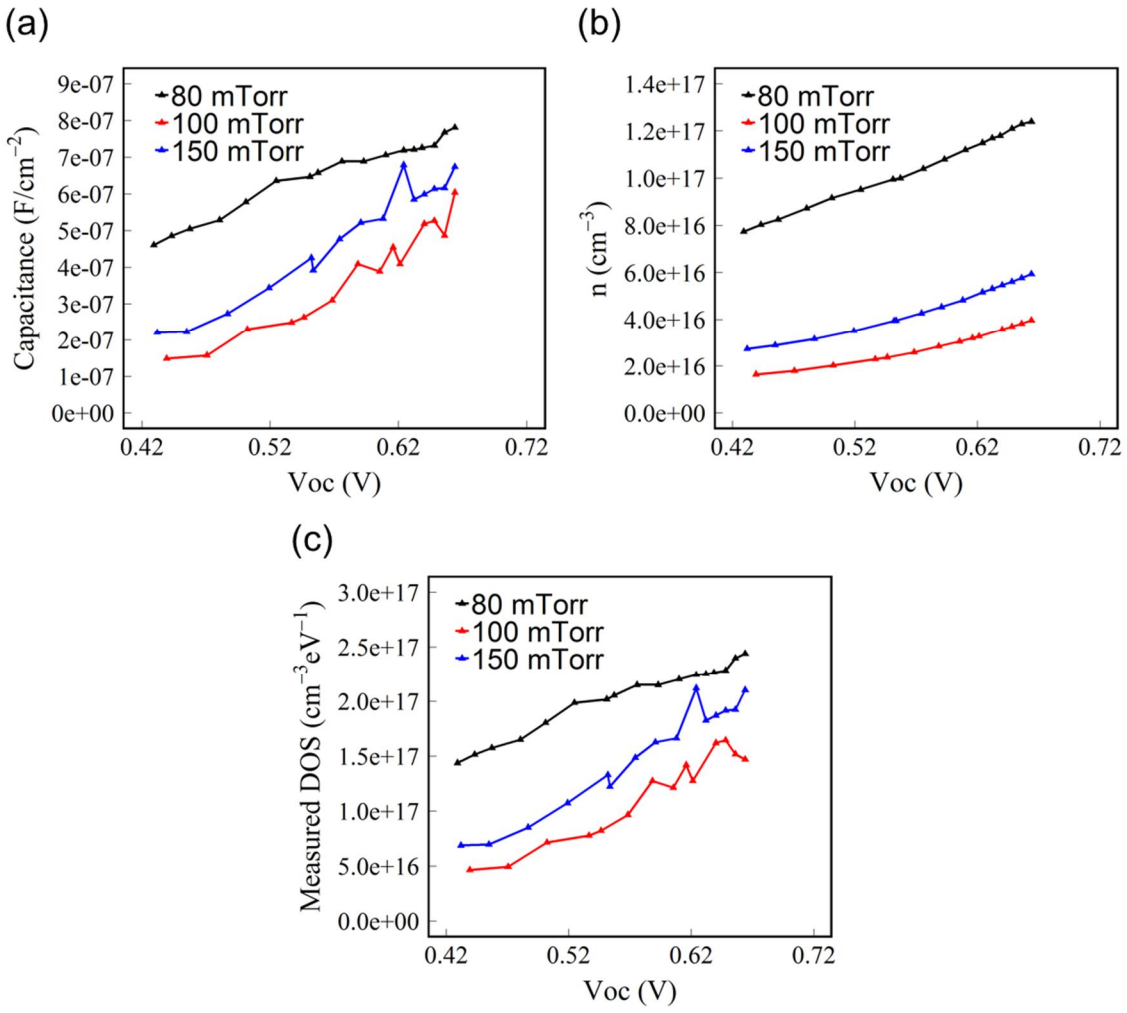

Figure 4.12 Capacitance (a), carrier concentration (b) and density of trap states (c) for the devices with ZnO films deposited under different oxygen pressures.

Based on aforementioned results and discussion, the performance improvement with optimized ZnO film morphology can now be thoroughly explained. Despite showing a better planar mobility, presumably due to its in-plane compactness, the ZnO-type I has a higher overall density of defects. The best cell performance obtained from ZnO-type II arises because it presents the lowest defect DOS, the largest carrier lifetime, and thus a reduced bimolecular recombination.

4.7 Impact of Physical Defects on ZnO Films Performance

Finally, what physical defects have caused by the ZnO performance disparity? Photoluminescence (PL) and X-ray photoelectron spectroscopy (XPS) were employed to bring light to this last question. Figure 4.13 show the PL spectra and XPS for the three different types of ZnO films. As illustrated in the PL spectra (Figure 4.13a), the two emission peaks indicate different kinds of emissions. The band-edge emission is indicated by the peak centered near 400 nm and the oxygen vacancy (V_O) defect related emission in turn is indicated by the other broad one centered at 660 nm.[38–40] Compared with the three types of ZnO films, the type I-ZnO has the highest peak related to the V_O defect, which is likely the ultimate culprit behind its lower performance in the solar cells. This is also the most likely reason for the device's slight EQE losses within the 500-800 nm wavelength region in absorption/emission. On the other hand, XPS analysis provides details on the state of the surface oxygen ions in the ZnO. As shown in Figure 4.13b, c and d, the deconvoluted oxygen binding peak for ZnO could be expressed by two contributing signals: the lower-binding-energy peak (529.2 eV) corresponds to the oxygen atoms in a ZnO matrix, and the higher-binding-energy peak (531.5 eV) corresponds to the oxygen-interstitial defects.[41] The numbers shown within the figure are the ratios of the areas of the lower-binding-energy peak to that of the higher-binding-energy peak, which indicate the relative content of the oxygen-defected binding sites in the ZnO film. The data in Figure 4.13b and c shows relative smaller intensities of higher-binding-energy components, indicating that the oxygen-interstitial binding defects in the ZnO films are lower at the two lower oxygen fabrication pressures. These XPS and PL results indicate that the decline of vacancies and the rise of oxygen interstitials along the oxygen pressure increase path, introduce different traps and hindering mechanisms to the charge transport in the solar cell. The best morphology of the ZnO film thus seems to result from a balancing act between these compositional layer defects.

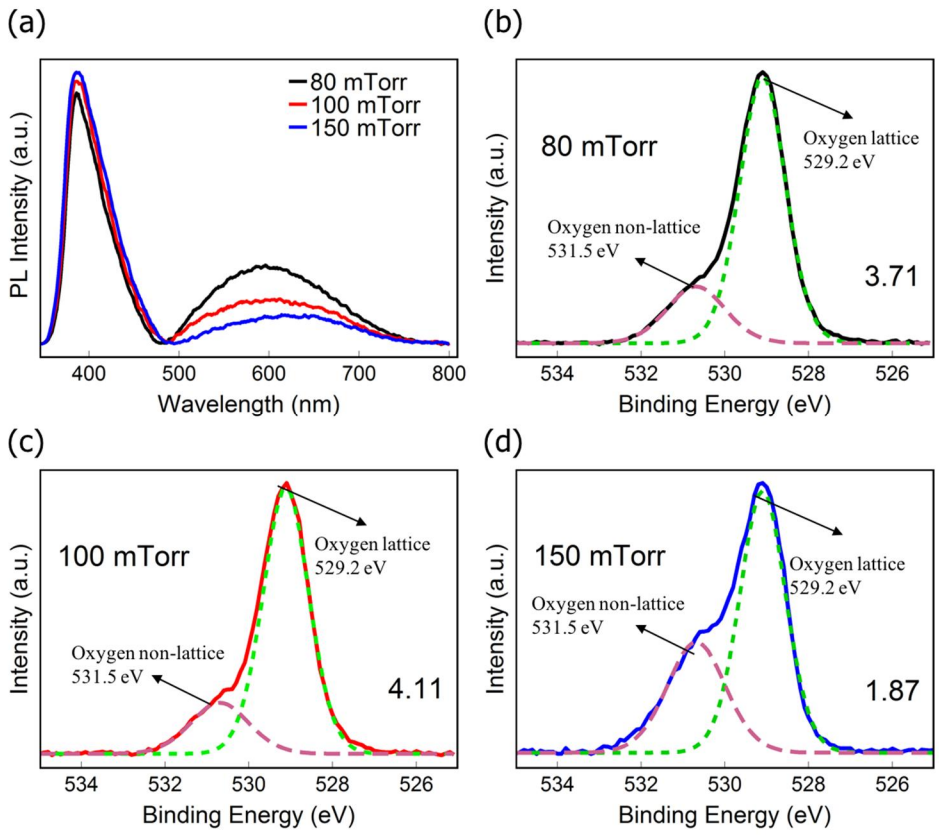

Figure 4.13 (a) Steady-state PL spectra of ZnO films with different morphology. Deconvoluted XPS spectra of the O1s core level of ZnO films under different deposition oxygen pressures, (b) 80 mTorr; (c) 100 mTorr; (d) 150 mTorr. The numbers shown within the figure are the ratios of the areas of the lower-binding-energy peak to that of the higher-binding-energy peak, which indicate the relative content of the oxygen-defected binding sites in the ZnO film.

4.8 Conclusion

In this chapter, we discuss the impact of ZnO film morphology on the performance of ZnO-PbS CQD solar cell device and the charge carrier conduction and transport mechanism underneath. During the fabrication of three types of ZnO films by PLD, which differed only in the oxygen pressures employed during growth, we encountered very distinct differences that had a remarkable impact in their performance as part of PbS CQDs solar cells. Oxygen pressure increases led to small grain sizes, less crystallographic alignment, lower film density, and decreased index of refraction, which in turn resulted in a decreasing in-plane electron mobility. Notwithstanding this monotonic trend, the mid fabrication pressure, 100 mTorr, actually resulted in the higher PCE performance of 7.8%, due to significantly enhanced J_{SC} and FF relative

to the devices with ZnO made at the highest and lowest fabrication pressures. Light and voltage bias analyses showed that the bulk of this improvement originated from limited bimolecular recombination, which was likely a consequence of an extended carrier-lifetime and a relatively low defect density. The defects are not limited to one defect type, rather there are the luminescent defects associated with oxygen vacancies declining with oxygen fabrication pressure, and other types associated with interstitial/amorphous ZnO. These results highlight the clear morphology changes that a single processing variable can induce to modify the micro- and atomic structure of the material and thereby lead to drastic opto-electronic property changes. Direct measurement of material defect types and densities might be no less important than more immediate characterizations such as crystallinity, grain size, or even in-plane mobility. Further work is now directed towards determining whether the ZnO oxygen defects are a bulk-transport hindering factor or only possibly acting at the interface with the PbS quantum dot film.

REFERENCES

(1) Cunningham, P. D.; Boercker, J. E.; Foos, E. E.; Lumb, M. P.; Smith, A. R.; Tischler, J. G.; Melinger, J. S. Enhanced Multiple Exciton Generation in Quasi-One-Dimensional Semiconductors. *Nano Lett.* **2011**, *11*, 3476–3481.

(2) Semonin, O. E.; Luther, J. M.; Choi, S.; Chen, H.; Gao, J.; Nozik, A. J.; Beard, M. C. Peak External Photocurrent Quantum Efficiency Exceeding 100% via MEG In a Quantum Dot Solar Cell. **2011**, *334* , 1530–1534.

(3) Gao, J.; Luther, J. M.; Semonin, O. E.; Ellingson, R. J.; Nozik, A. J.; Beard, M. C. Quantum Dot Size Dependent J - V Characteristics in Heterojunction ZnO/PbS Quantum Dot Solar Cells. *Nano Lett.* **2011**, *11*, 1002–1008.

(4) Brown, P. R.; Kim, D.; Lunt, R. R.; Zhao, N.; Bawendi, M. G.; Grossman, J. C.; Bulović, V. Energy Level Modification in Lead Sulfide Quantum Dot Thin Films through Ligand Exchange. *ACS Nano* **2014**, *8*, 5863–5872.

(5) Lan, X.; Masala, S.; Sargent, E. H. Charge-Extraction Strategies for Colloidal Quantum Dot Photovoltaics. *Nat. Mater.* **2014**, *13*, 233–240.

(6) Xu, J.; Voznyy, O.; Liu, M.; Kirmani, A. R.; Walters, G.; Munir, R.; Abdelsamie, M.; Proppe, A. H.; Sarkar, A.; García De Arquer, F. P.; Wei, M.; Sun, B.; Liu, M.; Ouellette, O.; Quintero-Bermudez, R.; L, J.; Fan, J.; Quan, L.; Todorivic, P.; Tan, H.; Hoogland, S.; Kelley, S. O.; Stefik, M.; Amassian, A.; Sargent, E. H.2D Matrix Engineering for Homogeneous Quantum Dot Coupling in Photovoltaic Solids. *Nat. Nanotechnol*. **2018**, *13*, 456–462.

(7) Shi, G.; Wang, Y.; Liu, Z.; Han, L.; Liu, J.; Wang, Y.; Lu, K.; Chen, S.; Ling, X.; Li, Y.; Cheng, S.; Ma, W. Stable and Highly Efficient PbS Quantum Dot Tandem Solar Cells Employing a Rationally Designed Recombination Layer. *Adv. Energy Mater.* **2017**, *7*, 1–8.

(8) Lan, X.; Voznyy, O.; Kiani, A.; García De Arquer, F. P.; Abbas, A. S.; Kim, G. H.; Liu, M.; Yang, Z.; Walters, G.; Xu, J.; Yuan, M.; Ning, Z.; Fan, F.; Kanjanaboos, P.;Kramer, I.; Zhitomirsky, D.; Lee, P.; Perelgut, A.; Hoogland, S.; Sargent, E. H. Passivation Using Molecular Halides Increases Quantum Dot Solar Cell Performance. *Adv. Mater.* **2016**, *28*, 299–304.

(9) Liu, M.; De Arquer, F. P. G.; Li, Y.; Lan, X.; Kim, G. H.; Voznyy, O.; Jagadamma, L. K.; Abbas, A. S.; Hoogland, S.; Lu, Z.; Kim, J. Y.; Amassian, A.; Sargent, E. H. Double-Sided Junctions Enable High-Performance Colloidal-Quantum-Dot Photovoltaics. *Adv. Mater.* **2016**, *28*, 4142–4148.

(10) Luo, J.; Dai, X.; Bai, S.; Jin, Y.; Ye, Z.; Guo, X. Ligand Exchange of Colloidal ZnO Nanocrystals from the High Temperature and Nonaqueous Approach. *Nano-Micro Lett.* **2013**, *5*, 274–280.

(11) Janotti, A.; Van De Walle, C. G. Fundamentals of Zinc Oxide as a Semiconductor. *Reports Prog. Phys.* **2009**, *72*, 126501.

(12) Singh, K. J.; Singh, C. A.; Singh, T. J.; Chettri, D.; Sarkar, S. K. ZnO Based Homojunction P-i-n Solar Cell to Self-Power UV Detector. *Proc. Int. Conf. Inven. Commun. Comput. Technol.* **2017**, No. Icicct, 304–307.

(13) Kim, G. H.; García De Arquer, F. P.; Yoon, Y. J.; Lan, X.; Liu, M.; Voznyy, O.; Yang, Z.; Fan, F.; Ip, A. H.; Kanjanaboos, P.; Hoogland, S.; Kim, J. Y.; Sargent, E. H. High-Efficiency Colloidal Quantum Dot Photovoltaics via Robust Self-Assembled Monolayers. *Nano Lett.* **2015**, *15*, 7691–7696.

(14) Yang, Z.; Janmohamed, A.; Lan, X.; García De Arquer, F. P.; Voznyy, O.; Yassitepe, E.; Kim, G. H.; Ning, Z.; Gong, X.; Comin, R.; Sargent, E. H. Colloidal Quantum Dot Photovoltaics Enhanced by Perovskite Shelling. *Nano Lett.* **2015**, *15*, 7539–7543.

(15) Yang, X.; Hu, L.; Deng, H.; Qiao, K.; Hu, C.; Liu, Z.; Yuan, S.; Khan, J.; Li, D.; Tang, J.; Song. H.; Cheng, C. Improving the Performance of PbS Quantum Dot Solar Cells by Optimizing ZnO Window Layer. *Nano-Micro Lett.* **2017**, *9*, 1–10.

(16) Rekemeyer, P. H.; Chang, S.; Chuang, C. H. M.; Hwang, G. W.; Bawendi, M. G.; Gradečak, S. Enhanced Photocurrent in PbS Quantum Dot Photovoltaics via ZnO Nanowires and Band Alignment Engineering. *Adv. Energy Mater.* **2016**, *6*, 1600848 .

(17) Jean, J.; Chang, S.; Brown, P. R.; Cheng, J. J.; Rekemeyer, P. H.; Bawendi, M. G.; Gradečak, S.; Bulović, V. ZnO Nanowire Arrays for Enhanced Photocurrent in PbS Quantum Dot Solar Cells. *Adv. Mater.* **2013**, *25*, 2790–2796.

(18) Bai, S.; Wu, Z.; Xu, X.; Jin, Y.; Sun, B.; Guo, X.; He, S.; Wang, X.; Ye, Z.; Wei, H.; Han, X.; Ma, W. Inverted Organic Solar Cells Based on Aqueous Processed ZnO Interlayers at Low Temperature. *Appl. Phys. Lett.* **2012**, *100*, 203906.

(19) Jagadamma, L. K.; Abdelsamie, M.; El Labban, A.; Aresu, E.; Ngongang Ndjawa, G. O.; Anjum, D. H.; Cha, D.; Beaujuge, P. M.; Amassian, A. Efficient Inverted Bulk-Heterojunction Solar Cells from Low-Temperature Processing of Amorphous ZnO Buffer Layers. *J. Mater. Chem. A* **2014**, *2*, 13321–13331.

(20) You, J.; Chen, C. C.; Dou, L.; Murase, S.; Duan, H. S.; Hawks, S. A.; Xu, T.; Son, H. J.; Yu, L.; Li, G.; Yang, Y. Metal Oxide Nanoparticles as an Electron-Transport Layer in High-Performance and Stable Inverted Polymer Solar Cells. *Adv. Mater.* **2012**, *24*, 5267–5272.

(21) S. Choopun, R. D. Vispute, W. Noch, A. Balsamo, R. P. Sharma, T. Venkatesan, A. Iliadis and D. C. Look, *Appl. Phys. Lett.*, **1999**, *75*, 3947–3949.

(22) Christoulakis, S.; Suchea, M.; Koudoumas, E.; Katharakis, M.; Katsarakis, N.; Kiriakidis, G. Thickness Influence on Surface Morphology and Ozone Sensing Properties of Nanostructured ZnO Transparent Thin Films Grown by PLD. *Appl. Surf. Sci.* **2006**, *252*, 5351–5354.

(23) Garvey, T. R.; Farnum, B. H.; Lopez, R. Pulsed Laser Deposited Porous Nano-Carpets of Indium Tin Oxide and Their Use as Charge Collectors in Core-Shell Structures for Dye Sensitized Solar Cells. *Nanoscale* **2015**, *7*, 2400–2408.

(24) Cullity, B. D. *Elements of DIFFRACTION*, 2nd ed, **1978**; Chapter 3, pp 101-103.

(25) Yang, D.; Li, B.; Hu, C.; Deng, H.; Dong, D.; Yang, X.; Qiao, K.; Yuan, S.; Song, H. Controllable Growth Orientation of SnS_2 Flakes for Low-Noise, High-Photoswitching Ratio, and Ultrafast Phototransistors. *Adv. Opt. Mater.* **2016**, *4*, 419–426.

(26) Cowan, S. R.; Roy, A.; Heeger, A. J. Recombination in Polymer-Fullerene Bulk Heterojunction Solar Cells. *Phys. Rev. B* **2010**, *82*, 245207.

(27) Gadisa, A.; Hara, Y.; Fu, Y.; Vrouwenvelder, K. T.; Dempsey, J. L.; Samulski, E. T.; Lopez, R. Disparity in Optical Charge Generation and Recombination Processes in Upright and Inverted PbS Quantum-Dot Solar Cells. *J. Phys. Chem. C.* **2015**, *119*, 4606–4611.

(28) Hara, Y.; Gadisa, A.; Fu, Y.; Garvey, T.; Vrouwenvelder, K. T.; Miller, C. W.; Dempsey, J. L.; Lopez, R. Gains and Losses in PbS Quantum Dot Solar Cells with Submicron Periodic Grating Structures. *J. Phys. Chem. C.* **2016**, *120*, 8005–8013.

(29) Mallajosyula, A. T.; Iyer, S. S. K.; Mazhari, B. Charge Transport in Polythiophene:Fullerene:Nanotube Bulk Heterojunction Photovoltaic Devices Investigated by Impedance Spectroscopy. *Curr. Appl. Phys.* **2013**, *13*, 677–683.

(30) Wang, H.; Wang, Y.; He, B.; Li, W.; Sulaman, M.; Xu, J.; Yang, S.; Tang, Y.; Zou, B. Charge Carrier Conduction Mechanism in PbS Quantum Dot Solar Cells: Electrochemical Impedance Spectroscopy Study. *ACS Appl. Mater. Interfaces* **2016**, *8*, 18526–18533.

(31) Bisquert, J. Theory of the Impedance of Electron Diffusion and Recombination in a Thin Layer. *J. Phys. Chem. B* **2002**, *106*, 325–333.

(32) Mora-Seró, I.; Garcia-Belmonte, G.; Boix, P. P.; Vázquez, M. A.; Bisquert, J. Impedance Spectroscopy Characterisation of Highly Efficient Silicon Solar Cells under Different Light Illumination Intensities. *Energy Environ. Sci.* **2009**, *2*, 678-686.

(33) Moehl, T.; Kytin, V. G.; Bisquert, J.; Kunst, M.; Bolink, H. J.; Garcia-Belmonte, G. Relaxation of Photogenerated Carriers in P3HT:PCBM Organic Blends. *ChemSusChem* **2009**, *2*, 314–320.

(34) Mora-Seró, I.; Luo, Y.; Garcia-Belmonte, G.; Bisquert, J.; Muñoz, D.; Voz, C.; Puigdollers, J.; Alcubilla, R. Recombination Rates in Heterojunction Silicon Solar Cells Analyzed by Impedance Spectroscopy at Forward Bias and under Illumination. *Sol. Energy Mater. Sol. Cells* **2008**, *92*, 505–509.

(35) Shuttle, C. G.; O'Regan, B.; Ballantyne, A. M.; Nelson, J.; Bradley, D. D. C.; De Mello, J.; Durrant, J. R. Experimental Determination of the Rate Law for Charge Carrier Decay in a Polythiophene: Fullerene Solar Cell. *Appl. Phys. Lett.* **2008**, *92*, 2006–2009.

(36) O'Regan, B. C.; Scully, S.; Mayer, A. C.; Palomares, E.; Durrant, J. The Effect of Al_2O_3 Barrier Layers in TiO_2/Dye/CuSCN Photovoltage Cells Explored by Recombination and DOS Characterization Using Transient Photovoltage Measurements. *J. Phys. Chem. B* **2005**, *109*, 4616–4623.

(37) Ip, A. H.; Thon, S. M.; Hoogland, S.; Voznyy, O.; Zhitomirsky, D.; Debnath, R.; Levina, L.; Rollny, L. R.; Carey, G. H.; Fischer, A.; Kemp, K. W.; Kramer, I. J.; Ning, Z. J.;Labelle, A. J.; Chou, K. W.; Amassian, A.; Sargent, E. H. Hybrid Passivated Colloidal Quantum Dot Solids. *Nat. Nanotechnol.* **2012**, *7* , 577–582.

(38) Prasada Rao, T.; Goswami, G. K.; Nanda, K. K. Detailed Understanding of the Excitation-Intensity Dependent Photoluminescence of ZnO Materials: Role of Defects. *J. Appl. Phys.* **2014**, *115*, 1–8.

(39) Chen, S.; Small, C. E.; Amb, C. M.; Subbiah, J.; Lai, T. H.; Tsang, S. W.; Manders, J. R.; Reynolds, J. R.; So, F. Inverted Polymer Solar Cells with Reduced Interface Recombination. *Adv. Energy Mater.* **2012**, *2*, 1333–1337.

(40) Zeng, H.; Duan, G.; Li, Y.; Yang, S.; Xu, X.; Cai, W. Blue Luminescence of ZnO Nanoparticles Based on Non-Equilibrium Processes: Defect Origins and Emission Controls. *Adv. Funct. Mater.* **2010**, *20*, 561–572.

(41) Sun, Y.; Seo, J. H.; Takacs, C. J.; Seifter, J.; Heeger, A. J. Inverted Polymer Solar Cells Integrated with a Low-Temperature-Annealed Sol-Gel-Derived ZnO Film as an Electron Transport Layer. *Adv. Mater.* **2011**, *23*, 1679–1683.

Chapter 5：The Effect of Light Intensity, Temperature, and Oxygen Pressure on the Photo-oxidation Rate of Bare PbS Quantum Dots[1]

5.1 Introduction

Owing to its unique optical property coupled with its charge transport characteristics, PbS QDs have already been advantageously exploited in PbS QDs-based solar cell application. To achieve better performance of PbS QDs-based solar cells, people has been made great efforts through different aspects. In chapter 2 and 4, through device architecture engineering approach, we have already elaborated that the device performance enhancement could be achieved by introducing grating pattern and optimizing the morphology of the ZnO window layer. In this chapter, we'll return to the nature of PbS QDs itself and discuss another way to passivate its surface states.

Since QDs often present unsatisfied dangling bonds at the surface, it gives rise to surface defect states in the bandgap. Despite the progress achieved by colloidal synthesis and the molecular surface passivation of those defects, one of the major obstacles that limits the scope of QD applications is the nature and kinetics of environmentally induced QDs chemical instabilities, because these usually lead to deleterious QD compositional changes and degradation of the material's performance.[1] Several researchers have previously investigated the stability of PbS QDs. [2,3] Most of these inquiries have noted the existence of thermal [4,5] and photo-induced paths for oxidation and degradation. [1] However, in the vast majority of these studies, the physical and chemical changes to the chalcogenide surface are convoluted with the degradation or alterations in the capping or linking ligands, which mask the evolution of the PbS itself under the environmental variables of interest (light, gas and temperature). This is fair in some instances, as for many

[1]This chapter previously appeared as an article in the Journal of ACS Applied Nanomaterials. The original citation is as follows: Liu, H., Dong, Q., Lopez, R. *Nanomaterials*, **2018**, *8*(5), 341

applications, those molecules are an integral part of the device operation. However, in no few cases, the environmental evolution of the QDs becomes intricately more complex, making it extremely hard to arrive at precise descriptions of the physical-chemical processes. For instance, Peterson et al. [6] found that the photo-oxidation rate of PbS quantum dots was size dependent; this is a very interesting result, but the QDs studied were oleic acid coated and embedded within a polymer, which made the gas-QD surface interaction hard to describe in a quantitative way. When Zhang et al. [7] observed photo-induced luminescence (PL) enhancement in similarly-prepared oleic acid coated PbS QDs in solution, they determined that the light activation was dependent on the solution concentration. However, the QD's surface change or its kinetics induced by the light could not be precisely quantified since the light intensity on the QDs varied with penetration depth and the solution was bound to present convection. Beyond lacking quantitative assessment, Turyanska et al. [8] studied the temperature dependence of the near-infrared PL emission from thiol-capped PbS QDs; finding that such PbS QDs showed no time-dependent change. In contrast, Ihly et al. [4] showed that ethanedithiol-treated PbS QDs in films will oxidize, ripen, and even sinter. Because most of these discrepancies could be traced to non-trivial differences in testing conditions and QDs cappings, to have a clear relationship between light, gas pressure, temperature, and the rate of change at the surface of PbS quantum dots, we propose it is necessary to test the evolution under those environmental variables in non-aggregated ligand-free PbS QDs, with the goal of arriving to precise quantitative reaction rates. The quantitative knowledge from this condition will help to establish a reliable basis upon which to compare all other modified QDs.

In the previous work conducted by our colleagues, we found that although the solar cells based on the PbS QDs synthesized via PLD technique produced a very low J_{SC} as well as the efficiency, the V_{OC} of the devices was improved significantly, approaching approximately 0.725V. This was much higher than the record has been report and thus may provide more possibilities for the performance improvement of the PbS QD based solar cells. In this chapter, we report on the quantitative relationship between the above-mentioned variables and the oxidation of bare PbS QDs directly fabricated by PLD. We found that under

relatively intense illumination with photon energy larger than the bandgap, the kinetics of the oxidation process can be fitted to a minimal physical kinetic model to obtain a precise relationship between the environmental conditions and the oxidation rate constant of the process. In particular, we note that when subjected to illumination, the rate of the oxidation was boosted to a linear relationship with light intensity and O_2 pressure. Furthermore, under illumination, the temperature of the environment was also played a significant role, with an apparent activation energy barrier of only 0.19 eV. These findings, obtained from easy-to-follow changes in the PL emission under controlled conditions, are significant because they highlight the key role that photo-excitation performs in the material transformation process and the substitutive roles that O_2, light intensity, and temperature can play in the oxidation of PbS QDs.

5.2 Experiments

Ligand-free PbS QDs were fabricated using pulsed laser deposition (PLD) [9] by ablation of a pressed PbS powder target using a KrF excimer laser (λ = 248 nm; repetition rate = 10 Hz, fluence = 5 J/cm^2) under 500 mTorr of Helium (99.999% pure) background gas pressure that filled the chamber, which, prior to the experiment, was evacuated to 1 $\times 10^{-6}$ Torr. The PbS QDs growth was performed at room temperature onto fuse silica, SiO_2/Si substrates, and transmission electron microscopy (TEM) carbon grids simultaneously and placed on a rotating holder parallel to, and 10 cm away, from the target. Although the method allowed for simple QDs size, controlled via the number of laser shots (N_{LP}) (Figure 5.1a), we selected the samples made with N_{LP} = 500 shots to be the focus of this study to maintain a constant QD size. The QDs obtained under such conditions were ~2.5 nm in average diameter and ±1 nm enclosed the sample size dispersion. Figure 5.1b shows the X-ray diffraction pattern (XRD) obtained using a Bruker D8 Discover diffractometer (using Cu-Kα radiation) for samples deposited on the fuse silica substrates. With less than one monolayer of QDs, only one X-ray peak is easily distinguishable over the background. The position of this peak perfectly matched the (002) planes of cubic of PbS. [10] Figure 5.1c shows the TEM micrograph of these QDs, obtained using a JEOL 2100-plus microscope operated at 200 kV. The inset in Figure 5.1c displays the

electron diffraction pattern for this sample, highlighting the crystallinity and random orientation of the QDs. The first few diffraction rings that could be distinguished with clarity corresponded to the (200), (220), and (222) crystal planes of PbS. [11]

For this study, the primary tool used to track the evolution of the QDs was their PL. PL measurements were carried out by exciting the sample using 532 nm wavelength emissions from a continuous wave laser. Photoluminescence spectra were recorded by a thermoelectrically-cooled CCD camera. The system is integrated in a confocal microscope using a 50 × microscope objective. However, important for our study, the laser instead of having a diffraction limited size was defocused so that the beam spot was at the sample and reached approximately 1.75 μm in radius. Thus, the area from which PL was detected by the collection photonic fiber (3 micrometer cores) was only the ~5% central top of the Gaussian beam. This was done to secure a uniform intensity excitation over all the QDs under observation simultaneously. PL from QDs in the skirts of the Gaussian beam excitation were not able to enter the microscope collection fiber.

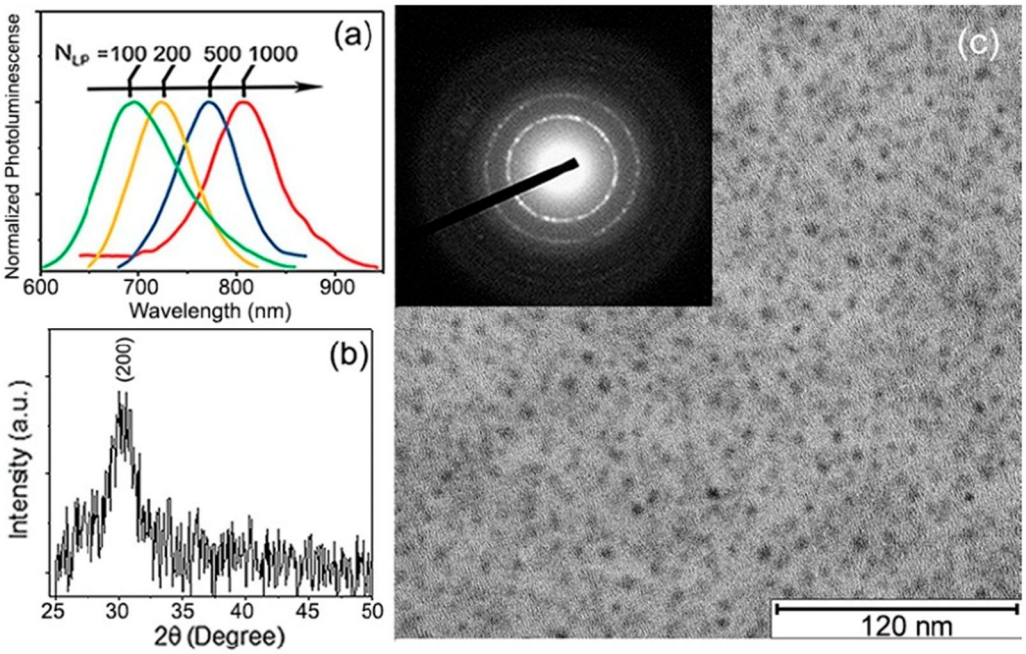

Figure 5.1 (a) Initial photoluminescence (PL) spectra of PLD-deposited PbS QDs with different number of laser shots (N_{LP}). PL of the PbS QDs shows clearly red shift from 680 to 820 nm. This obvious shift is a consequence of the quantum size effects of the PbS QDs; [9] (b) XRD pattern of PbS QDs deposited with N_{LP}

= 500; (c) TEM image of PbS QDs deposited directly onto carbon-filmed-grids; the inset in (c) is their TEM diffraction pattern.

5.3 Oxidation Kinetics Analysis for PbS QDs

Figure 5.2 shows the typical PL time evolution for all the experiments performed to analyze the oxidation kinetics of the QDs. The PL always started relatively weak with an emission peak centered at 765 nm wavelength. With time, the PL intensity increased progressively to eventually reach a maximum, for which the magnitude and time stability depended on the specific environmental variables and excitation intensity. Simultaneously, the PL peak could be observed shifting toward shorter wavelengths. After some additional time, lasting from a few seconds to several hours, still under continuous laser excitation, the intensity of the PL signal started to decrease toward low emission yields. Samples on SiO_2 and SiO_2 /Si substrates behaved identically, ruling out possible significant heating effects from laser during this evolution. This process closely resembles the phenomenon of photoactivation extensively documented in CdSe nanocrystals. [12-14] Assuming our observations are fully analogous, the oxidation thus should follow a progressive reaction from the surface to the core, giving an initial PL enhancement through early surface oxide passivation, which continues deepening until the core of the QD is transformed. The chemical products of prolonged atmospheric oxidation of PbS QDs, albeit coated with molecular linkers, have been examined by several researchers.[3,15,16] Examination of the laser-irradiated spots (from beginning to end of their PL evolution) by fitting of the Pb $4f_{7/2}$ level obtained from X-ray photoelectron spectroscopy (XPS) shows that the chemical state of the Pb atoms can be deconvoluted into three major contributions (Figure 5.2 b–d) of which relative weights vary with time. For the QDs freshly deposited and exposed to air but without any laser-irradiation, the XPS spectrum showed that, besides the 137 eV feature due to PbS, there was already a small but not negligible signal at 138.3 eV due to the initial formation of possible intermediate oxidation products, [15-17] $Pb(OH)_2$, PbO, and/or $PbSO_3$. These products cannot be independently quantified here, although other researchers advocate that $PbSO_3$ makes up the majority of the intermediates.[3] Inspection of areas where the experiment was stopped at the time of maximum PL intensity showed that the transformation of the PbS

into the intermediate oxidation products had taken a significant fraction of the QDs' mass (~60%), presumably just the most external atoms, reducing the QDs effective size to ~1.8 nm. Albeit a small fraction, this stage also seemed to correspond with the appearance of $PbSO_4$, which marks the beginning of the PL decline. After a longer period under light exposure, when the PL decreased to a small fraction from its peak value, the Pb $4f_{7/2}$ peak shifted almost completely to 140.0 eV, indicating the bulk of each nanocrystal had been transformed into $PbSO_4$. [17]

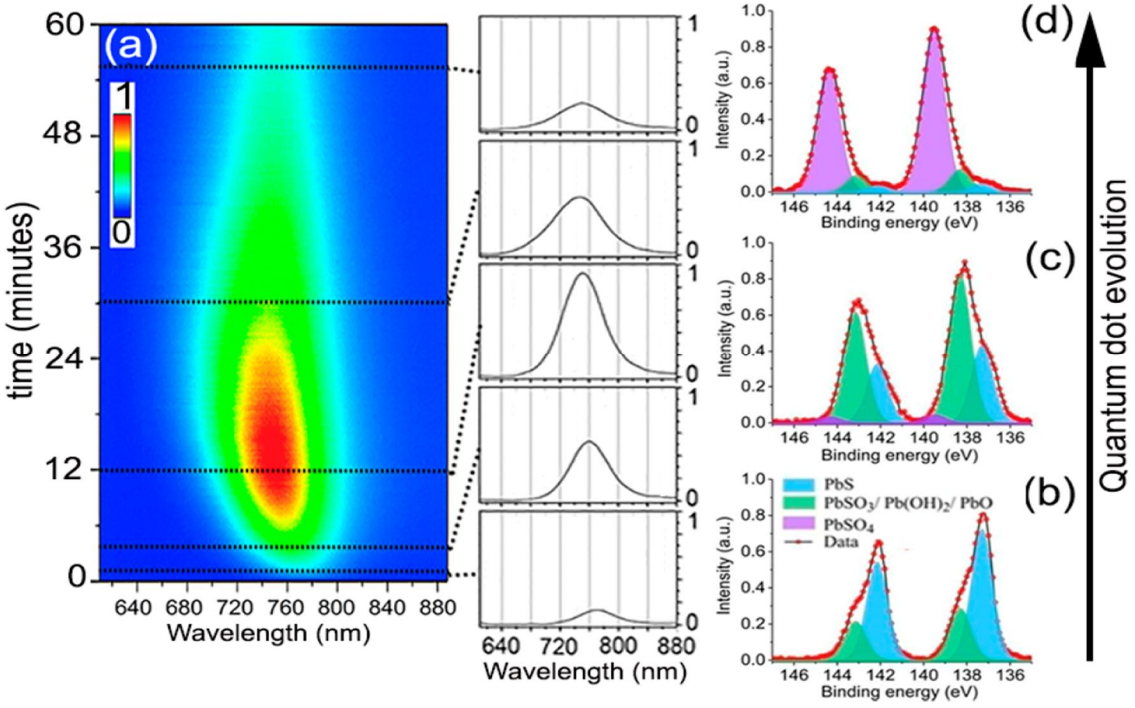

Figure 5.2 (a) Typical of the photoluminescence spectrum for the PbS QDs, all the experiments presented similar behavior but with marked time differences depending on the exact environmental conditions. (b) – (d) XPS Pb $4f_{7/2}$ spectrum of the freshly deposited, after laser-irradiation until reached maximum PL intensity, and after PL intensity decayed, respectively. The XPS measurement was conducted using a Thermo Fisher ESCALAB 250XI Analyzer with base pressure below 10^{-10} mbar. Al Kα (1486.6 eV) radiation was used as an X-ray source (15 kV, 159.3 W)

5.4 Impacts of the Light Intensity, O_2 Pressure and Temperature on the Oxidation Kinetics of PbS QDs

Figure 5.3 shows the all-wavelength-integrated PL as a function of time under the influence of the three environmental variables under consideration: Light intensity, O_2 pressure, and temperature. As observed, the three variables had a direct effect on the rise and subsequent decrease of the total integrated PL counts,

but its characteristic times and maxima require a detailed analysis to quantitatively obtain the overall kinetic properties of the oxidation process. To determine the specific mathematical form of the oxidation rate, we employ a simple phenomenological model of the PL under the oxidation process. [18] Here we suppose that in each QD and at all times, there exist N_T constant pairs of PbS atoms that, under the oxidation process and illumination, can be found oxidized to some extent (N_C), prepared to absorb a photon (N_A), or already responsible for one exciton (N_{A^*}), such that $N_T = N_A + N_{A^*} + N_C$. We do not specify each PbS pair location inside of the QD as it is assumed that the oxidation proceeds from the outside toward the center, that is, the N_C pairs make a growing outer shell at the expense of the decreasing $N_A + N_{A^*}$. Over time, the rate of change of each quantity should follow the following rate equations:

$$\frac{dN_{A^*}}{dt} = \alpha(N_A - N_{A^*}) - \frac{N_{A^*}}{\tau} - k^* N_{A^*} \tag{5.1}$$

$$\frac{dN_A}{dt} = \alpha(N_{A^*} - N_A) + \frac{N_{A^*}}{\tau} - kN_A \tag{5.2}$$

$$\frac{dN_C}{dt} = k^* N_{A^*} + kN_A \tag{5.3}$$

where in $\alpha = \sigma I/h\upsilon$, σ represents the light absorption cross-sectional area per PbS pair, I is the intensity of the incident light, and $h\upsilon$ is the photon energy. k and k^* are the rate constants for the reaction under dark and light, respectively; and $\tau = (\tau_R^{-1} + \tau_{NR}^{-1})^{-1}$ is the lifetime of the exciton allowing for non-radiative (NR) and radiative (R) paths to ground state decay. The first term in Equations (5.1) and (5.2) represents the absorption and stimulated emission, and the second term corresponds to the spontaneous emission. The third term in both Equations (5.1) and (5.2) represents the oxidation processes that result in an increase of the number of the oxidized pairs (N_C), as is correspondingly shown in Equation (5.3).

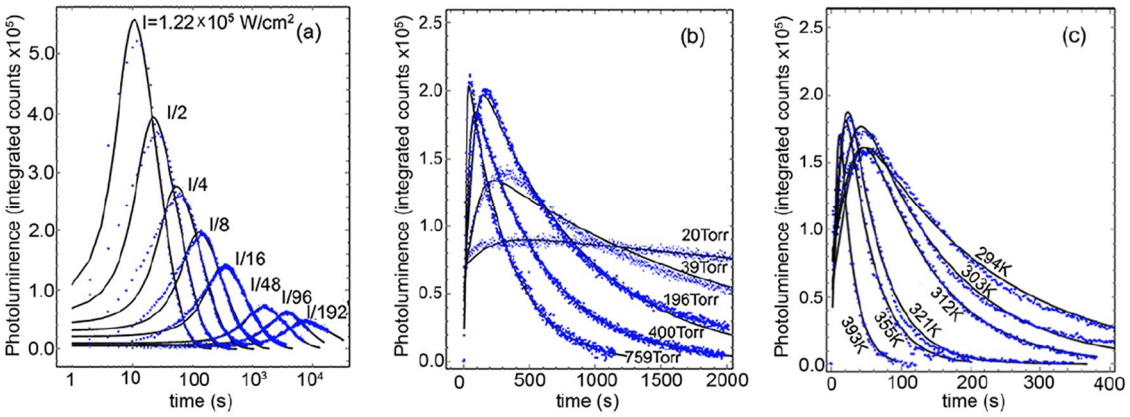

Figure 5.3 Time evolution of the photoluminescence integrated intensity for the PbS QDs, under three distinct experimental conditions: (a) Variation over laser power with 1 atmosphere of oxygen pressure and constant temperature (294 K), (b) variation under different oxygen pressures at room temperature and 1.54 $\times 10^4$ W/cm^2 light intensity, and (c) temperature effect at constant pressure (1 atmosphere) and same constant laser power. Solid lines are fit to the physical model described in the text.

As the early oxidation of the surface has a PL-enhancing effect, we can expect that the initial oxidation lengthens the τ_{NR} to favor the radiative path of decay. Phenomenologically, we propose the non-radiative life time be inversely related to the number of non-oxidized PbS pairs as $\tau_{NR} \sim \frac{1}{(N_{A^*}+N_A)^{\gamma}}$, where γ is an exponent to be determined from the experiment. Because the radiative PL lifetime of PbS QDs has been measured by others and found to be ~1 μs, [19] the reaction under light we measured in our experiments happens over ~1–1000 s, and the reaction under dark requires > 1 month, [4] to explicitly solve the system of equations we adopted the following approximation $\tau^{-1} \gg k^* \gg k \sim 0$. In this regime, the photon-mediated process is the only path for oxidation and the huge difference between $\tau^{-1} \gg k^*$ permit us to solve Equations (5.1) and (5.2), simultaneously, in a closed form to obtain quasi-static values for N_A and N_{A^*}. The values of N_A and N_{A^*} will then slowly decrease under the rate defined in Equation (5.3). Since $\mathrm{PL} \sim \frac{N_{A^*}}{1+\tau_R/\tau_{NR}}$, this results in a rather simple explicit expression as the PL integrated counts as a function of time:

$$\mathrm{PL(t)} = \mathrm{A}\frac{\exp(-Bt)}{1+Cexp(-\gamma Bt)} \tag{5.4}$$

with $A = M\left(\frac{\alpha}{\tau^{-1}+2\alpha}\right)$, $C = \frac{\tau_R}{\tau_{NRt=0}}$ and the effective reaction rate $B = \frac{k^*\alpha}{\tau^{-1}+2\alpha}$. The model assumes all QDs are behaving similarly and does not include explicitly diffusion or any atomic-detail steps that must occur during the oxidation. As detailed work on metal nanoparticle oxidation has demonstrated, [20] the complexity of a more detailed theory involves so large a number of parameters, such as a variety of activation energies, pre-exponential factors of individual oxidation stages, ion and electron diffusion coefficients, that from the standpoint of the experimental observation, only their collective behavior could be probed. The simple model we employ (Equation (5.4)) contains just five parameters for determination, namely M, γ, C, τ, and k^*, with the rest derived from their relationships or fixed from the materials properties or experimental conditions. Of those five parameters, M is practically arbitrary and has no real importance, as it stands for the number of QDs in the examined area and the efficiency of the whole microscope optical train and detector setup. The remaining four are all physically meaningful, and although they all could in principle depend on the environmental variables, we can expect their sensitivity to them be quite low.τ, strictly speaking, should be a function of the oxidation, varying as the non-radiative recombination path is changing relevance. By this physical connection, all the environmental variables could affect τ, but in the approximation taken to solve for the quasi-static value of N_{A^*}, it is left to be a constant value, thus it represents an effective exciton lifetime, moving from non-radiative to radiative, over the whole QD oxidation process. The solid line in Figure 5.4a shows the fit of the A parameter from Equation (5.4), the amplitude coefficient of the PL counts. Following its functional form $A = M\left(\frac{\alpha}{\tau^{-1}+2\alpha}\right)$, we expect it to be strongly dependent on the light intensity alone. This allows the simultaneous determination of M = 2.08 $\times 10^6$ counts, and τ = 6.11 $\times 10^{-8}$ s. Although the model is fairly simple, τ results in the expected range between the best radiative life times reported and non-radiative values that would prevent PL emission.

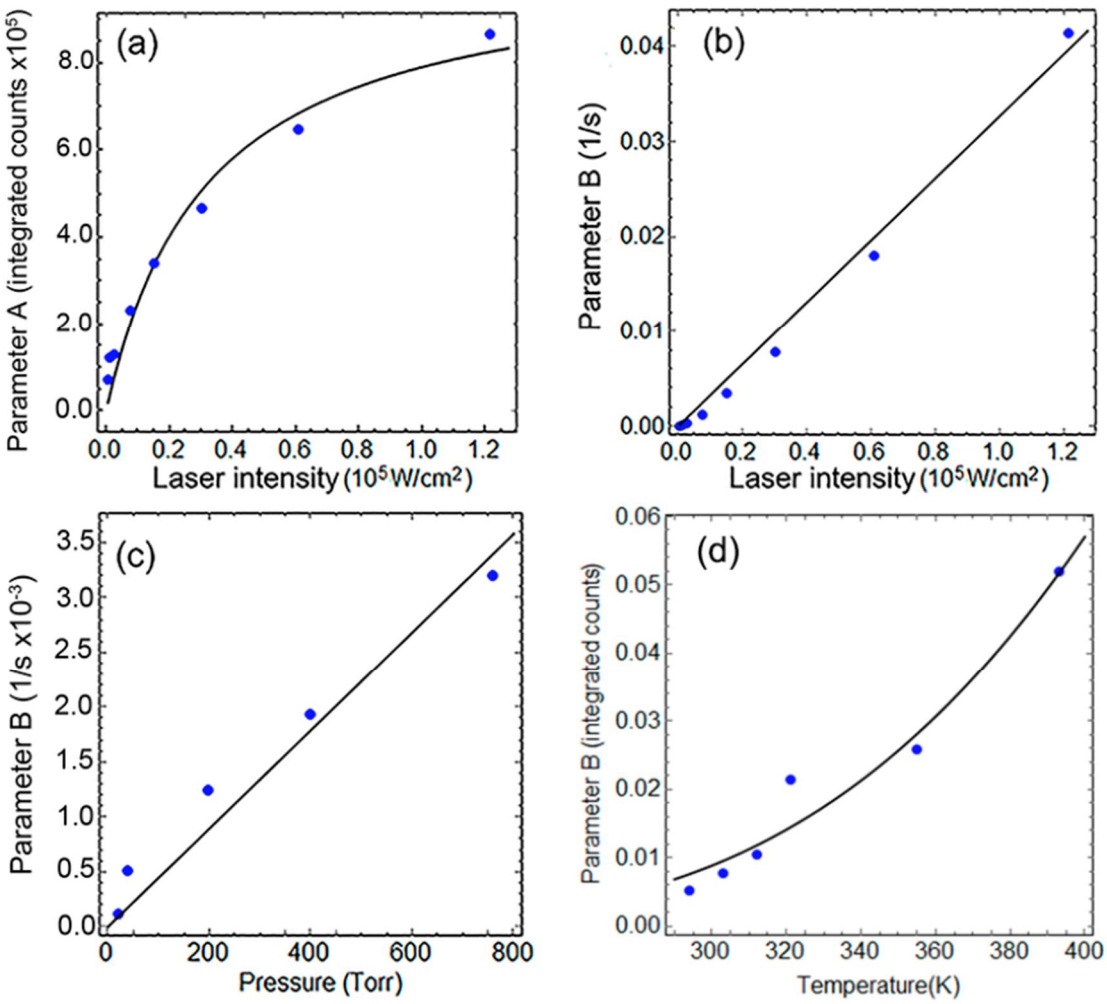

Figure 5.4 (a, b) parameters A and B under different light intensities at 294 K and 1 atmosphere of oxygen, respectively; (c) Parameter B as function of pressure at 294 K and 1.54 $\times 10^4$ W/cm^2 light intensity; (d) Parameter B as function of temperature at 1 atmosphere and same light intensity. Dots are the specific parameters that produce the fitted curves in Figure 5.3. Solid lines are best fits to functional forms of those parameters vs. The controlled environmental variables as explained in detail in the following.

Parameters γ and C work together to determine the onset behavior of the PL intensity increase. For all the samples and conditions explored, their fitting showed weak dependencies on the environmental variables. This perhaps means that all initial surface atom changes are all similarly fast, leaving the effective rate constant B to carry the weight of the environmental variables' functionality. Figure 5.4c, d presents the functional fits of parameter B against laser power, O_2 pressure, and temperature. Their functional form was not assumed before the fitting procedure, but as it can be seen, B presents a good simple linear dependence with the light intensity and the oxygen pressure, and an expected Arrhenius behavior with the absolute

temperature. The collective information from those fits can be summarized in the following succinct expression, $B = B_0 I P_{O^2} \exp(\frac{-\Delta E}{k_B T})$, where I is the laser intensity in W/cm^2, P_{O^2} is the oxygen pressure in atmospheres (during the PL experiment, sample chamber was evacuated to 10^{-5} torr prior to filling with oxygen 99.999% pure), ΔE = 0.19 eV is the apparent energy barrier, k_B is the Boltzman constant, T is the temperature, and $B_0 = 5.0 \times 10^{-4} \frac{cm^2}{s \cdot W \cdot atm}$ is the proportionality constant. To put in context how much lower the oxidation barrier appears under illumination, the free energy of reaction for formation of $PbSO_4$ from PbS and O_2 is reported to be -718 kJ/mol (-7.45 eV/PbS pair). [3] Thus, illumination allows the oxidation to proceed at much higher rate.

The effect of the light intensity on B has an interesting consequence, under 1 sun intensity ~0.1 W/cm^2 for example, the process results in an effective rate of only $B = 3.5 \times 10^{-8}$ s^{-1}, a significantly low value that, after early surface passivation, might give the appearance of very constant PL. This is in line with our experience and that from other researchers [4] whose QDs perform well even months after fabrication when stored in the laboratory air and exposed to ambient light. However, note this does not translate directly into the same behavior for k^*, the actual rate constant, which the model requires to be $k^* = 2B_0 I P_{O^2} \exp(\frac{-\Delta E}{k_B T})(1 + h\upsilon/2\tau\sigma)$ (expression obtained from combining the above phenomenological expression for B and the model-required relationship with k^*). This expression approaches a non-zero constant at low light intensities, which at 1 atmosphere and room temperature would be $k^* = 2.07 \times 10^{-2}$ s^{-1}, a significantly faster rate than B. At low light intensities, the difference is the existence of an $\alpha\tau$ factor in $B \approx \alpha\tau k^*$, the number of absorbed photons during one relaxation time. The implication of this difference is that the effective rate decreases as light intensity goes down, mostly because the number of attempts made by photons to oxidize the QD is low, but the reaction rate of those few absorbed photons remains relatively high. If, at best, the radiative life time is ~1 μs, then the oxidation reaction probability of an absorbed photon will be $\frac{k^*}{k^* + \tau^{-1}} \sim 10^{-8}$. Therefore k^* coupled with a large photon flux can bring oxidation very rapidly.

It is also worth remarking that low oxygen content effectively arrests the oxidation without need to reach extremely low pressures. At 20 mTorr we noticed the PL was activated and remained close-to-stable for many hours without significant change. However, crucially, at higher vacuum levels <10 mTorr, the PL yield did not increase at all, marking the environment quality required for a maximum oxygen concentration to protect QDs from oxidation under light utilization. Regarding the influence of temperature on the oxidation process, we can see that moderate above-room-temperature conditions readily enhanced the oxidation process. Due to some limitations in our microscope setup, we did not test low temperature evolution; however, given the functional form that fits our temperature data in the near-above-room-temperature range, only very low temperatures are likely to significantly slow down the oxidation process. On the contrary, under no-illumination conditions and full 1atmosphere O_2 pressure, the same temperature range probed in our experiment had not affected the QDs in any observable way, because after cooling the samples that experienced the thermal treatment under dark, showed PL behavior identical to samples that did not experience this treatment. Another observation we wish to mention is that performing the oxygen concentration experiments with "wet" oxygen (passing the gas through water before filling the chamber) did not change the kinetics at all, which does not support the conjecture that the presence of some water might aid the oxidation process significantly, in contrast to literature examples of QDs in solution where water is attributed an important role in the photo-oxidation.[21]

5.5 Conclusion

In this chapter, the true rate constant for the oxidation of bare PbS QDs was determined through the fit of the PL integrated counts as function of temperature, oxygen pressure, and laser intensity, which highlighted their combined effect on the number photo-excited excitons and their reduced barrier to allow for the oxidation process. Although the oxidation steps and intermediate compounds are complicated, our experiment and model results seem to indicate that the overall oxidation reaction is first order with the oxygen pressure and the light intensity. Thus, even though the $k^*$is very large, the effective oxidation rate is dominated by the oxygen and photon availability. This work may help in setting a quantitative reference

upon which characterize the stability of QDs in general, and specifically to encourage the study of the stability of those coated with ligands/linkers in a quantitatively precise and thus comparatively fair way. Identifying whether the source of protection against oxidation might come from blocking the photo-oxidation path, or by simply limiting the oxygen availability, might be important distinction in the design of increasingly more robust PbS QDs stabilization layers. With this distinction in mind, the precise effect of the relevant environmental variables on the changes of more complex QDs systems coated with other participating molecules could be assessed.

REFERENCES

(1) Carrillo-Carrión, C.; Cárdenas, S.; Simonet, B. M.; Valcárcel, M. Quantum Dots Luminescence Enhancement due to Illumination with UV/Vis Light. *Chem. Commun.* **2009**, No. 35, 5214–5226.

(2) Chuang, C. M.; Brown, P. R.; Bulović, V.; Bawendi, M. G. Improved performance and stability in quantum dot solar cells through band alignment engineering, *Nature Materials*, **2014**, *13* (8), 796–801.

(3) Clark, P. C. J.; Radtke, H.; Pengpad, A.; Williamson, A. I.; Spencer, B. F.; Hardman, S. J. O.; Leontiadou, M. A.; Neo, D. C. J.; Fairclough, S. M.; Watt, A. A. R.; et al. The Passivating Effect of Cadmium in PbS/CdS Colloidal Quantum Dots Probed by nm-Scale Depth Profiling. *Nanoscale* **2017**, *9* (18), 6056–6067.

(4) Ihly, R.; Tolentino, J.; Liu, Y.; Gibbs, M.; Law, M. The Photothermal Stability of PbS Quantum Dot Solids. *ACS Nano* **2011**, *5* (10), 8175–8186.

(5) Ullrich, B.; Xiao, X. Y.; Brown, G. J. Photoluminescence of PbS Quantum Dots on Semi-Insulating GaAs. *J. Appl. Phys.* **2010**, *108* (1), 13525-1-013525-5.

(6) Peterson, J. J.; Krauss, T. D. Photobrightening and Photodarkening in PbS Quantum Dots. *Phys. Chem. Chem. Phys.* **2006**, *8* (33), 3851–3856.

(7) Zhang, T.; Zhao, H.; Riabinina, D.; Chaker, M.; Ma, D. Concentration-Dependent Photoinduced Photoluminescence Enhancement in Colloidal PbS Quantum Dot Solution. *J. Phys. Chem. C* **2010**, *114* (22), 10153–10159.

(8) Turyanska, L.; Patanè, A.; Henini, M.; Hennequin, B.; Thomas, N. R. Temperature Dependence of the Photoluminescence Emission from Thiol-Capped PbS Quantum Dots. *Appl. Phys. Lett.* **2007**, *90* (10), 1–4.

(9) Ka, I.; Ma, D.; El Khakani, M. A. Tailoring the Photoluminescence of PbS-Nanoparticles Layers Deposited by Means of the Pulsed Laser Ablation Technique. *J. Nanoparticle Res.* **2011**, *13* (6), 2269–2274.

(10) Wang, Y.; Suna, A.; Mahler, W.; Kasowski, R. PbS in Polymer. From Moleculs to Bulk Solids. *J. Phys. Chem. C* **1987**, *87* (12), 7315–7321.

(11) Liu, C.; Heo, J.; Zhang, X.; Adam, J. Photoluminescence of PbS Quantum Dots Embedded in Glasses. **2008**, *354*, 618–623.

(12) Nazzal, A. Y.; Wang, X.; Qu, L.; Yu, W.; Wang, Y.; Peng, X.; Xiao, M. Environmental Effects on Photoluminescence of Highly Luminescent CdSe and CdSe/ZnS Core/Shell Nanocrystals in Polymer Thin Films. *J. Phys. Chem. B* **2004**, *108* (18), 5507–5515.

(13) Nazzal, A. Y.; Qu, L.; Peng, X.; Xiao, M. Photoactivated CdSe Nanocrystals as Nanosensors for Gases. *Nano Lett.* **2003**, *3* (6), 819–822.

(14) Efros, A. L.; Nesbitt, D. J. Origin and Control of Blinking in Quantum Dots. *Nat. Nanotechnol.* **2016**, *11* (8), 661–671.

(15) Malgras, V.; Nattestad, A.; Yamauchi, Y.; Dou, S. X.; Kim, J. H. The Effect of Surface Passivation on the Structure of Sulphur-Rich PbS Colloidal Quantum Dots for Photovoltaic Application. *Nanoscale* **2015**, *7* (13), 5706–5711.

(16) Cant, D. J. H.; Syres, K. L.; Lunt, P. J. B.; Radtke, H.; Treacy, J.; Thomas, P. J.; Lewis, E. A.; Haigh, S. J.; Obrien, P.; Schulte, K.; et al. Surface Properties of Nanocrystalline PbS Films Deposited at the Water-Oil Interface: A Study of Atmospheric Aging. *Langmuir* **2015**, *31* (4), 1445–1453.

(17) Moulder, J. F.; Stickle, W. F.; Sobol, P. E.; Bomben, K. D. *Handbook of X-Ray Photoelectron Spectroscopy*, 2nd ed.; J. Chastain, Ed.; Perkin-Elmer Corp., Physical Electronics Division: Eden Prairie, Minnesota, USA, 1995.

(18) Bäuerle, D. *Laser Processing and Chemistry*, 4th ed.; Springer Berlin Heidelberg: Berlin, Heidelberg, 2011.

(19) Cheng, C.; Li, J.; Cheng, X. Photoluminescence Lifetime and Absorption Spectrum of PbS Nanocrystal Quantum Dots. *J. Lumin.* **2017**, *188*, 252–257.

(20) Chernavskii, P. A.; Peskov, N. V.; Mugtasimov, A. V.; Lunin, V. V. Oxidation of Metal Nanoparticles: Experiment and Model. *Russ. J. Phys. Chem. B* **2007**, *1* (4), 394–411.

(21) Hines, M. A.; Scholes, G. D. Colloidal PbS Nanocrystals with Size-Tunable Near-Infrared Emission: Observation of Post-Synthesis Self-Narrowing of the Particle Size Distribution. *Adv. Mater.* **2003**, *15* (21), 1844–1849.

Chapter 6 : Conclusion and Outlook

6.1 The Importance of Our Work

In this thesis, two device architecture engineering approaches were employed to investigate the impacts of device geometry and interfaces on the improvement of the device performance and the fundamental mechanism underneath for the PbS CQDs solar cells.

In the first approach, by employing a two-dimensional numerical model based on finite element method, the fully optoelectronic characteristics of both planar (1D) and submicron grating patterned TiO_2-PbS (2D) heterojunction CQD solar cell have been investigated. With optimized geometric parameters, the flat device could generate a maximum current density about 21 mA/cm^2. The further improvement is limited because of the existence of the mismatch between light absorption and charge carrier collection. However, the situation is changed when a grating patterned geometry is employed. The optimized pattered PbS CQD device showed a much higher J_{SC} of 35.2mA/cm^2, leading a 11.2% of PCE. This result confirms the assumption that by bring in a 2D grating pattern, more light absorption could be realized with packing more absorbing materials per unit of effective cross area within the transport length limit. This agrees well with the higher JSC was achieved as well as the PCE. Furthermore, in our case study, the performance enhancement arise from the patterned structure was experimentally confirmed.

Inspired by this spring-like grating structure, in the project of "making highly flexible and transparent ITO films and realizing its potential optoelectronic application" collaborated with Eastman Chemical Company, we developed a periodic submicron grating patterned ITO film on the Polyethylene terephthalate (PET) films. With the aid of fundamental studies on mechanics and optics for this feature, through optimizing the pattern pitch and height, this ITO pattern demonstrates superior performance both in

mechanical flexibility and optical transparency. Moreover, in the following investigation of its potential application for optoelectronic devices, worked as the transparent conductive electrode, the PbS CQDs solar cell that incorporated this patterned ITO/PET exhibited great flexibility and its optoelectrical performance was still roughly maintained.

Considering the inevitable defects arising from the nanofabrication of submicron grating pattern which is detrimental to the solar device performance, an alternative approach was investigated in the planar heterojunction PbS CQDs solar cells. The device performance could be significantly enhanced through optimizing the morphology of ZnO layer via adjusting the oxygen pressure during deposition. In the study, we found that changing the oxygen pressure would not only modify the atomic and micro- structure of the materials, resulting in drastic change of its optoelectrical properties, but also have an impact on the formation of different types of defects. Taking all these factors into account, the carrier conduction and transport mechanism underneath is deeply understood.

Finally, other than considering from the perspective of device architecture, we retrieved back to the bare PbS QDs itself. A quantitative study was conducted to explore the relationship between the photo-oxidation rate of PbS QDs prepared by pulsed laser deposition and other processing variables (including the temperature, light intensity and oxygen pressure), from which the stability of PbS QDs could be characterized. Moreover, this may provide us with a quantitative reference for the study of PbS QDs coated with linkers/ligands, shining light on the PbS QDs surface passivation strategy from a new perspective.

6.2 Outlook

6.2.1 Fabrication of Nanopattern with Better Quality

To improve the CQD solar cell performance, the approaches to enhance the light absorption that rely on nano- engineering need to be further developed. Given that an AM 1.5 solar flux would translate to 40 mA/cm^2 for a 100% efficient photon-to-electron conversion in PbS, the model discussed in chapter 2 predicts an overall 88% photo-to electron conversion efficiency at J_{SC} (35.2 mA/cm^2), which is comparable

to what is practical in more established materials with similar optical absorption range such as standard silicon or CZTSSe cells. However, as reviewed in our case study, the J_{SC} improvement is far below the expectation due to the defects introduced by nanofabrication. Moreover, in order for CQD solar cell to become a real player as an energy converter in the market, developing extremely simple methods to realize large-sale fabrication is mandatory. Therefore, to development more practical method for nanopatterning and seek superior nanostructures with ease of fabrication and more light absorption would still be the goal to keep pursing.

6.2.2 Device Interface Engineering

Recombination at the metal oxide−semiconductor interfaceis has always been an area of ongoing concern in heterojunction CQD solar cells. Considering the significant mismatch between fully light absorption and charge collection and the much lower performance compared to the prediction of shockley-queisser limit, to better control the recombination at the interface is of paramount importance. Several strategies have been used to overcome this performance-limiting process Engineering of both electron-collecting and hole-collecting as discussed early. With the development of more new materials as well as deeper understanding of the device's physics, more researches on exploring efficient buffer layer and engineering the band alignment continue to be necessary.